RELATIVE SIGNIFICANCE OF SHEAR STRESS AND HORIZONTAL PRESSURE GRADIENTS ON SEDIMENT MOBILITY IN THE INNER SURF AND SWASH ZONE

by

Michael J. Larner

A thesis submitted to the Faculty of the University of Delaware in partial fulfillment of the requirements for the degree of Master of Civil Engineering

Summer 2021

© 2021 Michael J. Larner
All Rights Reserved

RELATIVE SIGNIFICANCE OF

SHEAR STRESS AND HORIZONTAL PRESSURE GRADIENTS

ON SEDIMENT MOBILITY

IN THE INNER SURF AND SWASH ZONE

by

Michael J. Larner

Approved: _____

Jack A. Puleo, Ph.D.
Professor in charge of thesis on behalf of the Advisory Committee

Approved: _____

Jack A. Puleo, Ph.D.
Chair of the Department of Civil and Environmental Engineering

Approved: _____

Levi Thompson, Ph.D.
Dean of the College of Engineering

Approved: _____

Louis F. Rossi, Ph.D.
Vice Provost for Graduate and Professional Education and
Dean of the Graduate College

ACKNOWLEDGMENTS

I must begin by thanking my advisor, Dr. Jack A Puleo, for taking a chance and trusting me to represent both the University and your research team. Your enthusiasm and inquisitiveness for all things coastal has provoked, within me, a greater curiosity of coastal engineering than I could have ever imagined (to the point where I have even questioned “what is a beach?”). I am particularly thankful for your patience in allowing me to take the reins on my own research while also providing guidance and knowing when to steer me back on track.

I am incredibly grateful for Sara Dionísio António, the University of Twente, and everyone at UPC for making this research possible and providing me with the opportunity to travel across the pond and meet some amazing people in the coastal engineering community. Sara, thank you for all the ridiculous pictures you made with your remarkable editing skills and for introducing me to all the musical talent that Portugal has to offer. To Iván and José, I am incredibly thankful for welcoming me to Spain, showing me your beautiful country, offering me an unbelievable wealth of wisdom (even if some of it was unsolicited, *no pasa nada*) and even allowing me to sit in on some of your daily debates.

I am very grateful for everyone I had the pleasure of meeting and working with in the CACR and our days in the field. There have been many thought-provoking discussions, countless bug bites, jellyfish stings, sunburns, windburns and laughs. Furthermore, I owe a great deal of gratitude to Maya Eley, without whom I could not have completed this research. You were handed a challenging dataset and rose to the

occasion; it is without doubt that you are now the unparalleled authority in the field of horizontal pressure gradients.

Thank you to my friends and family for pretending to be as interested in sand as I am and for nodding along to my rambling frustration with sensor thingys and coding stuff. Without your unconditional support and patience, I would not be where I am today. Lastly, thank you Carly, for always being my voice of reason and perspective. For your flexibility and willingness to adjust to the chaotic years of moving around the country, long trips home, late nights studying, and me being “too busy” to clean the mess I leave in my wake. I am excited for this new chapter and for you to choose our next adventure.

TABLE OF CONTENTS

LIST OF TABLES vii
LIST OF FIGURES viii
ABSTRACT xv

Chapter

1 INTRODUCTION 1

1.1 Swash Zone and Inner Surf Processes 2
1.2 Sediment Mobility 6

1.2.1 Modes of transportation 7
1.2.2 Incipient Motion 8

1.3 Sleath Parameter and Shields Number Research 11
1.4 Outline 15

2 METHODS 17

2.1 Experimental Setup 17

2.1.1 Study Conditions 20

2.1.1.1 Beach Profile Design 20
2.1.1.2 Waves 22

2.1.2 Instrumentation 29

2.1.2.1 Acoustic Doppler Profiling Velocimeter (ADPV) 35
2.1.2.2 Conductivity Concentration Profiler (CCP) 37
2.1.2.3 Pressure Sensor Array (PSA) 39

2.1.3 Data Acquisition 43

2.2 Data Processing 43

2.2.1 Sediment Concentration 43
2.2.2 Pressure 47

2.2.3 Velocity 48

3 RESULTS 54

3.1 Beach Profiles 54
3.2 Group Averaging 59
3.3 Bed Response Identification 62
3.4 Shields vs Sleath 64

3.4.1 Time Delayed Response 64
3.4.2 Influence on Bed Response 70

3.5 Irregular Waves 73

4 DISCUSSION 77
5 CONCLUSIONS 83

REFERENCES 85

Appendix

A PRESSURE SENSOR ARRAY 94
B GROUP AVERAGES FOR ALL CONDITIONS 96
C TIME LAG COMPARISON OF SLEATH NUMBER AND SHIELDS PARAMETER 104

LIST OF TABLES

Table 2.1: Summary of wave conditions. 24

Table 2.2: Bichromatic Wave Groups 27

Table 3.1: Shields and Sleath statistics for four-wave Bichromatic conditions 70

Table 3.2: Shields and Sleath statistics for irregular wave conditions 76

LIST OF FIGURES

Figure 1.1: Cross-shore beach profile illustrating various zones of interest as well as their respective boundaries..... 5

Figure 1.2: Forces acting on a sediment particle under steady flow conditions (adapted from (Dean & Dalrymple, 2002). 9

Figure 2.1: Grain size distribution of the sediment (provided by Sibelco) used during STB experiment campaign..... 19

Figure 2.2: Image of initial beach profile oriented shoreward. Dividers were installed to minimize longshore effects by reducing the width of the beach face. 20

Figure 2.3: (a) Flume setup up, stationary instrumentation, and beach profile profile schematic for the experiments conducted in the dissipative beach (slope 1:15). Horizontal dimensions represent initial still water shoreline and total length of experimental zone measured from the wave paddle, and the vertical dimension is the still water depth measured from the bottom of the flume (instrument elevation is not to scale; distances measured in meters). (b) Instrument locations within the inner surf and swash zones. (c) Photo of instrumentation deployed at Station 1..... 22

Figure 2.4: Ensemble averages of 2 consecutive wave groups (measured in deep water) from the varying grouping schemes tested in the bichromatic conditions. Conditions (a) B_E3_4W_R1, (c) B_E3_5W_R1, and (e) B_E3_6W_R1 consisted of a single group of 4, 5 and 6 waves, respectively, that was repeated continuously throughout the trial. Conditions (b) B_E3_4W_R2, (d) B_E3_5W_R2, and (f) B_E3_6W_R2 consisted of two slightly different groups that were repeated alternatingly (also containing 4,5, and 6 waves, respectively). 28

Figure 2.5: Images of the sensors used to measure the free surface elevation: (a) RWG (b) long-range AWG, (c) mid- and short-range AWG, and (d) PPT. The sensors were secured to the wall of the flume using 0.03 m diameter stainless-steel tubing..... 30

Figure 2.6: Image showing the (a) ADVs, (b) OBSs, and (c) PPT that were secured to the mobile platform and were used measure the flow characteristics and sediment concentration in the breaking zone of the profile. 32

Figure 2.7: Schematic of mechanical profiling device and mobile platform. The profile is measured using the trigonometric changes in X and Z determined by the change in the angle (α) between the pivoting trail arm and the horizontal. These changes are cross-referenced on the dry portion of the beach with measurements collected using an ultrasonic distance meter (UDM) identified in the schematic as *"Reference Sensor"*. 33

Figure 2.8: (a) Offshore oriented view of the swash zone within the CIEM flume. Measurement stations are shown along the left wall of the flume. (b) Enlarged view of the instrumentation used at station 1. Data from the OBS are not discussed in this thesis. 35

Figure 2.9: Cross-section schematic of ADPV with conceptual operation characteristics in a 2-dimensional flow. 37

Figure 2.10: Image of CCP with labeled components and dimensions. 38

Figure 2.11: Image of (a) MS5837-30BA high resolution pressure transducer, (b) Aluminum housing bolt with recessed MS5837-30BA sensor secured internally, and (c) fabricated sensor array mount with countersunk housing bolts secured through the center of the mount. 42

Figure 2.12: (a) Close-up profile view of the PSA deployed at station 1. (b) Shaded region of instrumented frame depicts the location of the PSA as seen through the viewing window in the flume wall. 42

Figure 2.13: Example merging process of offset CCPs. (a) Upper and (b) lower CCP sediment concentration profiles, reference concentration used to identify instantaneous vertical offset is shown as the white curve. (c) Merged sediment concentration profile. 45

Figure 2.14: Example of sheet flow layer calculation. (a) 300 second clip of sediment concentration profiles with bed level shown as the black curve and the top of the sheet flow layer is represented by the white curve. The red dashed box identifies (b) a zoomed in clip of calculated sheet flow layer thickness. 47

Figure 2.15: Bed identification example. (a) Water depth (relative to SWL) measurements were compared to (b) free stream velocity measurements to verify proper temporal alignment was conducted. (c) CCP sediment concentration data were used as a proxy to compare time dependent bed level changes. (d) Reflected amplitude measurements of ADPV bottom detection pulse, calculated bed location is identified as the white curve. Highlighted region represents the region shown in Figure 2.16. 50

Figure 2.16: Zoomed in depiction of highlighted region from Figure 2.15. (a) Free surface elevation (relative to SWL). (b) Free stream velocity. (c) Sediment concentration with bed level shown as black curve. (d) Reflected amplitudes of ADPV bottom detection pulse with identified bed level shown as white line. 51

Figure 2.17: (a) Example time series of cross-shore free stream velocity for one continuous flow cycle with colored circles representing (b) velocity profiles examined at 0.002 m resolution (identified by corresponding colors). Logarithmic fits (colored curves) are applied to the profiles shown in (b) and corresponding squared correlation coefficients between the data and fitted curves are listed on the left side of the panel. Positive velocities are onshore directed. Negative velocities are offshore directed. 53

Figure 3.1: Beach profile evolution for the energetic (erosive) irregular conditions on the (a) 1:15 and (b) 1:25 sloped profiles compared with less energetic (accretive) irregular condition on the (c) 1:15 and (d) 1:25 sloped profiles. Profiles were measured after each trail (30 minutes for erosive conditions and 60 minutes for accretive conditions) with the colors becoming darker for each successive profile. The accretive condition (I_A1) in (c) was tested immediately following the I_E1 condition. The accretive condition (I_A1) in (d) was tested after all three erosive conditions (I_E1, I_E2, and I_E3) were tested. The reference profile is represented by the black line. The beach was not reshaped between these trials. 56

Figure 3.2: Comparison of the (a) I_E1 wave condition and (b) I_A1 wave condition tested on the 1:15 slope with a closer look at the profile response within the inner surf and swash zones. The reference profile is represented by the black line and the yellow star depicts the location of station 1. 57

Figure 3.3: Profile evolution comparison of the bichromatic wave groupings and repetition sequences during the two experimental campaigns. The repetition sequence is identified by color; orange is the repetition of a single group (R1) and purple is the alternating repetition of two groups (R2). (a) B_E3_4W_R1 and B_E3_4W_R2 on the 1:15 slope. (b) B_E3_4W_R1 and B_E3_4W_R2 on the 1:25 slope. (c) B_E3_5W_R1 and B_E3_5W_R2 on the 1:15 slope. (d) B_E3_5W_R1 and B_E3_5W_R2 on the 1:25 slope. Colors become darker for each successive trial. The reference profile is represented by the black curve..... 58

Figure 3.4: Group averages of (a) relative free surface elevation, (b) Shields parameter, (c) Sleath number, and (d) sheet flow layer thickness for the bichromatic condition B_E3_4W_R1 (4 waves per group with a single group repetition) tested on the 1:15 slope. The black line represents the average values, and the gray lines are the individual realizations used in the averaging scheme. 61

Figure 3.5: Intermittent spikes in bed response are observed in (d). Group averages of (a) relative free surface elevation, (b) Shields parameter, (c) Sleath number, and (d) sheet flow layer thickness for the bichromatic condition B_E3_5W_R2 (4 waves per group with a single group repetition) tested on the 1:15 slope. The black line represents the average values, and the gray lines are the individual realizations used in the averaging scheme..... 62

Figure 3.6: Subplot comparison of (a) free surface, (b) free stream velocity, (c) Shields Parameter, (d) Sleath Number, and (e) sheet flow thickness where the white curve is the corrected sheet flow layer thickness. The gray shaded regions in (a) – (d) and the gray vertical dashed lines in (e) represent the data plotted in the panels on the right. The red vertical dashed line references the temporal location of the peak bed response shown in the lower right panel. 63

Figure 3.7: Example of peak values of (a) free surface elevation, (b) Shields parameter, and (c) Sleath number corresponding to (d) maximum bed responses exceeding 0.008 m. Corresponding peak values are identified by matching colored circles. 66

Figure 3.8: Histogram plots depicting the distribution of time lags between (a) Sleath number and bed response and (b) Shields Parameter and bed response for condition B_E3_4W_R1 on the 1:15 slope; Distribution of time lags between (c) Sleath number and bed response and (d) Shields Parameter and bed response for condition B_E3_4W_R2 on the 1:15 slope..... 67

Figure 3.9: Histograms of the time lags between peak bed response and the (a) corresponding peak Sleath number and (b) corresponding peak Shields parameter for condition B_E3_4W_R1 on the 1:15 slope; Compared with (c) peak Sleath number and (d) peak Shields parameter plotted as a function of the time lag and magnitude of the corresponding peak sheet flow thickness. The red dot denotes the center of mass of the plotted values weighted by the magnitude of sheet flow thicknesses. 69

Figure 3.10: (a) Peak Sleath numbers and (b) peak Shield parameters plotted as a function of peak bed response for condition B_E3_4W_R1 tested on the 1:15 sloped profile. The change in color represents the time lag between the forcing and response. The direction of the flow during peak bed response is illustrated by the shape of the symbol where circles indicate onshore, triangles indicate offshore, and squares indicate an undetermined flow direction. 72

Figure 3.11: Zoomed in depiction of Figure 3.10 for values of peak bed response less than 0.018 m. Plot characteristics are consistent with the description provided for Figure 3.10. 73

Figure 3.12: Histograms of the time lags between peak bed response and the (a) corresponding peak Sleath number and (b) corresponding peak Shields parameter for condition I_E3 on the 1:15 profile; Compared with (c) peak Sleath number and (d) peak Shields parameter plotted as a function of the time lag and magnitude of the corresponding peak sheet flow thickness. The red dot denotes the center of mass of the plotted values weighted by the magnitude of sheet flow thicknesses. 74

Figure 3.13: (a) Peak Sleath numbers and (b) peak Shield parameters plotted as a function of peak bed response for condition I_E3 tested on the 1:25 sloped profile. The change in color represents the time lag between the forcing and response. The direction of the flow during peak bed response is illustrated by the shape of the symbol where circles indicate onshore, triangles indicate offshore, and squares indicate an undetermined flow direction. 75

Figure A.1: Design assembly for pressure array mount and specifications for individual pressure sensors. 95

Figure B.1: Group averages of (a) free surface elevation, (b) Shields parameter, (c) Sleath number and (d) sheet flow layer thickness for condition B_E3_4W_R1 tested on the 1:15 slope profile. The black line represents the average values, and the gray lines are the individual realizations used in the averaging scheme. 97

Figure B.2: Group averages of (a) free surface elevation, (b) Shields parameter, (c) Sleath number and (d) sheet flow layer thickness for condition B_E3_4W_R1 tested on the 1:25 slope profile. The black line represents the average values, and the gray lines are the individual realizations used in the averaging scheme. 98

Figure B.3: Group averages of (a) free surface elevation, (b) Shields parameter, (c) Sleath number and (d) sheet flow layer thickness for condition B_E3_4W_R2 tested on the 1:15 slope profile. The black line represents the average values, and the gray lines are the individual realizations used in the averaging scheme. 99

Figure B.4: Group averages of (a) free surface elevation, (b) Shields parameter, (c) Sleath number and (d) sheet flow layer thickness for condition B_E3_4W_R2 tested on the 1:25 slope profile. The black line represents the average values, and the gray lines are the individual realizations used in the averaging scheme. 100

Figure B.5: Group averages of (a) free surface elevation, (b) Shields parameter, (c) Sleath number and (d) sheet flow layer thickness for condition B_E3_5W_R1 tested on the 1:15 slope profile. The black line represents the average values, and the gray lines are the individual realizations used in the averaging scheme. 101

Figure B.6: Group averages of (a) free surface elevation, (b) Shields parameter, (c) Sleath number and (d) sheet flow layer thickness for condition B_E3_5W_R2 tested on the 1:15 slope profile. The black line represents the average values, and the gray lines are the individual realizations used in the averaging scheme. 102

Figure B.7: Group averages of (a) free surface elevation, (b) Shields parameter, (c) Sleath number and (d) sheet flow layer thickness for condition B_E3_5W_R2 tested on the 1:25 slope profile. The black line represents the average values, and the gray lines are the individual realizations used in the averaging scheme. 103

Figure C.1: Histograms of the time lags between peak bed response and the (a) corresponding peak Sleath number and (b) corresponding peak Shields parameter compared with (c) peak Sleath number and (d) peak Shields parameter plotted as a function of the time lag and magnitude of the corresponding peak sheet flow thickness (condition B_E3_4W_R1 tested on the 1:15 slope profile). The red dot denotes the center of mass of the plotted values weighted by the magnitude of sheet flow thicknesses. 104

Figure C.2: Histograms of the time lags between peak bed response and the (a) corresponding peak Sleath number and (b) corresponding peak Shields parameter compared with (c) peak Sleath number and (d) peak Shields parameter plotted as a function of the time lag and magnitude of the corresponding peak sheet flow thickness (condition B_E3_4W_R2 tested on the 1:15 slope profile). The red dot denotes the center of mass of the plotted values weighted by the magnitude of sheet flow thicknesses. 105

Figure C.3: Histograms of the time lags between peak bed response and the (a) corresponding peak Sleath number and (b) corresponding peak Shields parameter compared with (c) peak Sleath number and (d) peak Shields parameter plotted as a function of the time lag and magnitude of the corresponding peak sheet flow thickness (condition B_E3_4W_R2 tested on the 1:25 slope profile). The red dot denotes the center of mass of the plotted values weighted by the magnitude of sheet flow thicknesses. 106

ABSTRACT

The swash zone and inner surf zones are often the most dynamic regions of the beach in terms of sediment transport processes that govern the morphological change of the shoreline. Yet, there exists a rather weak understanding in the contributing roles of the driving forces that govern sediment mobility and how these relationships are affected by different hydrodynamic forcing conditions, local morphology, phase of flow cycle, and spatial dependence across the swash and inner surf zones. Comprehensive understanding of the variation between horizontal pressure gradients and shear stress influences will greatly aid in the improvement of modelling skill to predict sediment transport. However, existing horizontal pressure gradient datasets are coarse and too limited to draw direct correlations. Modern advancements in sensor technology have enhanced the ability to collect high resolution measurements and further research the relative time-dependent significance of both shear stress and horizontal pressure gradients throughout the flow cycle. A novel low-profile Pressure Sensor Array (PSA) consisting of seven high resolution pressure transducers was developed to measure the horizontal change in pressure. The low-profile design allows for data collection in shallow water applications and reduces flow disruption.

Observations of shear stress and horizontal pressure gradients were collected in a large-scale wave flume during the Shaping The Beach (STB) experiments, conducted in Barcelona, Spain, during September – October 2019, and February – March 2020. Measurements were collected in the transitional region of the lower swash and inner surf zones under varying wave conditions that were tested on two

planar-sloped mobile profiles. Relative time lags between shear stress and bed level fluctuations as well as pressure gradients and bed level fluctuations were examined to determine a temporal correlation between the disruptive forces and bed response.

Shear stresses and horizontal pressure gradients were parameterized as the dimensionless Shields parameter and Sleath number, respectively, to allow for a more generalized parametric comparison. Bed response was identified as the maximum change in bed level elevation exceeding 0.008 m for a given wave, and the corresponding maximum Shields parameter, Sleath number, and associated time lags were compared.

Chapter 1

INTRODUCTION

Throughout history, coastal zones have been areas of high population and particular attraction due to their ability to sustain trade, navigation, resources, and recreation. Currently, many of the most populated cities and areas in the world can be found in coastal zones. Statistics of the exact population living in coastal zones are limited and variable due to the lack of a single definition of what constitutes a "coastal zone" (Crowell et al., 2007). Yet, these statistics become appreciably more definitive by considering a region with a specific spatial buffer from the coast to delineate a coastal zone. Sixty percent of the world's 39 largest cities are located within 100 km of the coast and approximately one quarter of the global population resides both within 100 km of the coast and less than 100 m above sea level (Nicholls et al., 2007; Small & Nicholls, 2003). However, living near the coast presents exposure to a wide range of challenges such as coastal erosion, sea-level rise, tsunamis and potential impacts from increasing storm events.

The beach is a highly dynamic region that acts as a protective mechanism to dampen the effects of some of these issues by exchanging sand onshore and offshore to dissipate wave energy. Relatively low wave heights, commonly found in *calm* conditions, generally transport sediment shoreward giving rise to gradual accretion and promoting beach growth (Beach et al., 1992; Butt et al., 2004). Conversely, energetic waves transport large amounts of sediment offshore causing, more rapid,

beach erosion. Thus, geophysical change can occur over timescales that range from hours to years.

Indeed, there is a fundamental dependence on the hydrodynamic conditions regarding the response of the cross-shore profile of the beach. However, the beach cannot be studied as a singular region when considering sediment transport due to the varying processes and boundary conditions that occur throughout different zones across the beach. The most active morphological change occurs in the inner surf and swash zone when considering hydrodynamic forcing on the migration of sand in cross-shore profile (Alsina & Cáceres, 2011; Butt et al., 2004). A comprehensive understanding of the processes and driving forces of sediment mobility in these zones is needed to best manage and forecast the ability for a beach to mitigate the aforementioned issues.

1.1 Swash Zone and Inner Surf Processes

The oscillatory nature of waves propagating landward and then receding seaward creates a dynamic interface between the beach and the ocean known as the swash zone. The swash zone is often defined as the region between the limits of the wave uprush and backwash. While the upper limit of the uprush is well defined as the extent of runup where the water reaches its maximum elevation, there is some ambiguity in what defines of the seaward boundary of the swash zone. Puleo et al. (2000) suggest another possible definition of the seaward boundary of the swash zone as the location where turbulence generated by the incident bore begins to affect the bed. The swash zone generally exists between the toe of the beach face (or beach step) up to the top of the berm (Figure 1.1). In extreme conditions, the upper limit of the swash zone can reach the dune or back bay/wetlands/inland coastal plain if no dunes

are present (Puleo & Torres-Freyermuth, 2016). However, the exact location of the swash zone is dependent on the instantaneous extent of the uprush and backwash which introduces both spatial and temporal variability in defining swash boundaries (Masselink & Puleo, 2006).

It is within the swash zone that incident waves dissipate or reflect their remaining energy due to the influence of frictional and gravitational forces as well as wave-swash and wave-backwash interactions (Cáceres & Alsina, 2012). During calm (accretive) conditions on a moderately sloped beach face the reflection of energy is dominated by shoreward energy dissipation, resulting in an onshore net sediment flux. On the contrary, larger in magnitude, reflected energy determined by low frequency infragravity waves and/or a steeper beach face profile is generally erosive (Puleo et al., 2000). Sediment may be entrained in the backwash due to energy that is not dissipated, and can be advected offshore. It should be noted that changes in water level will also affect the morphology of the beach face, however, not necessarily because of prominent reflection or dissipation but rather the nearshore zones shift and are acting on areas that were previously shaped by the processes of a different zone.

The hydrodynamic conditions within the swash zone are complex and undergo drastic transformation through a single swash cycle including wide ranges of cross-shore velocities, turbulence, and water depths (Alsina & Cáceres, 2011; Chardón-Maldonado et al., 2016; Puleo et al., 2000). In fact, it has been shown that backwash cannot simply be considered the reverse of the uprush due to the asymmetric nature of swash zone hydrodynamics. Evidence of this is observed as the flow decelerates during the uprush and accelerates during backwash (Aagaard & Hughes, 2006; Astruc et al., 2012; Hughes et al., 1997; Masselink & Puleo, 2006; Puleo et al., 2000). This

asymmetry introduces a strong difference between the two flow regimes. Typically, uprush velocities are large in magnitude but short-lived in duration compared to backwash velocities (Masselink & Hughes, 1998). Another differentiation can be described by the observation of where maximum velocities occur within the uprush and backwash. Maximum uprush velocities are experienced in the beginning of the uprush, whereas maximum backwash velocities are found at the end of the backwash before the transition back to onshore flow takes place. Undoubtedly, the swash zone location and processes are a function of morphology, tidal fluctuations, and both incident and infragravity wave conditions.

Next in offshore succession from the swash zone is the inner surf zone. The inner surf zone is one of two subdivisions that are used to define the surf (or breaker) zone as shown in Figure 1.1. The surf zone is the part of the nearshore that is characterized as the region where waves propagating from offshore begin to break due to shallow water depths and form bores that continue to propagate shoreward to the swash zone. Wave heights and flow characteristics initially undergo rapid changes in the surf zone, however, the change in wave height becomes more gradual after bore formation and the assumption of steady flow can be assumed in a Lagrangian frame (Svendsen et al., 1978; Svendsen & Madsen, 1984). Thus, allowing for a delineation between the inner and outer surf zones, where the inner surf zone is the region in which the wave generated bores propagate from just shoreward of wave breaking to the seaward extent of the swash zone. The gradual change in bore height is due to dissipation primarily controlled by the generation of turbulent kinetic energy and bed friction (Butt et al., 2004; Peregrine, 1983; Puleo et al., 2000; Svendsen, 1984; Svendsen & Madsen, 1984).

In the inner surf zone, the flow cannot simply be considered sinusoidal as the quasi-steady offshore flow (undertow) is coupled with strong onshore accelerations introduced by the leading edge of propagating asymmetric bores (Gallagher et al., 1998; Houser & Greenwood, 2005).

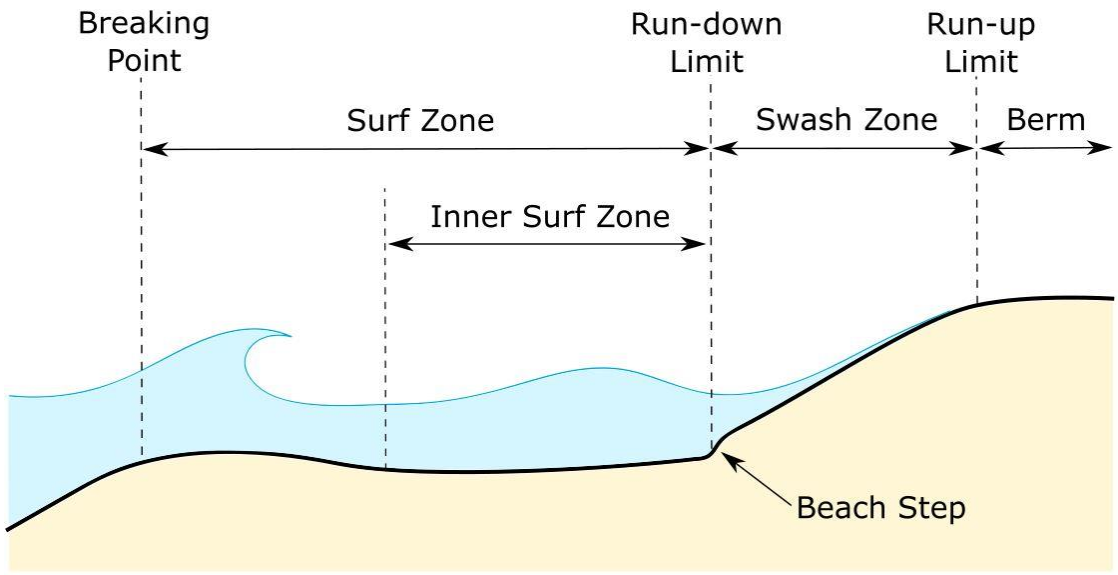

Figure 1.1: Cross-shore beach profile illustrating various zones of interest as well as their respective boundaries.

Although both the swash and inner surf zones are ubiquitous for sediment transport and dissipating wave energy, there are fundamental differences in the hydrodynamics, boundary conditions, and modes of transport that control the processes in these regions. In fact, the swash and inner surf zones cannot be

considered interchangeable, but rather studied independently with a shared boundary such that the processes of one are influential on those of the other (Elfrink & Baldock, 2002; Guard & Baldock, 2007). The shared boundary provides a direct linkage in the evolution of both turbulent and sediment advection. Sediment eroded from the swash zone is exchanged directly to the inner surf where it will either be deposited or continue to be entrained to a farther offshore location. Likewise, sediment transport is exchanged directly from the inner surf to the swash zone in accretive conditions. Accordingly, this direct exchange provides a means to measure the net sediment transport. Yet, the prediction of temporal variability in sediment exchange between these two regions remains unreliable [primarily] due to the coalescence of both locally entrained sediment and advected sediment (Jackson et al., 2004). Additionally, a more comprehensive understanding of the physical mechanisms that control incipient motion of sediment is needed to parameterize the transport processes that are present within these zones.

1.2 Sediment Mobility

Determining the thresholds of flow conditions and mechanisms of incipient motion is a preeminent factor when considering nearshore sediment transport. It is understood that, in a general sense, fluid motion is the basis of sediment mobility in the inner surf and swash zones. Yet, the hydrodynamic processes and forcing mechanisms controlling sediment mobility within these zones are not universal and these differences produce spatial variability in the modes of sediment transport as well as incipient motion. It is worth noting that while aeolian processes contribute to sediment transport on the beach, the upper limit of the swash zone defines the seaward boundary of aeolian effects due to the high moisture content of the sand within the

swash zone restricting incipient motion (Bauer et al., 2009), and therefore is not considered further in this study.

1.2.1 Modes of transportation

Nearshore sediment transport can be differentiated into three modes of subaqueous transport (bed load, suspended load, and wash load) based on their mechanism of movement and subsequent conveyance (Fredsøe & Deigaard, 1992). The wash load consists of very fine sediments held in constant suspension and entrained in the mean flow. Wash load sediments are not generally considered in bed composition and therefore transport associated with wash load is often neglected. This leaves the total load to be divided in the remaining two categories of suspended load and bed load. These two modes of transport are generally differentiated by the forces that govern the mobility of the sediment and the subsequent sediment motion. Suspended load much like wash load, is sediment that is suspended in the water column by turbulent eddies (Middleton & Southard, 1984). However, the sediment sizes are larger than wash load and the suspension is temporary rather than constant. Suspended load is sustained in the water column by turbulent eddies and fluid drag (Bagnold, 1956). On the other hand, bed load transport is identified as sediment that is driven by shear stress and intergranular interactions under the motion of sliding, rolling, saltation, and sheet flow. In general, bed load is typically considered to maintain close enough contact with the bed to not be significantly influenced by flow turbulence. It must be stressed that the vertical delineation between bed load and suspended load is not well-defined due to the temporal changes in flow characteristics promoting transition between the modes of transport.

Rapidly varying water depths, velocities, and turbulence in the inner surf and swash zone are influential on the mode of transportation that may be present at any given phase of the flow cycle within the swash and inner surf zones. A mixture of suspended load and bed load transport exists during the uprush phase of a swash cycle due to bore driven near-bed turbulence; yet, in the absence of large turbulent eddies due limited water depth and negligible flow fluctuations bedload is often the dominant mode during the backwash phase (Horn & Mason, 1994). However, the relative significance in suspended load during the uprush is dependent on the location within the swash. In fact, this may also be the case in the inner surf as well, under specific water depths, due to accelerations associated with asymmetric bores (Houser & Greenwood, 2005). It is evident that to properly predict sediment transport rates models must be able to account for the mode(s) of transport that will occur during different phases of the flow cycle and the driving forces that initiate sediment mobility.

1.2.2 Incipient Motion

A critical threshold of strength in conjunction with hydrodynamic characteristics of the flow must be met to induce incipient motion. A simplified 2-dimensional concept of a sediment particle resting on a submerged bed subject to steady nonturbulent flow (Figure 1.2) can be used to validate the assumption that the particle will begin movement by rotating about the contact point of its downstream neighbor under less force than would be required to lift it into suspension. Dean & Dalrymple (2002) showed that this assumption justifies the efficacy of using of a moment balance rather than the more intuitive force balance.

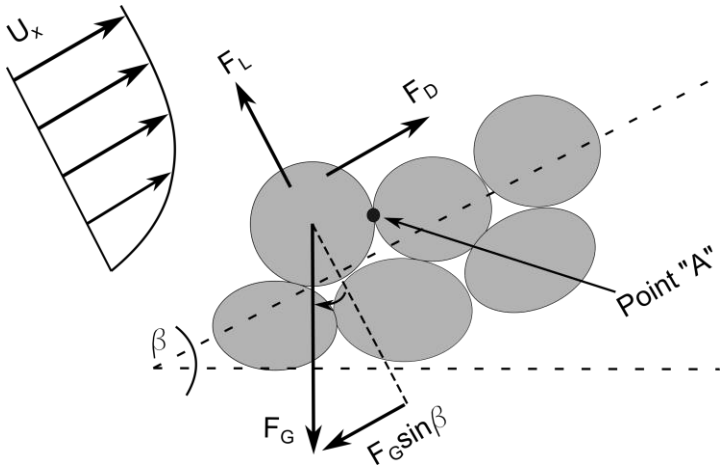

Figure 1.2: Forces acting on a sediment particle under steady flow conditions (adapted from (Dean & Dalrymple, 2002).

The moment balance is given as

$$F_D \alpha_1 d + F_L \alpha_2 d = F_g \alpha_3 d \tag{1.1}$$

Where d is the grain size, α_i (i = 1, 2, 3) are factors used to calculate the proportional moment arm of each force relative to *point A*, and F_L, F_D, and F_G are the forces due to buoyancy, lift, drag, and gravity, respectively. The forces are calculated as

$$F_D = \frac{1}{2}\rho C_D \frac{\pi}{4} d^2 U^2 \tag{1.2}$$

$$F_L = \frac{1}{2}\rho C_L \frac{\pi}{4} d^2 U^2 \tag{1.3}$$

$$F_G = (\rho_s - \rho) g \frac{\pi}{6} d^3 \tag{1.4}$$

Where $(\rho_s - \rho)g$ is the specific weight of the submerged particle and C_D and C_L are dimensionless drag and lift coefficients determined by the Reynolds number ($Re = \frac{u_* d}{v}$) of the flow:

$$Re = \frac{u_* d}{v} \tag{1.5}$$

Where v is the kinematic viscosity and u_* is the near bed shear velocity defined as

$$u_* = \left(\frac{\tau}{\rho}\right)^{\frac{1}{2}} \tag{1.6}$$

and

$$\tau = \frac{1}{8}\rho f U^2 \tag{1.7}$$

is the bed shear stress in which f is the Darcy -Weisbach friction coefficient.

The particle will remain in place at very low flow velocities, U, when the stabilizing forces (gravity and frictional resistance between particles) exceed the driving forces (lift and drag). However, when the driving forces dominate the stabilizing forces the particle will begin to move. Moreover, the driving forces in this conceptual example are governed by the effective bed shear stress when a proportional relationship between the friction coefficient and the drag and lift coefficients is examined. Shields (1936), found that the threshold of incipient motion in quasi-steady flow is parameterized by a ratio between the driving and stabilizing forces acting on a particle. Substituting the expression for shear stress into Eq. (1.1) and nondimensionalizing the ratio of the driving and stabilizing forces

$$\theta = \frac{\tau}{(\rho_s - \rho) g d} \tag{1.8}$$

can be expressed as the Shields parameter, θ.

The preceding example represents a considerable oversimplification of the sediment mobilization mechanisms involved in oscillatory flow in the inner surf and swash zones as it neglects the effects of flow accelerations, the change in pressure

associated with wave passage, and bore injected turbulence. Pressure, relative to the still water level, is increased under the peak of a propagating wave and decreased under the trough. This creates a particularly large horizontal pressure gradient on leading edge of asymmetric bores and near-breaking waves as the flow transitions from offshore to onshore (Madsen, 1974). In fact, Madsen's (1974) research concluded that large pressure gradients associated with steep asymmetric waves can result in a momentary bed failure. Such that, the influence of the change in pressure alters the effective stabilizing forces within the sediment particles on the bed corresponding to the introduction of an additional term, $\partial p/\partial x = \rho U \omega \sin(\omega t)$, applied to the forcing equation (Eq. (1.1)), where t is time and ω is the angular wave frequency. Much like the Shields parameter, the onset of motion can be parameterized by a ratio between pressure induced disruptive force and the stabilizing force of gravity (Sleath, 1999). The non-dimensional ratio, Sleath parameter, was defined as

$$S = \frac{-\frac{\partial p}{\partial x}}{(\rho_s - \rho)g} \tag{1.9}$$

where the sign of S describes the direction of the horizontal pressure gradient (from high to low pressure). The results of Sleath's (1999) research showed that a critical Sleath parameter value of 0.29 was needed to initiate plug flow (sediment particles moving together as a block); however, values much lower than that may promote individual sediment mobility when combined with the effect of shear stress.

1.3 Sleath Parameter and Shields Number Research

Sediment transport has long been estimated using energetics type models (e.g. Bagnold, 1966; Bailard, 1981; Bowen, 1980; Meyer-Peter & Müller, 1948) that have

been formulated in terms of a mobilizing component (shear stress) and transport component (flow velocity) to predict sediment transport in quasi-steady flows. Holistically, these models have been ineffective at predicting sediment transport in the swash and inner surf zones (Aagaard & Hughes, 2006; Butt et al., 2005; Hughes et al., 1997; Masselink & Hughes, 1998; Masselink & Russell, 2006; Puleo et al., 2000) as they lack fundamental forcing mechanisms associated with unsteady flows such as pressure gradients and flow accelerations (Zhao et al., 2011). Energetics type models do present general agreement during the backwash (where pressure gradients, turbulence, and variability in accelerations are negligible) despite the weak predicting skill associated with unsteady flows. Thus, leading to the assumption that shear stress is the dominating force during the backwash phase of the swash cycle. Intuitively, this makes sense as offshore flows on a planar beach can be representative of the quasi-steady stream flow criterion that energetics models were designed for. Puleo et al. (2016) studied the relative importance of different modes of sediment transport during backwash and uprush in the swash zone in the BARDEX II (Masselink et al., 2016) experiment. They found that suspended sediment transport was dominant during the uprush phase of the swash cycle, exceeding sheet flow in some conditions by a factor of 2 which is in good agreement with findings from Puleo et al. (2014). The results of this research provide critical validation to previous research (e.g., Horn & Mason, 1994; Masselink et al., 2005; Puleo et al., 2000) suggesting that suspended sediment was the dominant mode of sediment transport during uprush and expresses the need to explore additional mechanisms of sediment mobility. Moreover, Butt et al. (2009) concluded that phase lags between peaks in velocity and suspended sediment

concentration also suggest that mechanisms other shear stress may promote local bed response.

Horizontal pressure gradients have been introduced to improve model accuracy with promising results (Calantoni & Puleo, 2006; Drake & Calantoni, 2001; Hoefel, 2003; Hsu & Hanes, 2004). The use of a discrete particle model by Drake and Calantoni (2001) found that transient pressure gradients generated sawtooth waves produce moments of intense sheet flow transport and is directly proportional to the fluid acceleration. An acceleration term, calculated from flow measurements, can be added to energetics-based models to account for the effects of the horizontal pressure gradients improving the bed load efficiency by an order of magnitude. Hsu and Hanes (2004) used a two-phase flow model to examine the response of sheet flow transport under unsteady forcing and found that the horizontal pressure gradient is important because particle stress is balanced by the fluid drag. The results showed that, indeed, sediment transport rates cannot be parameterized solely by the effects of velocity and shear stress for certain wave shapes and flow characteristics.

Irrefutably, horizontal pressure gradients are inherent in near-shore gravity wave regimes and the incorporation of a pressure related term in sediment transport formulas has improved modelling accuracy in nearshore coastal applications. Yet validation of the relative importance of horizontal pressure gradients is hindered by the lack of field and/or large-scale experimental measurements. Foster et al. (2006) were the first to provide field evidence of momentary sediment mobilization due to horizontal pressure gradients in the surf zone on a barred beach. Critical Sleath parameter values ($S > 0.1$) were found to be much smaller than the critical values ($S > 0.29$) observed by Sleath (1999) to initiate sediment mobility. The lower critical

values are believed to be attributed to the addition of shear stresses which were not present in the Sleath (1999) study. Foster et al. (2006) suggested that a parameter, Υ, can be used to define the critical threshold of sediment mobilization considering the contribution of the Shields parameter and Sleath number. Rearranging the force balance on the sediment plug provided by Sleath (1999) yields

$$|\Upsilon| = \left|-\theta \frac{d}{h} - S\right| \geq K C_b \tag{1.10}$$

where d is the grain size diameter (often defined by the median grainsize, d_{50}), h is the plug thickness, C_b is the packed bed concentration, and K (set as $K = 0.58$) is the coefficient of static friction. C_b is defined by Bagnold (1956) as

$$C_b = \frac{C_*}{\left(\frac{1}{\lambda}+1\right)^3} \tag{1.11}$$

where C_* is the maximum value of C (=0.74 for uniform spheres), and λ is the average linear concentration

$$\lambda = \frac{d}{\text{mean radial separation distance}}\,. \tag{1.12}$$

Frank et al. (2015) argued that the combined-force sediment mobility parameter, Υ, can be applied to individual particles by removing the ratio of sediment size to plug thickness, d/h, resulting in a simplified equation:

$$\Upsilon = \theta + S \tag{1.13}$$

The initiation of sediment mobilization occurred in the range of ($\Upsilon =$) 0.08 to 0.22.

More recently, the contribution of horizontal pressure gradients in sediment mobility has been studied in a large-scale flume experiment by Anderson et al. (2017). The study focused on 26 different wave conditions over a sandbar profile. It was estimated that horizontal pressure gradients contributed to 33% (ranging from 20% to 45%) of bed erosion initiation. Shorter period, steeper waves typically had a greater contribution to bed failure. The onset of sediment motion occurred at Υ values in the range of 0.09 to 0.20, showing good agreement with the findings from Frank et al. (2015).

Much of the existing research of horizontal pressure gradients has been studied offshore in surf zones where water depths are sufficiently shallow to produce skewed or asymmetric wave characteristics, yet deep enough to allow for continuous measurements throughout the wave cycle. However, it should be noted that there is a lack of horizontal pressure gradient research in the swash zone, likely due to poor measurement capabilities and complexity associated with the rapidly changing water depth, turbulence, and bed level elevation.

1.4 Outline

The research presented in this thesis is part of a larger research experiment, Shaping The Beach (STB), that was conducted by researchers from various Universities to investigate the hydrodynamics, sediment transport processes, and net sediment transport in the swash zone. The highlight of this thesis aims to further understand and improve our knowledge of the correlation between shear stress and horizontal pressure gradients on mobile bed response within the swash and inner surf zones. Both contemporary and novel high-resolution instrumentation were used to measure the hydrodynamic and morphologic response under different forcing

conditions and beach slopes. The results of this research can be used to determine the relative importance and inclusion of governing forces in future sediment transport models.

The varying conditions were tested on an intermediate (somewhat reflective) beach as well as a more mild-sloped (dissipative) beach to.

Chapter 2

METHODS

2.1 Experimental Setup

Measuring and observing inner surf and swash zone processes is extremely difficult due to constantly varying water depths, bed level elevations, wave conditions, and the effects of external influences. A robust cross-shore array of high resolution near bed instrumentation is often needed to capture the temporal and spatial variability of hydrodynamics and sediment transport processes in these regions on natural beaches. The process is further complicated by the labor- and time-intensive need to continuously maintain and service sensor position, power supply, and data storage. On the other hand, large-scale wave flumes allow for repeatability, predictability, and uninterrupted observations in time-relative controlled conditions. All of which aid in analysis of these already complex environments.

The Shaping The Beach (STB) experiment was conducted at the University Polytechnic Catalunya's (UPC) Canal d'Investigació Maritíma (CIEM) large-scale wave flume in Barcelona, Spain. The flume is 100 m long, 3 m wide and 4.5 m deep, with typical working scales of 1:2 to 1:20. The waves are generated in the flume using a wedge-shaped hydraulic piston capable of controlling the variation in wave height and period. The cross-shore coordinate x is defined positively towards the shoreline with the origin ($x = 0$) located at the wave paddle. The vertical coordinate z is defined positively upwards from the concrete bottom ($z = 0$) to the top of the flume ($z = 4.5$ m).

The focus of the study was to investigate nearshore sediment transport processes and cross-shore morphology on two differently sloped mobile bed beach profiles. STB was conducted in two experimental campaigns, where each campaign consisted of the same series of differing hydrodynamic forcing conditions applied to one of the sloped beach profiles to examine the influence of slope on the morphological response to the hydrodynamic conditions. Differing wave conditions were tested during each campaign to provide comparative analysis on the response time and evolution of the beach profile. The sediment used for both experimental campaigns was a fine sand with a median diameter (d_{50}) of approximately 0.25 mm (the sand is well-sorted with σ_{φ} = 0.49; Figure 2.1). The sand was used for the entire profile (x = 33 to 89 m for the 1:15 sloped profile and x = 29 to 89 m for 1:25 sloped profile). Cross-shore walls (dividers) were constructed landward of the shoreline (x = 79 to 84 m for both campaigns) to reduce the generation of longshore effects emphasized by lateral bed asymmetries on the beach face (Figure 2.2). In addition to using the sediment size as a control, a still water level (SWL) of 2.47 m, measured from the bottom of the flume, was consistent for both experimental campaigns of the study.

SAMPLE STATISTICS

SIEVING ERROR: 0,0%

SAMPLE IDENTITY: **50-60** ANALYST & DATE: ,

SAMPLE TYPE: Trimodal, Moderately Well Sorted TEXTURAL GROUP: Sand

SEDIMENT NAME: Moderately Well Sorted Fine Sand

	µm	ϕ
MODE 1:	327,5	1,616
MODE 2:	231,0	2,119
MODE 3:	165,0	2,605
D_{10}:	154,4	1,426
MEDIAN or D_{50}:	245,8	2,024
D_{90}:	372,3	2,695
(D_{90} / D_{10}):	2,411	1,891
(D_{90} - D_{10}):	217,9	1,270
(D_{75} / D_{25}):	1,871	1,573
(D_{75} - D_{25}):	156,0	0,904

GRAIN SIZE DISTRIBUTION

GRAVEL: 0,0%	COARSE SAND: 0,4%
SAND: 100,0%	MEDIUM SAND: 46,8%
MUD: 0,0%	FINE SAND: 52,3%
	V FINE SAND: 0,5%
V COARSE GRAVEL: 0,0%	V COARSE SILT: 0,0%
COARSE GRAVEL: 0,0%	COARSE SILT: 0,0%
MEDIUM GRAVEL: 0,0%	MEDIUM SILT: 0,0%
FINE GRAVEL: 0,0%	FINE SILT: 0,0%
V FINE GRAVEL: 0,0%	V FINE SILT: 0,0%
V COARSE SAND: 0,0%	CLAY: 0,0%

	METHOD OF MOMENTS			FOLK & WARD METHOD		
	Arithmetic	Geometric	Logarithmic	Geometric	Logarithmic	Description
	µm	µm	ϕ	µm	ϕ	
MEAN ($\bar{x}$):	266,6	251,7	1,990	241,7	2,049	Fine Sand
SORTING (σ):	83,87	1,401	0,486	1,415	0,501	Moderately Well Sorted
SKEWNESS (Sk):	0,089	-0,372	0,372	-0,066	0,066	Symmetrical
KURTOSIS (K):	2,191	2,011	2,011	0,678	0,678	Platykurtic

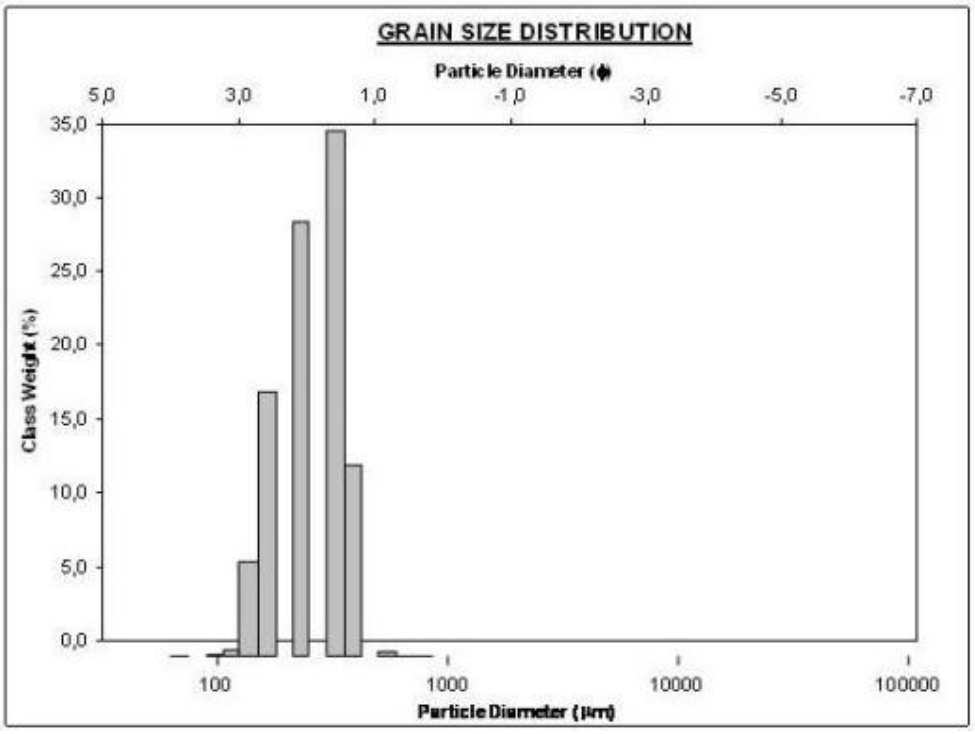

Figure 2.1: Grain size distribution of the sediment (provided by Sibelco) used during STB experiment campaign.

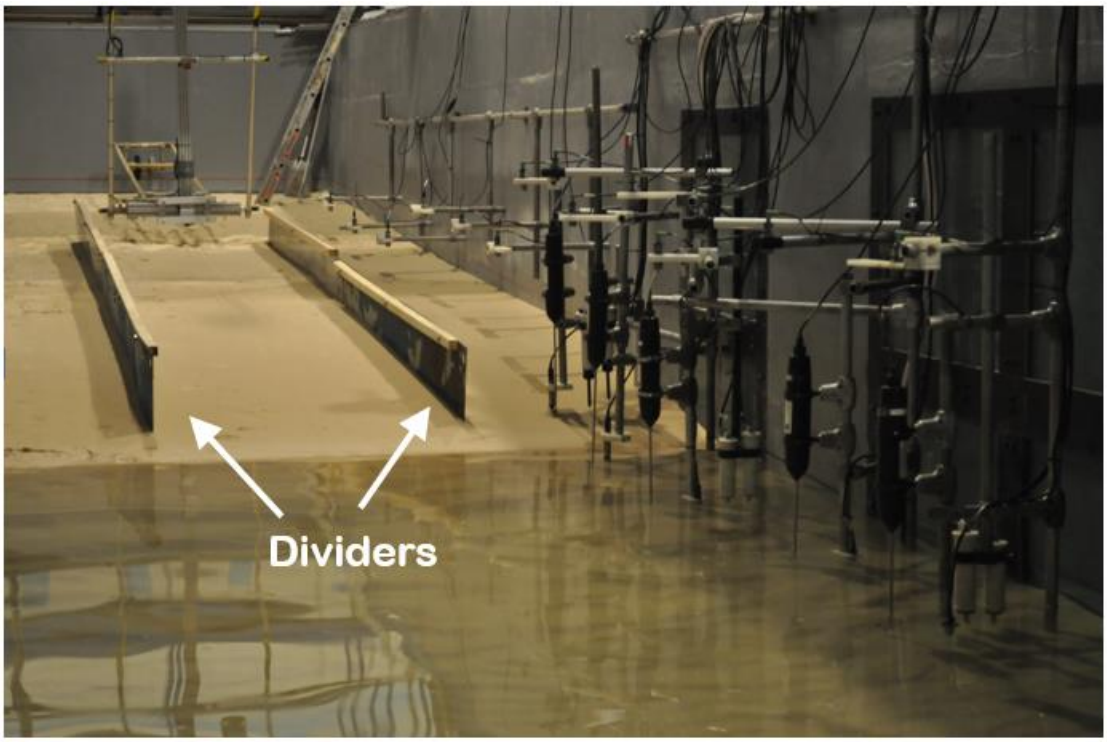

Figure 2.2: Image of initial beach profile oriented shoreward. Dividers were installed to minimize longshore effects by reducing the width of the beach face.

2.1.1 Study Conditions

A series of different wave conditions were used on two planar-sloping beach profiles to examine the influence of the driving forces of sediment mobility and the response of the beach.

2.1.1.1 Beach Profile Design

In a general sense, the profile of a beach is the result of the dynamic shoreline response which serves as a buffer to dissipate wave energy. Already broken waves that propagate shoreward as bores lose much of their energy to turbulence and friction. Much like ballistic motion (and neglecting the effects of pressure), the remaining kinetic energy is converted to potential energy as the fluid slab propagates up the

beach until it has completely decelerated, and the flow is reversed. Mildly sloped beaches force waves to break farther offshore and increase the duration in which bottom friction is effective, thus slowing the onshore-to-offshore flow transition. The gradual transition allows entrained sediment to be deposited as mobilizing forces are reduced. In contrast, a beach that is too steep is unable to dissipate as much energy through friction resulting in more kinetic energy being converted to potential energy and a more rapid flow reversal. The increased turnaround in flow reduces the settling time for mobilized sediments and can result in offshore transport as the remaining energy is projected offshore. Two differently sloped planar beach profiles were used in the experiments to further investigate how a more dissipative beach and a less dissipative beach affect the hydrodynamic forcing and the rate of morphological change associated with various wave conditions tested (described in section 2.1.1.2). Profile specifications within the flume are presented in Figure 2.3.

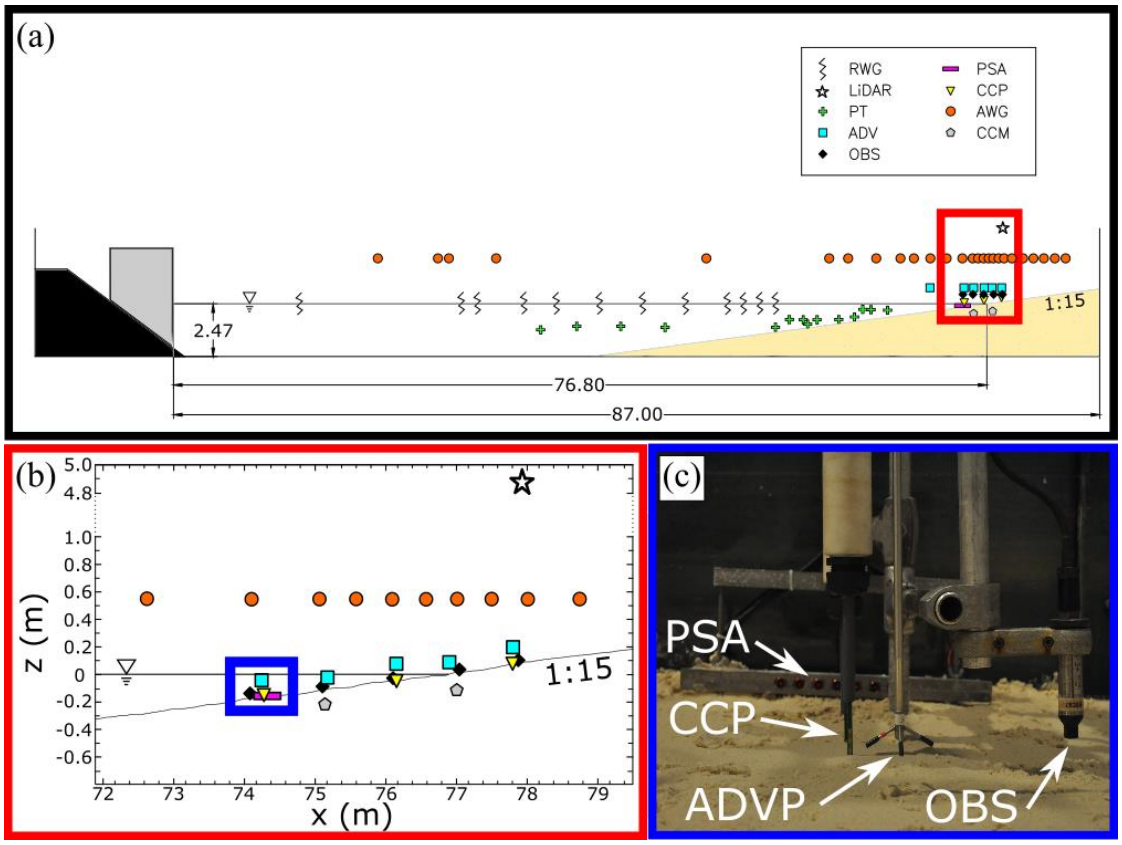

Figure 2.3: (a) Flume setup up, stationary instrumentation, and beach profile profile schematic for the experiments conducted in the dissipative beach (slope 1:15). Horizontal dimensions represent initial still water shoreline and total length of experimental zone measured from the wave paddle, and the vertical dimension is the still water depth measured from the bottom of the flume (instrument elevation is not to scale; distances measured in meters). (b) Instrument locations within the inner surf and swash zones. (c) Photo of instrumentation deployed at Station 1.

2.1.1.2 Waves

Wave trials were conducted using a series irregular and bichromatic waves consisting of both erosive and accretive conditions for the irregular waves and varying number of waves per group (N_w) and group repetitions within the bichromatic

conditions (Table 2.1). The trials were repeated multiple times in series at set durations to complete a total duration time for each condition.

The irregular wave conditions were subdivided into three erosive conditions with progressively increasing wave energies (I_E1, I_E2, I_E3) and one accretive low energy condition (I_A1). The irregular wave conditions were determined to be erosive or accretive based the criterion developed by Kraus et al. (1991) where the prediction of beach change is influenced by the significant wave height (H_s), wave period (T), and the settling velocity of the beach sediment (w_s). A wave field on a given beach is determined to be erosive for

$$\Omega = \frac{H_s}{w_s T} \geq 3.2, \tag{2.1}$$

and accretive for

$$\Omega = \frac{H_s}{w_s T} < 3.2. \tag{2.2}$$

Conditions I_E1, I_E2, and I_E3 had values of Ω equal to 3.78, 4.62, and 5.46 respectively, while I_A1 was equal to 1.41.

Condition I_A1 was tested following the first erosive condition over the 1:15 slope and following the third erosive condition over the 1:25 slope, to examine the rate of response and overall recovery of the beach. In an idealized experiment, the accretive condition would be run until the reference profile was restored but the timescales of beach recovery are much longer than those of erosion. Moreover, the reference profile was a planar slope and will likely never be completely restored as the continuous evolution trends to a nonlinear equilibrium state. Regardless, the accretive condition was still tested for 10 trials at 60 minutes per trial for a total duration of 600 minutes to examine the rate of recovery.

Table 2.1: Summary of wave conditions.

Wave Type	Condition Type	T_p (s)	H_s (m)	Condition ID	N_t	D (min)	D_T (min)	N_w	Trial ID (Phase 1)	Trial ID (Phase 2)
Irregular	Control	4	0.42	Benchmark	4	15	15		1, 52, 65, 78	1, 31, 44, NA
Irregular	Erosive	3.5	0.45	I_E1	6	30	180		(4-9)[a]	2-7
			0.55	I_E2	6				20-25	8-13
			0.65	I_E3	6				26-31	14-20
	Accretive	5.2	0.25	I_A1	10	60	600		(10-14)[a] 15-19	21-30
Bichromatic	Erosive	3.5	0.65	B_E3_4W_R2**	8	30	240	4	53-60	32-39
				B_E3_5W_R2**				5	66-73	45-47, (48-52)[b]
				B_E3_6W_R2**				6	79-82, 87-91	NA
				B_E3_4W_R1*	4		120	4	61-64	40-43
				B_E3_5W_R1*				5	74-77	(53-56)[b]
				B_E3_6W_R1*				6	83-86	NA

N_t = Number of trials conducted for given conditions.
N_w = Number of waves per group.
D = Duration of individual trial.
D_T = Total duration of condition.

* Denotes group phase repetition was after every group.

** Denotes group phase repetition was after every two groups.

[a] Data from CCPs and PSA were not available for given trials.

[b] Data from PSA were not available for given trials.

Note: Conditions B_E3_6W_R2 and B_E3_6W_R1 were not tested during the second phase of the experiment due the outbreak of the Covid-19 pandemic.

Natural ocean waves are comprised of many frequencies that alter the response of the beach and influence swash dynamics. Laboratory realizations of irregular waves, although often analogous to waves experienced on a natural beach,

introduce nonrepeatable complexities that are difficult to analyze for coherent trends and interdependencies. On the contrary, bichromatic waves have been shown to produce similar erosional and accretive evolution as irregular waves while still producing repeatability (Baldock et al., 2011). Bichromatic waves consisting of identical wave heights and periods but varying waves per group and group sequencing were tested to investigate the effects of long period infragravity waves on swash related sheet flow dynamics (Figure 2.4). Previous research has shown that as incident waves propagate shoreward the energy from higher frequencies dissipates and is transferred to the lower group frequency and other harmonics (Baldock et al., 2000; Janssen, 2003; van der Zanden et al., 2015) and on shallow sloping foreshore profiles swash energy in the infragravity band is dominant (Aagaard & Hughes, 2006; Chardón-Maldonado et al., 2016; Hughes et al., 2014). The surf similarity parameter (also known as the Iribarren number, ξ_o) is used to classify the types of breaking waves that occur in the nearshore, depending on the wave steepness and beach slope (Battjes, 1974). Where ξ_o is defined as

$$\xi_o = \frac{\tan\alpha}{\sqrt{H_o/L_o}} \tag{2.2}$$

and $\tan\alpha$ is the beach slope, H_o is the deep-water wave height, and L_o is the deep-water wavelength. Waves are classified as spilling breakers for surf similarity numbers less than 0.5 and are often indicative of a shallow sloped beach, relative to the wave field, where infragravity bands dominate the swash energy scales. Additionally, the period of wave grouping has been shown to be an important factor in the influence of

infragravity and incident bands affecting swash zone hydrodynamics, sheet flow layer dynamics, and cross-shore sediment advection (Alsina et al., 2018).

The bichromatic wave conditions for this experiment consisted of three sets of wave groupings with different number of waves per group, N_w = 4, 5, and 6, as well as two varying group phase repetitions, denoted by *R1* and *R2* at the end of the condition label. The repetition was controlled by modulating the phase of the incident waves such that conditions ending in *R2* contain two alternating wave groups with the same number of waves and energy flux and conditions ending in *R1* have a single wave group that is repeated continuously. The group period, T_g, was calculated using

$$T_g = \frac{1}{f_1 - f_2}, \tag{2.3}$$

where f_1 and f_2 are the frequency components that construct the bichromatic signal. Repetition periods, T_R, for single group conditions are equal to the group period and $T_R = 2T_g$ for the two group conditions. All bichromatic conditions had similar wave height components, $H_1 = H_2 = \sim 0.32$ m, to generate a combined significant wave height of H_s = 0.65 m and equal mean incident wave period of T_p = 3.5 s; calculated using

$$T_g = \frac{2}{f_1 + f_2}. \tag{2.4}$$

The equal wave height and period produces an equal incident wave energy content, Ω = 5.46. Corresponding bichromatic wave group characteristics are listed in Table 2.2. The surf similarity numbers for bichromatic conditions were calculated as ξ_o= 0.36 and ξ_o= 0.22 for the 1:15 and 1:25 slopes, respectively.

Erosion at station 1 (discussed in Section 2.1.2) was larger than anticipated during conditions B_E3_6W_R1 and B_E3_6W_R2. Therefore, results from these conditions are not presented in this thesis due to unobtainable near-bed measurements.

The flume was drained, and the beach was manually restored to the reference profile between the irregular and bichromatic conditions as well as before the adjustment of number of waves per group (N_w) within the bichromatic conditions. A benchmark (or control) condition was run following the beach profile reshape to provide initial bed compaction and beach moisture content prior to the start a new condition sequence.

Table 2.2: Bichromatic Wave Groups

Wave conditions	Component 1		Component 2			
	H_1 (m)	f_1 (Hz)	H_2 (m)	f_2 (Hz)	T_g (s)	T_R (s)
B_E3_4W_R2	0.3251	0.3214	0.3251	0.2500	14.00	28.00
B_E3_4W_R1	0.3248	0.3175	0.3248	0.2540	15.75	15.75
B_E3_5W_R2	0.3252	0.3143	0.3252	0.2571	17.50	35.00
B_E3_5W_R1	0.3250	0.3117	0.3250	0.2597	19.25	19.25
B_E3_6W_R2	0.3253	0.3095	0.3253	0.2619	21.00	42.00
B_E3_6W_R1	0.3248	0.3077	0.3248	0.2637	22.75	22.75

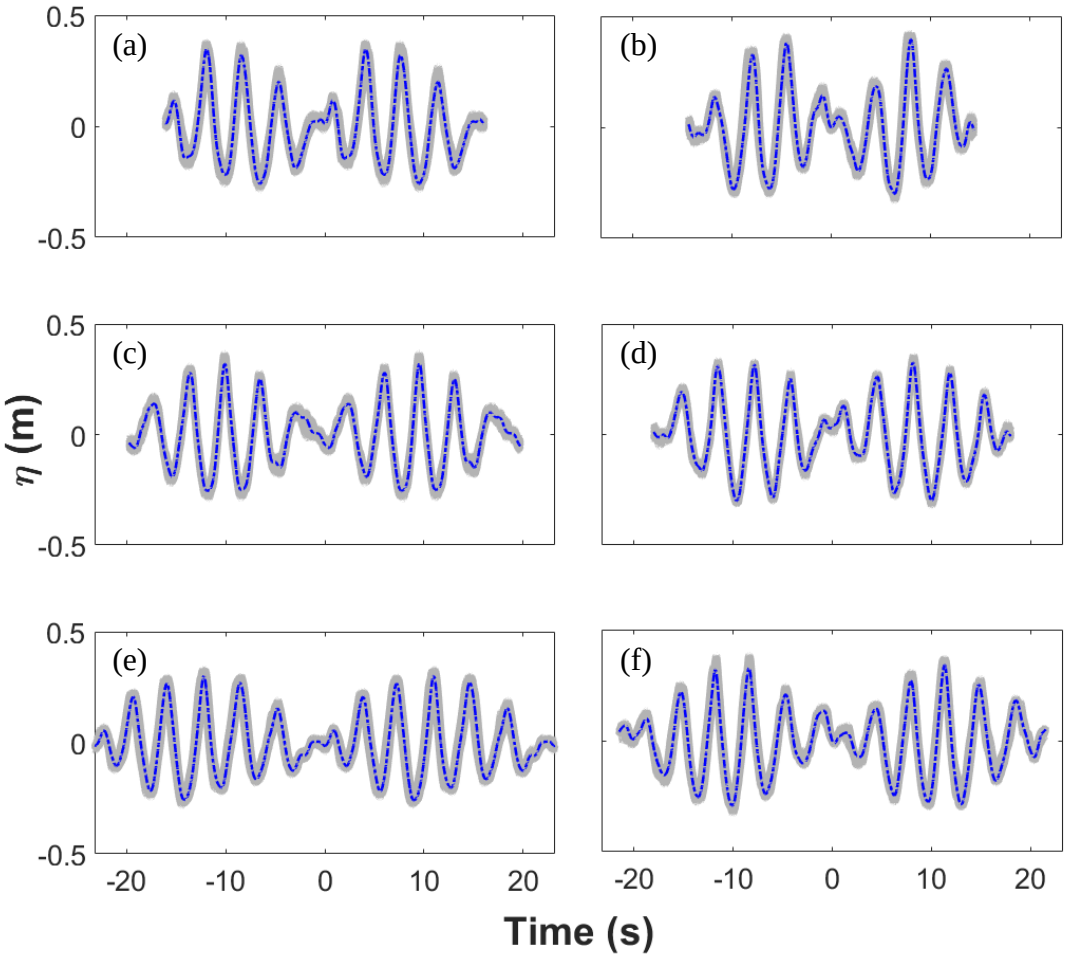

Figure 2.4: Ensemble averages of 2 consecutive wave groups (measured in deep water) from the varying grouping schemes tested in the bichromatic conditions. Conditions (a) B_E3_4W_R1, (c) B_E3_5W_R1, and (e) B_E3_6W_R1 consisted of a single group of 4, 5 and 6 waves, respectively, that was repeated continuously throughout the trial. Conditions (b) B_E3_4W_R2, (d) B_E3_5W_R2, and (f) B_E3_6W_R2 consisted of two slightly different groups that were repeated alternatingly (also containing 4,5, and 6 waves, respectively).

2.1.2 Instrumentation

Free surface elevations were measured from beyond the surf zone to the shoreward limit of the swash zone using 12 Resistance Wave Gauges (RWGs), 26 Acoustic Wave Gauges (AWGs), and 14 Pore Pressure Transducers (PPTs) and remained fixed in position for both campaigns (Figure 2.2a and Figure 2.3a). The RWGs measure the current flowing between two stainless-steel wires (each 1.5 mm in diameter). The current is converted into an output voltage proportional to the depth of submergence that is set to zero for a given initial water depth. Wave heights are measured on the principle that the voltage drop across two resistors is supplied to a precision rectifier to produce a DC voltage (± 10 V) proportional to the wave height that can be calibrated using the change between two known water depths (Figure 2.5a). The RWGs were positioned offshore of the surf zone can measure wave heights up to 2 m (x = 11.8 to 56.6 m) The AWGs emit ultrasonic pulses that reflect off the surface of the measurement object, the sensor receives the pulse as an echo and outputs a voltage (0 to 10 V) proportional to the measured distance. The sensors are calibrated at known distances to transform the intensity of the signal to the proportional distance. Three models of AWGs (ULS-40D, mic+130, and mic+350) were used during the experimental campaign to accommodate the need to collect a varying range of measured distances. Ten ULS-40Ds were deployed at varying offshore locations to collect long-range measurements of wave heights propagating from the deep water through the outer surf zone (x = 19.2 to 69.5 m; Figure 2.5b). Twenty-three mic+130 mid-range sensors were used in the inner surf and swash zones (x = 70.9 to 80.8 m) and three mic+350 short-range sensors were used to measure the

swash on the upper beach face (x = 81.7 to 83.8 m; Figure 2.5c). The AWGs were deployed at 1 m spacing in the nearshore and upper beach face (x = 73 to 75 m and x = 78.8 to 83.8 m, respectively) and 0.5 m spacing through the inner surf and swash zones (x = 75.5 to 78 m). AWG positions within the inner surf and swash zones vary slightly between the two campaigns due to re-deployment constraints. The PPTs (STS ATM/N; Figure 2.5d) can measure changes in free surface elevation through the linear relationship between hydrostatic pressure and water depth without interference from nearby sensors allowing for increased spatial resolution. The PPTs were deployed between the RWGs in deep water (approximately 4 m spacing) and within close proximity (< 2 m spacing) to one another in the breaker zone to better resolve the location of waves breaking. Three PPTs (x = 56.6, 59.6, and 64.8 m) were removed prior to the second campaign to reduce the risk of local scour near the bed.

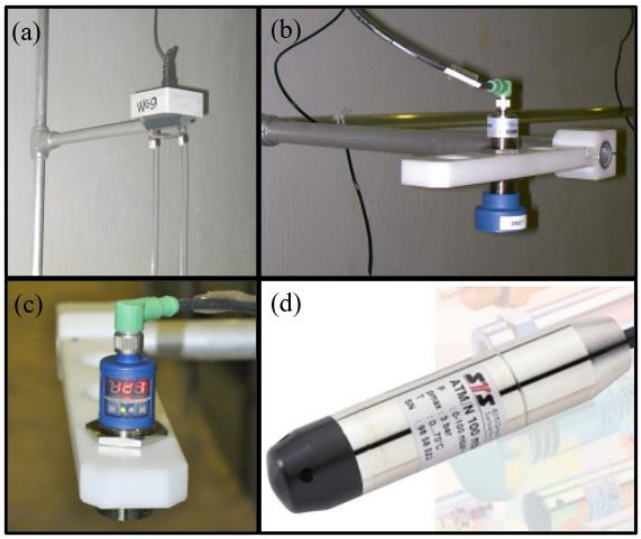

Figure 2.5: Images of the sensors used to measure the free surface elevation: (a) RWG (b) long-range AWG, (c) mid- and short-range AWG, and (d) PPT. The sensors were secured to the wall of the flume using 0.03 m diameter stainless-steel tubing.

Flow characteristics of the wave field and suspended sediment concentration in the breaking region of the surf zone were obtained using 3 Acoustic Doppler Velocimeters (ADVs), 3 Optical Backscatter Sensors (OBSs), and an additional PPT (Figure 2.6). The ADVs (Nortek Vectrino Velocimeter; Figure 2.6a) collect point measurements of the flow velocity using the Doppler effect by transmitting short pairs of sound pulses and measuring the change in pitch and time lag of the reflected sound with a measuring range of 3 to 15 mm. The OBSs (Campbell Scientific OBS-3+) measures suspended solids and turbidity by detecting infrared light scattered by the suspended particles. The OBSs were calibrated using a sediment sample in a replicated apparatus developed by Downing & Beach (1989). The aforementioned "surf zone" instruments were secured to a mobile platform that could be positioned at the appropriate location (horizontally and vertically) to capture wave breaking as the sandbar migrated throughout the duration of the campaign.

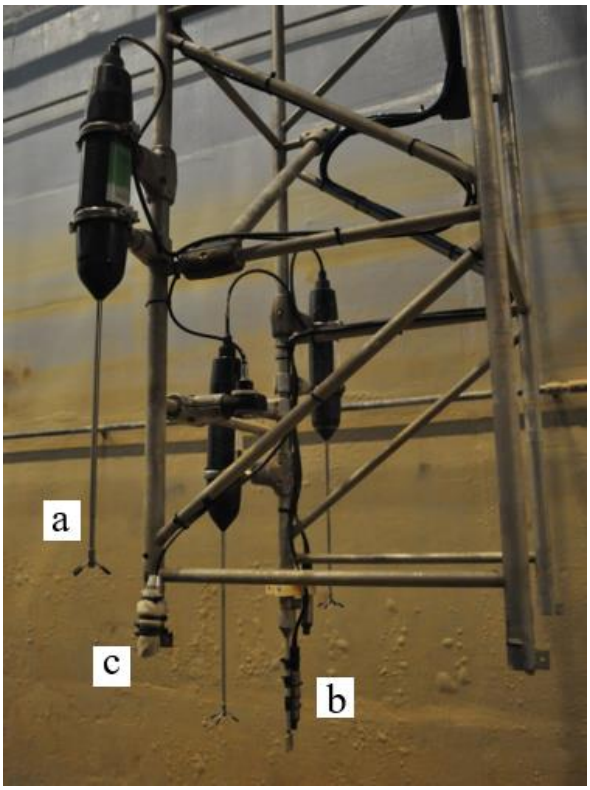

Figure 2.6: Image showing the (a) ADVs, (b) OBSs, and (c) PPT that were secured to the mobile platform and were used measure the flow characteristics and sediment concentration in the breaking zone of the profile.

A second mobile platform was used to measure morphological change in the beach profile after each trial with a mechanical profiling device within an accuracy of approximately 1 cm (Figure 2.7). The device measures elevation changes using a wheel connected to a trailing arm (with vertical free range of motion) that rolls along a cross-shore transect along the flume centerline. Right-angle trigonometry is used to translate the change in angle between the trail arm and the horizontal plane to vertical distance (z). The mechanical profiler is calibrated to a known elevation that is measured using an ultrasonic distance meter (UDM). Survey data were used to

estimate the morphological change across the profile under the assumption any change was uniform in the longshore.

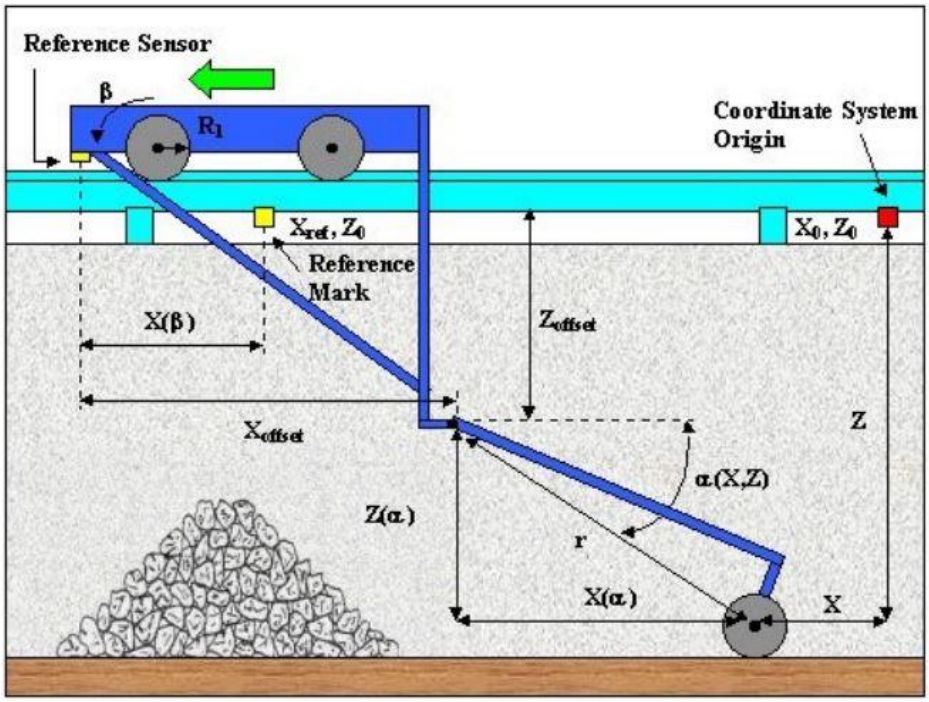

Figure 2.7: Schematic of mechanical profiling device and mobile platform. The profile is measured using the trigonometric changes in *X* and *Z* determined by the change in the angle (α) between the pivoting trail arm and the horizontal. These changes are cross-referenced on the dry portion of the beach with measurements collected using an ultrasonic distance meter (UDM) identified in the schematic as *"Reference Sensor"*.

Flow velocities, suspended sediment and sheet flow layer concentrations, bed and water elevations, and pressures were measured in the inner surf and swash zones at 5 data collection stations (spaced approximately 1 m apart at x = 74 to 78 m) on the 1:15 slope beach and at 8 data collection stations (x = 73 to 80 m on the 1:25 slope beach). Data were collected using 4 ADVs, 1 Acoustic Doppler Velocity Profiler

(ADPV; discussed further in section 2.1.2.1), 6 Conductivity Concentration Profilers (CCP; discussed further in section 2.1.2.2), 2 conductivity concentration measurement tanks (CCMs), 5 OBSs, 1 Pressure Sensor Array (PSA; discussed further in section 2.1.2.3), and 1 Light Detection And Ranging (LiDAR) sensor (an additional 3 CCPs were used to measure the upper swash during the second campaign). The sensors located in the swash and inner surf zones were secured by a custom-built frame, spanning a cross-shore distance of 5 m (1:15) and 8 m (1:25), using 0.03 m diameter stainless steel tubing that was designed to minimize flow disruptions while also being sufficiently rigid to withstand wave impact. The frame was mounted to horizontal support bars that spanned the length of the flume wall.

The work presented in this thesis will focus on the velocity, pressure, and sediment concentration data collected at the most seaward station containing CCPs (referred to hereafter as Station 1; located at x = 74 m during the first campaign and x = 75.3 m during the second; Figure 2.8).

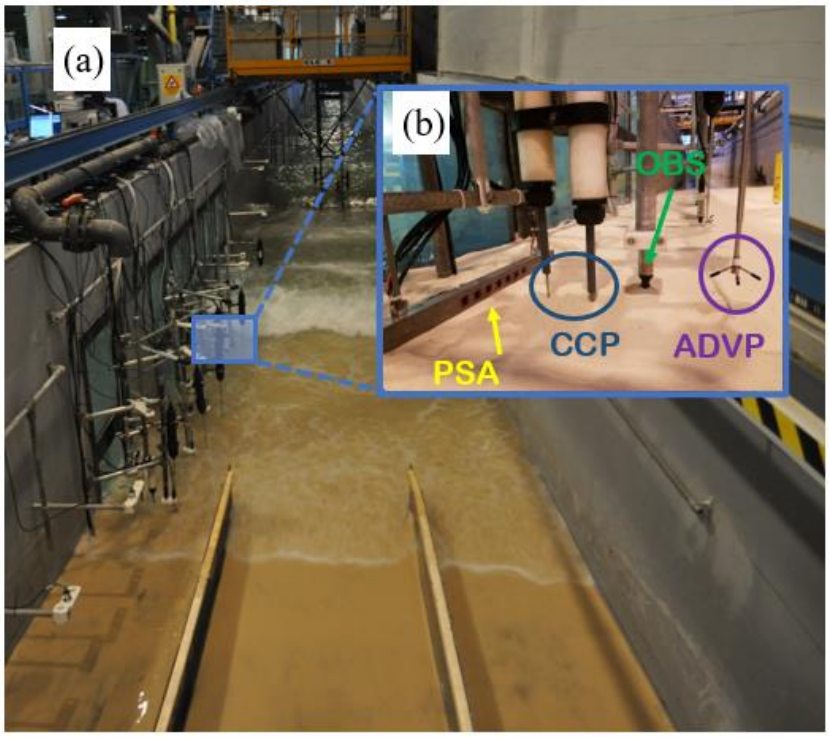

Figure 2.8: (a) Offshore oriented view of the swash zone within the CIEM flume. Measurement stations are shown along the left wall of the flume. (b) Enlarged view of the instrumentation used at station 1. Data from the OBS are not discussed in this thesis.

2.1.2.1 Acoustic Doppler Profiling Velocimeter (ADPV)

Accurate and highly resolved near bed velocity measurements collected during the onset of motion are crucial in determining sediment mobility and subsequent transport. Collecting these measurements in the swash and inner surf zones is challenging due to limited measurement range in the water column, turbulence and aerated induced signal interference, as well as varying bed elevations (Blenkinsopp et al., 2011; Masselink & Puleo, 2006; Masselink & Russell, 2006). Furthermore, the intermittent absence of water across the swash zone makes it impossible to measure velocities of a full swash event at certain locations. In fact, a full swash event itself is

discontinuous in flow in an Eulerian frame located where the bed fully re-emerges (Puleo et al., 2000). Much of the associated research from a few decades ago has been focused in the surf zone where bed elevations are more stable and adequate water depths allow for longer periods of sensor submergence. However, recent advancements in sensor technology have paved the way for both higher temporal resolution and more spatially robust measurements (O(0.01 s) and O(0.001 m) respectively), furthering the collection field to near instantaneous vertical velocity profiles from the bed. The ability to collect measurements closer to the bed (< 0.03 m above the bed; e.g. Puleo et al., 2012) has shown good agreement with energetics based models (Bagnold, 1966) during backwash.

Flow velocities at station 1 were collected at 100 Hz using a downward-looking ADPV (Nortek Vectrino II Profiler; Figure 2.8b) that measures cross-shore, longshore, and vertical velocities in a 0.03 mm vertical profile at 0.001 m resolution. The ADPV, much like the ADVs, emits acoustic pulses from a central transducer and receives the reflected signal through four receiving prongs to measure the change in pitch between the output and input signals (Figure 2.9). Velocities are measured using the Doppler effect at 31 points in a range of 0.04 to 0.07 m below the central transducer. The multi-point sampling allows for the vertical structure of streamwise velocity profile to be collected while near-bed (~ 0.001 m) velocities are still obtained as the bed level fluctuates within measuring range. The ADPV was deployed at x = 74.25 m for the first campaign and x = 75.25 m for the second campaign and ~ 0.6 m from the flume wall (y = ~ 0.6 m) for both campaigns. The vertical height of the central transducer was adjusted between trials to maintain ~ 0.05 m above the bed to ensure that near-bed velocities remained within range for the duration of each trial.

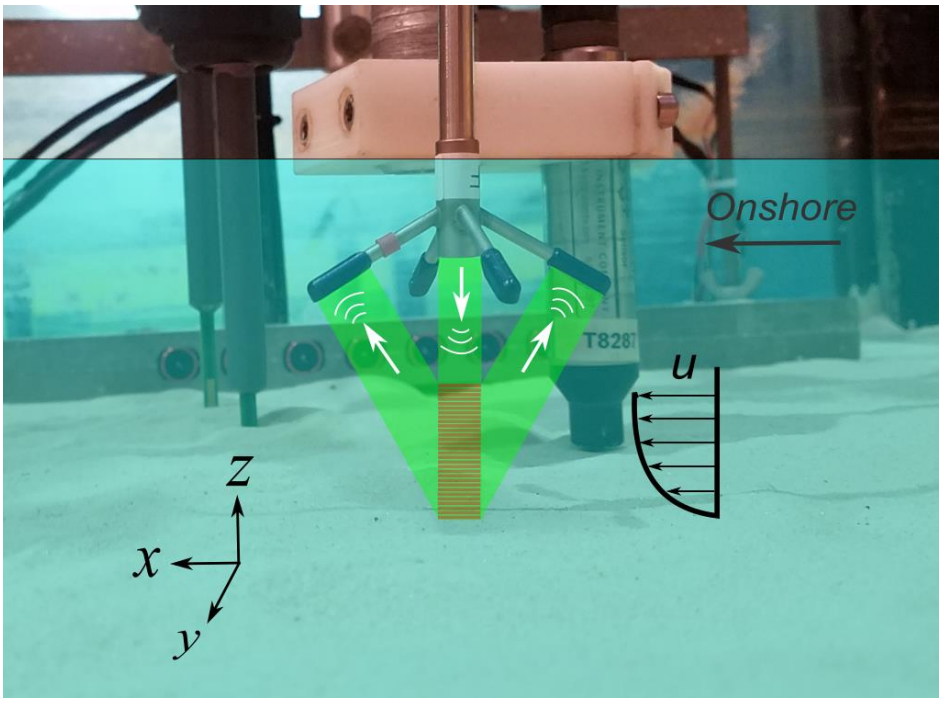

Figure 2.9: Cross-section schematic of ADPV with conceptual operation characteristics in a 2-dimensional flow.

2.1.2.2 Conductivity Concentration Profiler (CCP)

Instrumentation capable of recording time-dependent sheet flow thickness is another modern development that has greatly contributed to the research effort in inner surf and swash zone sediment transport. The thickness of the sheet flow is highly variable, often *O*(10 to 100 times the diameter of the sediment), and is dependent on the local flow characteristics (Ribberink & Al-Salem, 1995). Conductivity-based instruments have been found to be the most reliable for measuring high sheet flow concentrations (100 to 1600 g/L), where measurements are made using the linear relationship between sediment concentration and the electrical conductivity of a sediment-water mixture (van der Zanden et al., 2013). The method was first used by Horikawa et al. (1982), and led to the development of a point measuring Conductivity

Concentration Meter (CCM) by Ribberink & Al-Salem (1995) that was later improved to a multi-point sampling system capable of moving in the vertical direction with a fixed offset to also collect velocity measurements. However, the CCM is still unable to measure the vertical concentration profile of the sheet flow layer. A Conductivity Concentration Profiler (CCP; mentioned in section 2.1.2) was developed by Puleo et al. (2010) that was composed of eight electrode pairs and could measure the voltage response across each pair, but the sensor probes proved to promote appreciable scour and flow disturbance. The CCP design was later improved by Lanckriet et al. (2013), to streamline the sensor probes and increase sampling resolution by incorporating 32 electrode plates onto a printed circuit board that was 5.6 mm wide and 1.6 mm thick (Figure 2.10). The new design enables increased versatility in the deployment of the CCP such that it can be suspended with the probe extended downward into the bed or, contrarily, buried with the probe pointing upwards.

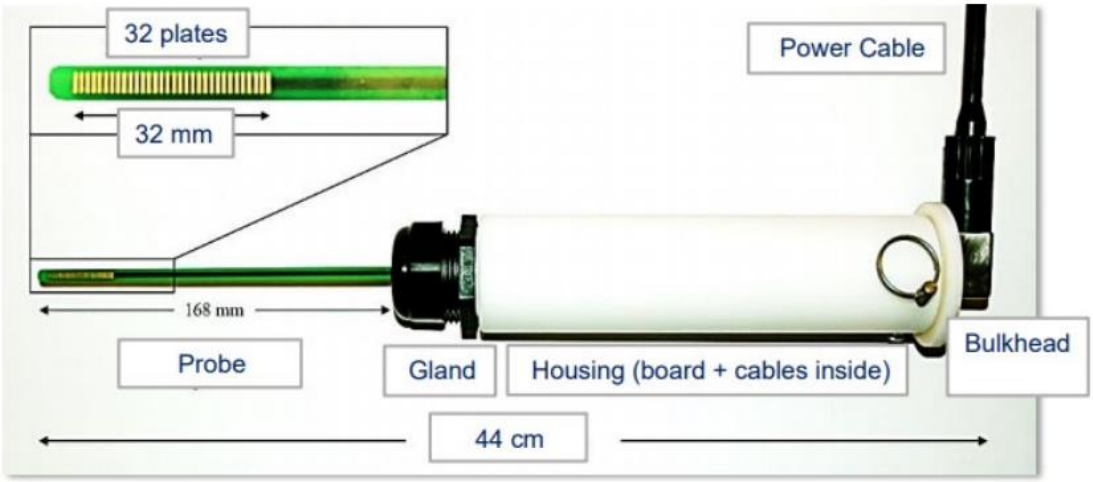

Figure 2.10: Image of CCP with labeled components and dimensions.

A pair of CCPs was deployed concurrently at the same cross-shore location (x = 74.3 m and 75.4 m for the first and second campaigns, respectively) with ~ 0.04 m separation in the spanwise direction. The CCP pair was suspended above the bed with a fixed vertical offset of 0.026 m from each other to increase the vertical range from 0.029 m to 0.054 m while still providing enough overlap to ensure a continuous field of measurement. The downward measuring deployment was chosen to allow for vertical adjustments to be made between trials while the CCPs were submerged to maintain the fluid/sand interface was still in the measurement frame.

2.1.2.3 Pressure Sensor Array (PSA)

Pressure gradients in the nearshore are difficult to measure directly due to the specific requirements that must be met for a sensor to effectively collect highly resolved change in pressure without altering the flow dynamics and local bed evolution. Presently, there a very few devices available that offer adequate spatial resolution, unobtrusive streamlined design, and durability to meet the complexities present in the near shore environments. Alternative techniques, such as using the slope of the free surface (e.g. Baldock & Hughes, 2006) or the acceleration of the free stream velocity (e.g. Foster et al., 2006), have been used to estimate horizontal pressure gradients in lieu of collecting direct pressure measurements. However, the approximation of horizontal pressure gradients using the acceleration of the free stream collected from single point velocity measurement lacks contribution from convective acceleration terms, such that

$$\frac{DU}{Dt} = -\frac{1}{\rho}\frac{\partial p}{\partial x} \tag{2.5}$$

becomes

$$-\frac{\partial p}{\partial x} = \rho \frac{\partial u_\infty}{\partial t} \ . \tag{2.6}$$

It is important to note that the convective accelerations are not negligible in the inner surf and swash zones and consideration of only the local acceleration, $\frac{\partial u_\infty}{\partial t}$, leads to a critical underestimate of the horizontal pressure gradient (Baldock, 2012).

An array of seven high-resolution pressure sensors (labeled P_1, P_2, P_3, P_4, P_5, P_6, and P_7 from offshore to onshore) was assembled to calculate the change in pressure between each sensor. The sensors (MS5837-30BA from TE Connectivity; Figure 2.11a) are small (3.3 m diameter and 2.75 mm thick) and water resistant (gel-coated transducer), while also capable of measuring pressure at a resolution of 2 mbar up to a depth a 300 m. The sensor uses an I^2C bus interface to allow for communication across a variety of available microcontrollers. An aluminum mount was fabricated to hold the sensors at a uniform height of 0.01 m above the bottom of the mount and fixed horizontal spacings of 0.03 m to collect measurements over a range of 0.18 m (detailed dimensions are shown in Appendix A). Each sensor was independently recessed in a hollowed-out anodized aluminum bolt housing (supplied by BlueRobotics; Figure 2.11b) to increase durability and ensure the wired connections were sufficiently water-proofed. The bolts were countersunk into the mount so that the sensors were flush with the face of the array to minimize flow disturbance (Figure 2.11c). A swivel was built into the upper brace of the mount enabling the PSA to be adjusted to the slope of the bed (Figure 2.12).

Independent sensor connection was maintained to address the need of sensor replacement in case of malfunction. Waterproof heat shrink was used to run the

connection leads from each sensor out of the flume up to a microcontroller operated by the Arduino Integrated Development Environment (IDE) software. The MS5837-30BA pressure sensors have a common fixed I^2C address thus restricting simultaneous communication from the microcontroller. This issue was resolved by incorporating a multiplexer (TCA9548A; supporting communication protocols of 100 and 400 kHz) to serve as a gateway that cycles the communication from the microcontroller through each sensor.

Data were collected at 50 Hz and manually saved to the laptop operating the PSA during the first experimental campaign. Manual data storage limited the sampling duration to 18 minutes, at which time the PSA was stopped, the data were saved, and data acquisition was reinitiated. A data logger (Adalogger FeatherWing) was integrated with the microcontroller prior to the second experimental campaign to increase sampling frequency to 100 Hz and eliminate interruptions in the time series by increasing sampling duration. The data logger enabled automatic storage to a microSD capable of storing entire time series as well as including a real time clock to eliminate constant time transmission from the computer.

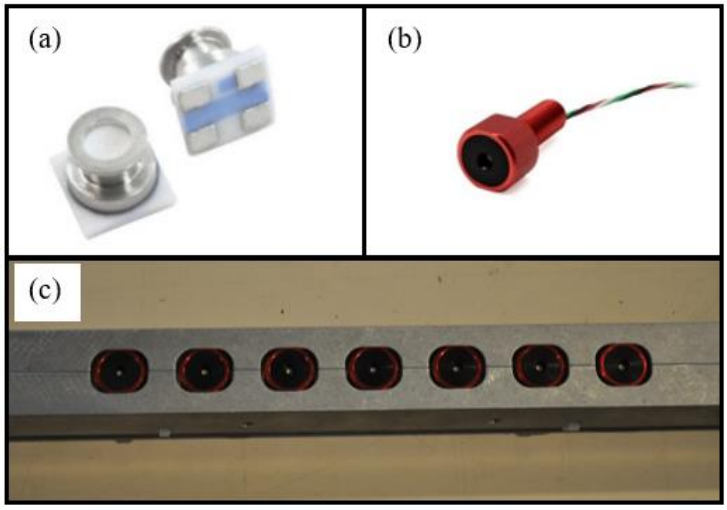

Figure 2.11: Image of (a) MS5837-30BA high resolution pressure transducer, (b) Aluminum housing bolt with recessed MS5837-30BA sensor secured internally, and (c) fabricated sensor array mount with countersunk housing bolts secured through the center of the mount.

Figure 2.12: (a) Close-up profile view of the PSA deployed at station 1. (b) Shaded region of instrumented frame depicts the location of the PSA as seen through the viewing window in the flume wall.

2.1.3 Data Acquisition

The sensors used in this study were powered and operated from independent computers and were manually initiated prior to the start of each trial. An additional computer was used to record a 5 V voltage jump transmitted from the wave maker that signaled the start of the trial. The voltage jump remained at 5 V for 5 seconds before returning to 0 V and was recorded at 100 Hz. The recorded timestamps received from the individual computers were synchronized using an allocated computer that functioned as a master time server. The time server received Coordinated Universal Time (UTC) using a Global Positioning System (GPS) antenna and updated the linked computer clocks through Network Time Protocol (NTP) software. Time synchronization was updated across all the computers every second to mitigate temporal drift.

2.2 Data Processing

2.2.1 Sediment Concentration

Two CCPs were located offshore (one in fluid without any suspended sediment and the other buried in the packed bed) and used as controls to measure pure fluid conductivity and packed bed concentrations. The control measurements were used to convert CCP data from station 1 from electrical conductivity to sediment concentration using Archie's Law

$$\frac{1}{F} = \frac{\sigma_m}{\sigma_f} = \phi^m = (1-c)^m , \tag{2.7}$$

where F is the formation factor, σ_m is the conductivity of the mixture, σ_f is the conductivity of the fluid, $\phi = (1-c)$ is the porosity of the bed, and m is a calibration factor (Archie, 1942; Lanckriet et al., 2013). A MATLAB Graphical User Interface

(GUI) was used convert the conductivity to sediment concentration of the measuring CCPs by taking the conductivity measurements of the control CCPs as inputs to and calculating the appropriate calibration factor for each trial.

Although the CCP pairs were set to a fixed vertical offset, slight variations in bed level fluctuations were observed between the two CCPs, complicating the process of merging the CCP measurements to a uniform time series. Differences in concentrations measured across the vertical profile were plotted in a histogram to determine a well-defined fluid/sand interface concentration that could serve as a reference to measure the instantaneous vertical offset. A concentration of 0.35 m^3/m^3 was chosen to define the reference elevation because concentrations below 0.35 m^3/m^3 dropped off rapidly to pure water measurements and concentrations above 0.35 m^3/m^3 increased rapidly as the volume of sediment in the bed became denser. A time dependent identification of the reference concentration in both CCPs was used to calculate the offset between the two corresponding elevations identified and the profiles were shifted to remove the vertical offset (Figure 2.13). Measurements that were closest to 0.35 m^3/m^3 ($\pm$0.04 m^3/m^3) for each timestep were compared to the three measurements above and the three measurements below to ensure that identified elevation was valid and not an outlier mistakenly identified. In the event that the identified elevation was determined to be invalid the next closest corresponding concentration was considered. The preceding offset was used if no concentrations within the range of acceptable values were identified or if the instantaneous change in offset exceeded 0.004 m. If the reference concentration was identified too low in the upper CCP, the lower CCP would be used, and the offset would be added to the profile. Likewise, if the reference concentration was identified too high in the lower

CCP, the upper CCP would be used, and the offset would be subtracted from the profile.

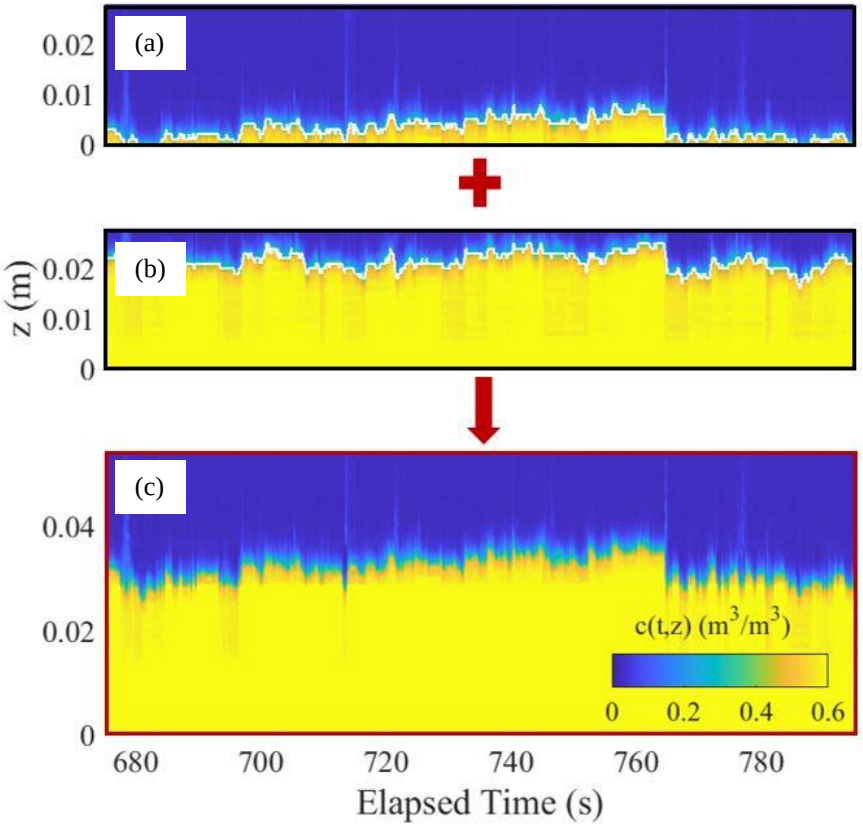

Figure 2.13: Example merging process of offset CCPs. (a) Upper and (b) lower CCP sediment concentration profiles, reference concentration used to identify instantaneous vertical offset is shown as the white curve. (c) Merged sediment concentration profile.

The merged sediment concentration profile was used to determine the instantaneous bed level elevation (also referred to as the bottom of the sheet flow layer) by identifying the sharp concentration transition in the profile much like the

merging process previously discussed. However, this procedure used a composite power law to fit a curve to the transition using a boxcar window with a width of 3 vertical samples and extrapolating a linear curve from the inflection point to the intersection of a vertical tangent line extended from the packed bed ($c(t) > 0.6$ m^3/m^3; Lanckriet et al., 2014; Mieras et al., 2017; O'Donoghue & Wright, 2004). The top of the sheet flow layer was identified as the elevation where sediment concentrations transitioned from $c(t) > 0.08$ m^3/m^3 to $c(t) < 0.08$ m^3/m^3 (refer to Lanckriet et al. (2014) and Mieras et al. (2017) for a more comprehensive description of CCP bed identification). The measured sheet flow layer thickness is found by calculating the difference in elevation between the top of the sheet flow layer and the instantaneous bed level (Figure 2.14). The measured sheet flow layer maintains a nominal thickness of up to 0.005 m due limited vertical resolution and the smoothing of the concentration profile. A correction formula developed by Lanckriet et al. (2014) was used to remove the smoothing effect

$$\frac{\delta_m}{\delta_r} = \frac{1}{713\times10^3\delta_m^2 - 6024\delta_m + 21.9} + 1 \tag{2.8}$$

Where δ_m is the sheet flow layer thickness measured by the CCP and δ_r is the real sheet flow layer thickness.

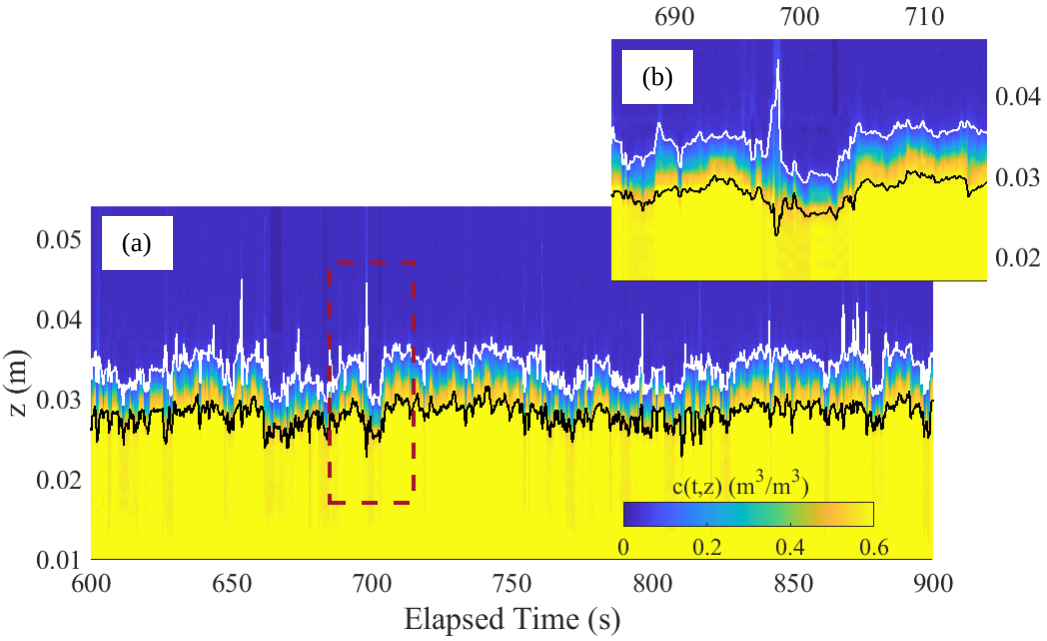

Figure 2.14: Example of sheet flow layer calculation. (a) 300 second clip of sediment concentration profiles with bed level shown as the black curve and the top of the sheet flow layer is represented by the white curve. The red dashed box identifies (b) a zoomed in clip of calculated sheet flow layer thickness.

2.2.2 Pressure

The data collected using the Pressure Sensor Array (PSA) were first filtered using an acceptable range for the data; points that fell outside of this range were eliminated. The acceptable range was determined on a trial-by-trial basis, but 990 mbar – 1080 mbar was most frequently used. The remaining data were then compared against an initial maximum for slope magnitude; 5 mbar per sample was used as the maximum slope magnitude for all trials. If two consecutive points created a slope that

exceeded this magnitude, the first data point was eliminated, while the second point remained in the dataset.

Next, the slopes between the remaining points were plotted on a histogram to determine a more appropriate slope magnitude maximum on a trial-by-trial basis. Most frequently, a slope magnitude of 1 mbar/s was used. Slopes larger than the refined maximum were identified and both data points were eliminated.

Then, the indices of eliminated data points were saved and a simple linear interpolation was used to temporarily fill the gaps in the data. The interpolated data were passed through MATLAB's detrend function to eliminate hydrostatic pressure due to the height of the free surface. The temporary interpolations were then eliminated from the data. Finally, the data were smoothed using a second order Savistky-Golay filter.

The filtered, smoothed data was then used to calculate the Sleath number over time. For nearly all trials, a fourth-order centered difference approximation was used to calculate the Sleath number. However, pressure sensor 6 failed to collect data for Trials 59-64. In these cases, a second order centered difference formula was used to approximate the Sleath number.

2.2.3 Velocity

Velocity data were post-processed to address dry readings, pulse-to-pulse interference, and measurements collected when the bed was out the sampling range of the ADPV. Dry readings can occur when water levels drop to low and the sensor head and transducers are no longer submerged, as well as when the flow is highly turbulent and laden with air bubbles. Valid measurements were determined to have a self-

similarity (or correlation) greater than 60% and a signal-to-noise ratio greater than 10 dB.

Once the data were properly treated, an algorithm was used to identify the time dependent location of the bed. Bed level was determined as the maximum amplitude, greater than -5 dB, of the reflected acoustic pulse received by the central transducer measured at a resolution of 0.001 m. The ADPV transmitted and received a bottom detection pulse at a frequency of 10 Hz which was interpolated to the time series of the velocity profiles allowing for bed detection at every timestep (100 Hz). Estimated bed levels were compared to measurements collected by the CCP (previously mentioned in section 2.2.1) to verify the accuracy of the algorithm (Figure 2.15). The algorithm performed with a mean variation in bed level change between the two sensors of 0.002 m, a standard deviation of 0.0014 m, and average root mean squared error (RMSE) of 0.91. Velocity data identified as measured below the bed were considered redundant echoes caused by surface reflection of the pulse and were removed.

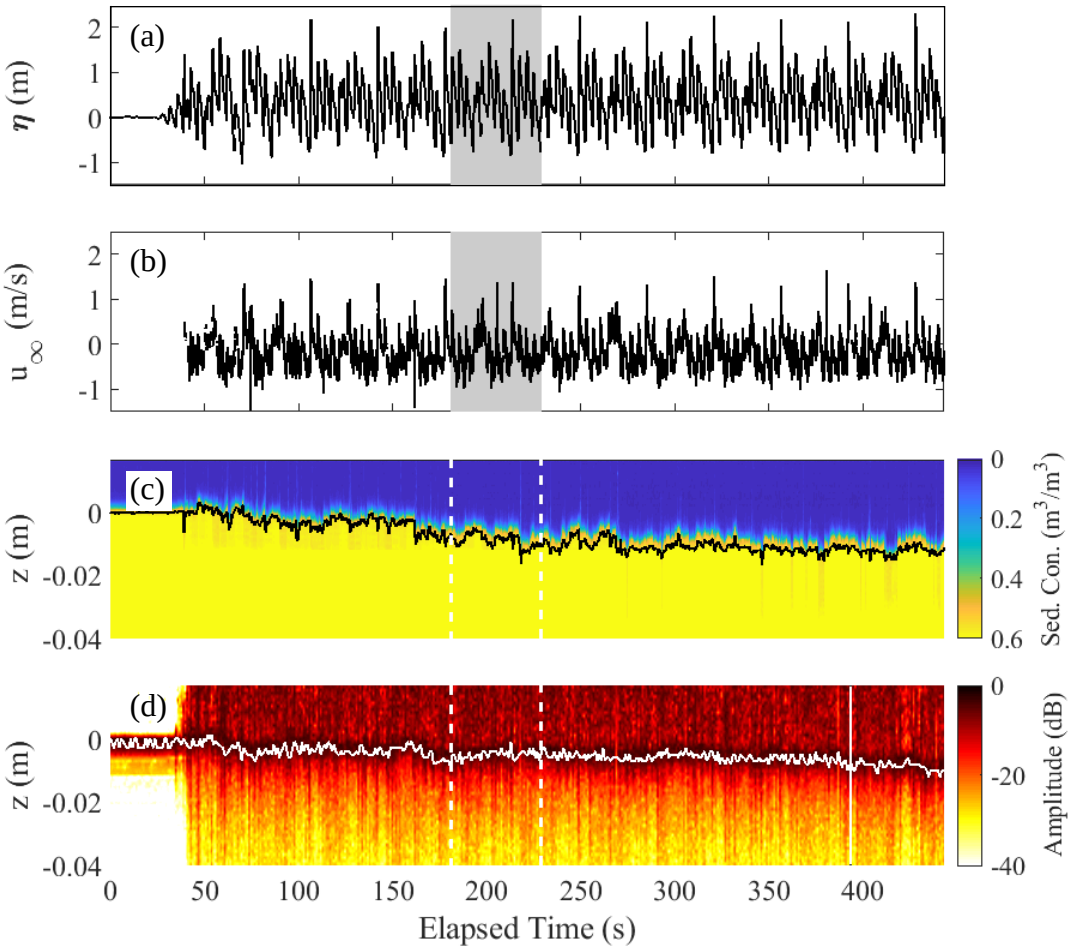

Figure 2.15: Bed identification example. (a) Water depth (relative to SWL) measurements were compared to (b) free stream velocity measurements to verify proper temporal alignment was conducted. (c) CCP sediment concentration data were used as a proxy to compare time dependent bed level changes. (d) Reflected amplitude measurements of ADPV bottom detection pulse, calculated bed location is identified as the white curve. Highlighted region represents the region shown in Figure 2.16.

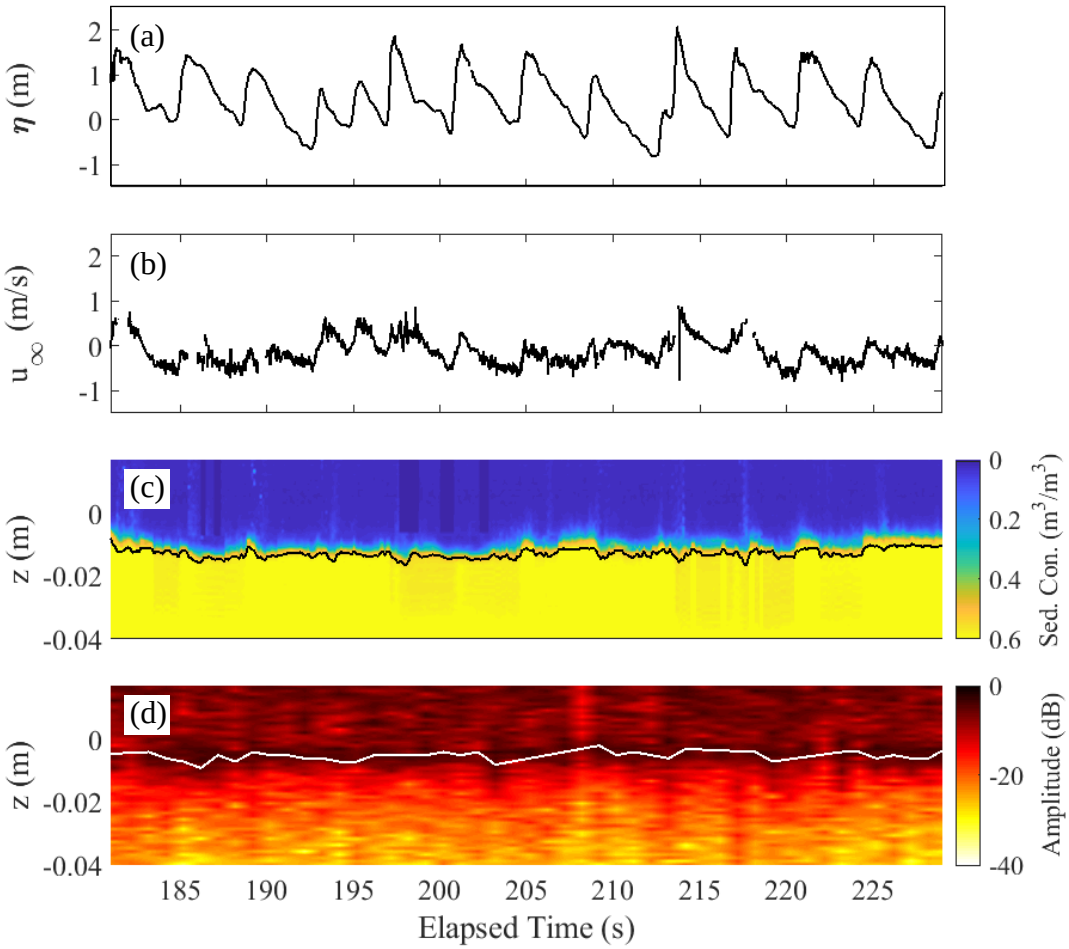

Figure 2.16: Zoomed in depiction of highlighted region from Figure 2.15. (a) Free surface elevation (relative to SWL). (b) Free stream velocity. (c) Sediment concentration with bed level shown as black curve. (d) Reflected amplitudes of ADPV bottom detection pulse with identified bed level shown as white line.

Shear stress is often estimated using free stream or depth averaged velocity (Eq. 1.7) under the assumption that the quadratic drag law is valid and the relationship is parameterized by an empirical friction factor, *f*. It has been shown that variability in *f* is largely dependent on the choice of velocity used and the elevation at which the

velocity is measured (extensively discussed by Puleo et al., 2012). Shear stress can be calculated with less uncertainty using the logarithmic shape of velocity profiles in fully developed boundary layers to obtain the frictional velocity, u_*. The logarithmic shape, *u(z)*, is described in the von Karman-Prandtl equation as

$$u(z) = \frac{u_*}{\kappa} \ln\left(\frac{z - d_*}{z_0}\right) \tag{2.9}$$

where z_0 is the roughness height, κ is the von Karmen constant (0.4), and d_* is the displacement distance. Obtaining u_* is useful in that it provides a direct relationship to shear stress that is illustrated by rearranging Eq. 1.6 to

$$\tau = \rho u_* |u_*| \tag{2.10}$$

where | | maintain the direction of the shear stress.

A logarithmic profile was fit to the vertical structure of the retained velocity profiles using the methods described by Puleo et al. (2012) to determine u_*. Curves that had a squared correlation coefficient, r^2, less than 0.9 to measured data were considered poorly fit and were not used in the calculation of shear stress. The calculated shear stresses were used to determine the corresponding Shields parameter presented in the results of this study. Velocity profiles near flow reversal were generally in poor agreement with the logarithmic law, which was expected as directional transition of the flow occurs non uniformly at different elevations in the water column (Figure 2.17).

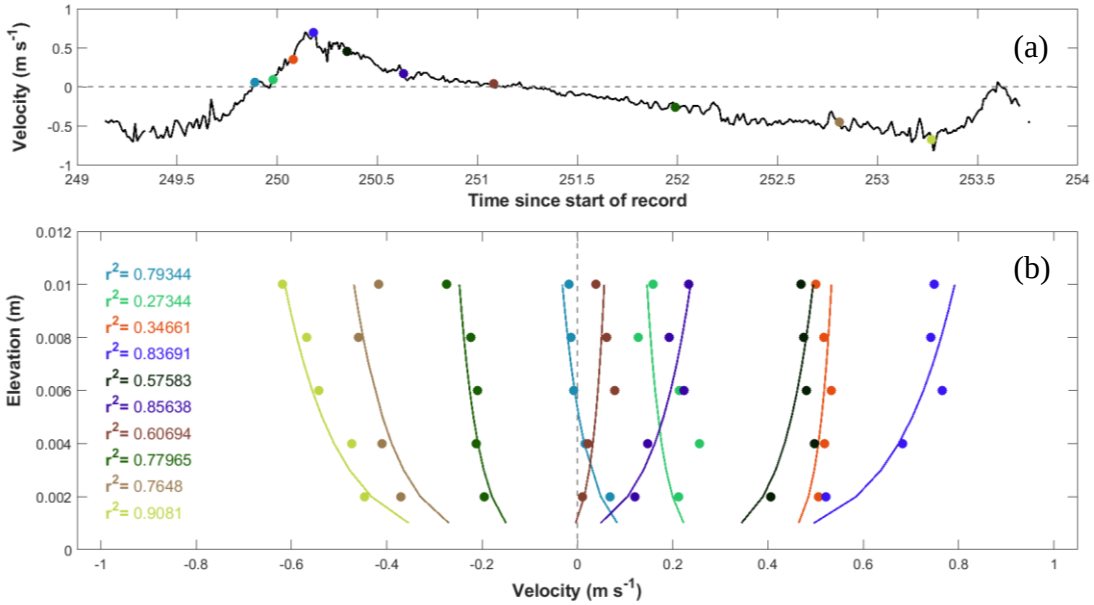

Figure 2.17: (a) Example time series of cross-shore free stream velocity for one continuous flow cycle with colored circles representing (b) velocity profiles examined at 0.002 m resolution (identified by corresponding colors). Logarithmic fits (colored curves) are applied to the profiles shown in (b) and corresponding squared correlation coefficients between the data and fitted curves are listed on the left side of the panel. Positive velocities are onshore directed. Negative velocities are offshore directed.

Chapter 3

RESULTS

3.1 Beach Profiles

A reference profile was measured after each reshaping of the beach and the profile was remeasured between subsequent trials. Rapid morphologic response was observed during the initial trials of each different wave condition, but the rate of change became more gradual as the beach profile equilibrated to the forcing conditions.

The rate and extent of both erosion and recovery of the irregular waves on both profiles were used as a proxy to compare the similarity of controlled bichromatic wave conditions to natural waves of equal incident wave energy. Three irregular energetic wave conditions of varying energy levels (previously described in Section 2.1.1.2) were used to gauge the range of response exhibited by the profile evolution. A less energetic condition (I_A1) was tested following the erosive conditions to assess the ability of the beach to recover (Figure 3.1). Wave condition I_A1 was tested following condition I_E1 during the first experimental campaign as greater morphologic change was anticipated for the 1:15 sloped profile and this sequence offered the greatest chance of maximum recovery. The sandbar was observed migrating shoreward and sediment was deposited onto the beach face during I_A1. However, the inner surf and lower swash zones experienced much greater local erosion than anticipated. Moreover, sand bar migration and beach face deposition slowed as the I_A1 trials progressed, but the rate of nearshore erosion continued to increase creating an appreciable trough

between the bar and the beach face (Figure 3.2b). The extent of nearshore erosion limited data collection in the final trials of I_A2 as the local bed elevation eroded out of measuring range for the PSA and ADPV. Condition I_A1 was run after all three erosive conditions (I_E1, I_E2, I_E3) were tested on the 1:25 slope as less change was expected to occur. The results of the profile evolution during I_A2 showed an improved recovery trend compared to the 1:15, but nearshore erosion was still observed. Additionally, sediment was not mobilized on the upper beach due to a lower extent of the upper swash limit.

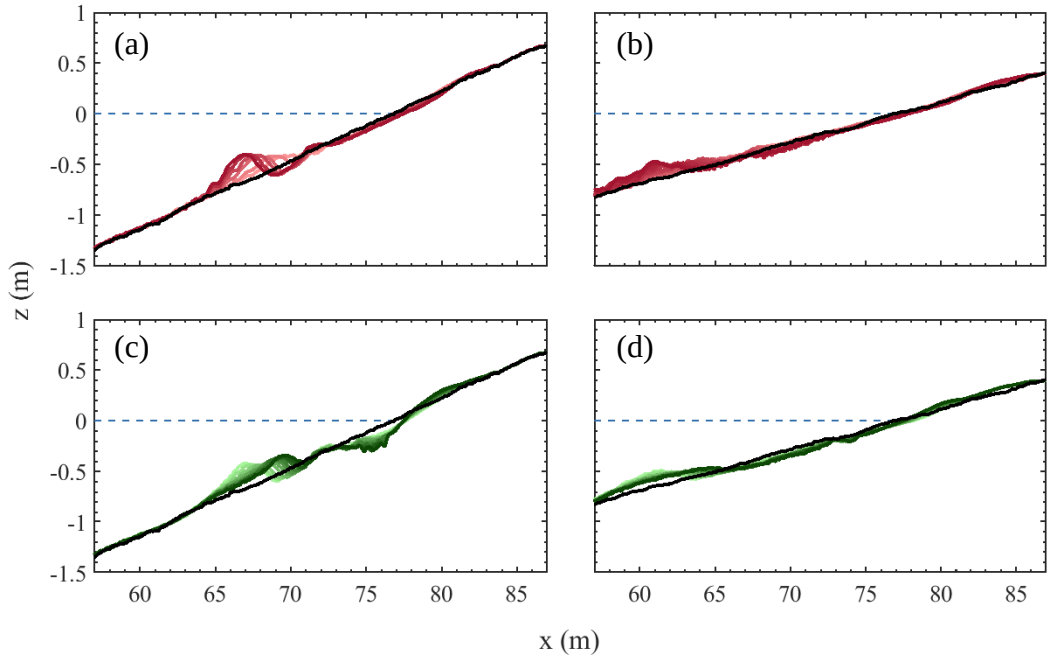

Figure 3.1: Beach profile evolution for the energetic (erosive) irregular conditions on the (a) 1:15 and (b) 1:25 sloped profiles compared with less energetic (accretive) irregular condition on the (c) 1:15 and (d) 1:25 sloped profiles. Profiles were measured after each trail (30 minutes for erosive conditions and 60 minutes for accretive conditions) with the colors becoming darker for each successive profile. The accretive condition (I_A1) in (c) was tested immediately following the I_E1 condition. The accretive condition (I_A1) in (d) was tested after all three erosive conditions (I_E1, I_E2, and I_E3) were tested. The reference profile is represented by the black line. The beach was not reshaped between these trials.

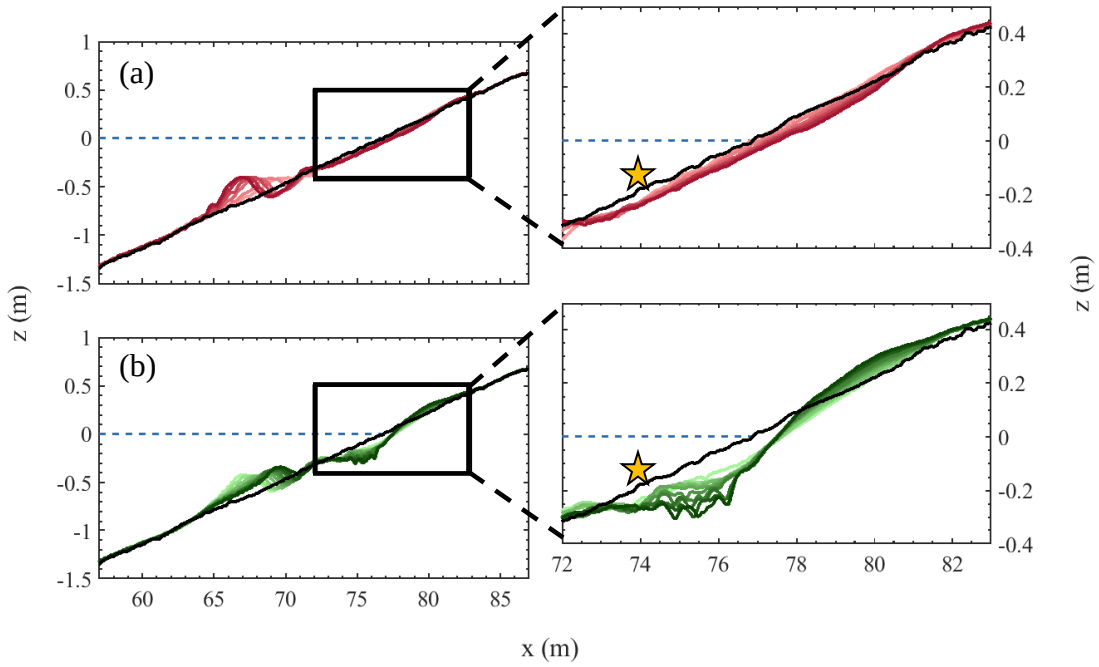

Figure 3.2: Comparison of the (a) I_E1 wave condition and (b) I_A1 wave condition tested on the 1:15 slope with a closer look at the profile response within the inner surf and swash zones. The reference profile is represented by the black line and the yellow star depicts the location of station 1.

Although the bichromatic conditions exhibited similar evolution trends as the irregular waves on the 1:15 slope, a uniform breaking area caused by continual wave similarity created a second bar shoreward of the breaking zone with a trough separating the two bars. The second bar appeared to be inconsequential when examining the repeatability of the flow characteristics (discussed in further detail in section 3.2). Local erosion was also observed in the nearshore which was not experienced during the energetic irregular conditions. The response of the 1:25 slope during the bichromatic conditions showed very weak similarity to the irregular

conditions. Large change was observed both in nearshore erosion and accretion on the beach face. The B_E3_4W_R1 condition presented exceptionally dramatic changes.

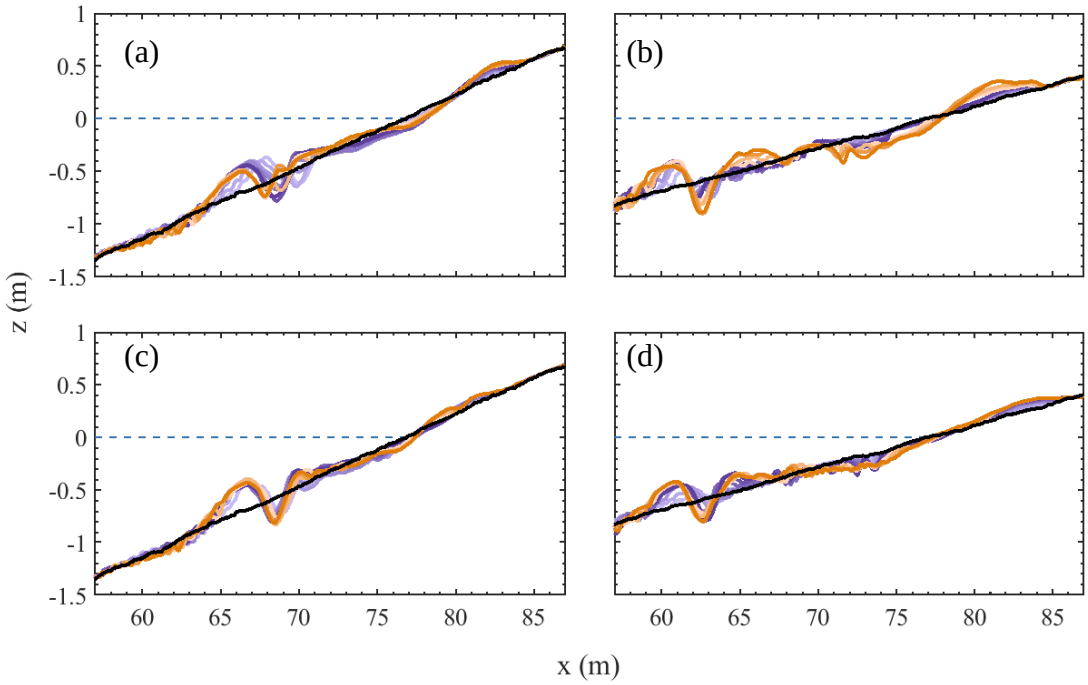

Figure 3.3: Profile evolution comparison of the bichromatic wave groupings and repetition sequences during the two experimental campaigns. The repetition sequence is identified by color; orange is the repetition of a single group (R1) and purple is the alternating repetition of two groups (R2). (a) B_E3_4W_R1 and B_E3_4W_R2 on the 1:15 slope. (b) B_E3_4W_R1 and B_E3_4W_R2 on the 1:25 slope. (c) B_E3_5W_R1 and B_E3_5W_R2 on the 1:15 slope. (d) B_E3_5W_R1 and B_E3_5W_R2 on the 1:25 slope. Colors become darker for each successive trial. The reference profile is represented by the black curve.

3.2 Group Averaging

Group averaging of the various bichromatic wave conditions was conducted to validate the repeatability of the bichromatic forcing and identify trends between the disruptive forces and the bed response. The collected group averages spanned across two groups regardless of repetition sequence to maintain consistency in the analysis. The group pairs were identified using a unique characteristic feature repeated in the wave signal for each condition that was manually selected from the free surface elevation data. The extracted data segment was compared to the full time series for each trial of the wave condition using cross correlation to locate similar occurrences. A squared correlation coefficient of 0.9 was chosen as the cutoff for acceptable similarity. A temporal buffer of twice the group period was used to prevent any overlap by the identified groups. The buffer was not necessary during the two group repetitions; however, the single group repetitions were at risk of having repeat occurrences if the buffer was not used. Condition B_E3_5W_R1 had the longest group period of 19.25 s (38.5 second buffer) allowing for a maximum of 45 realizations in a 30-minute trial. The maximum number of acceptable realizations was set to less than the maximum number possible and realizations collected within less than the corresponding group period of the trial start and termination were discarded to avoid inconsistencies associated with wave maker ramp-up and cool down. The indices for the collected groups were used to extract frames of the Shields parameter, Sleath number, and sheet flow layer thickness time series for comparison (Figure 3.4).

The group averaged values of the Shields parameter exceeded the critical range for sheet flow initiation, θ = 0.5 to 1.0 (Mieras et al., 2017; Nielsen, 1992; Sumer et al., 1996), in all presented conditions. Averaged Sleath numbers also exceeded the critical limit, S = 0.1 (Foster et al., 2006), required for plug flow. Interestingly, there

were many occurrences where these criteria were met, yet the observed bed response was insignificant and in some realizations the bed response was large compared to the response captured in another realization under the same conditions (Figure 3.5). Nevertheless, it was observed that the largest responses are in general alignment with increases in Shields parameter and Sleath number averages. The intermittent spikes in bed response require further analysis that cannot be conducted through the inspection of group averages.

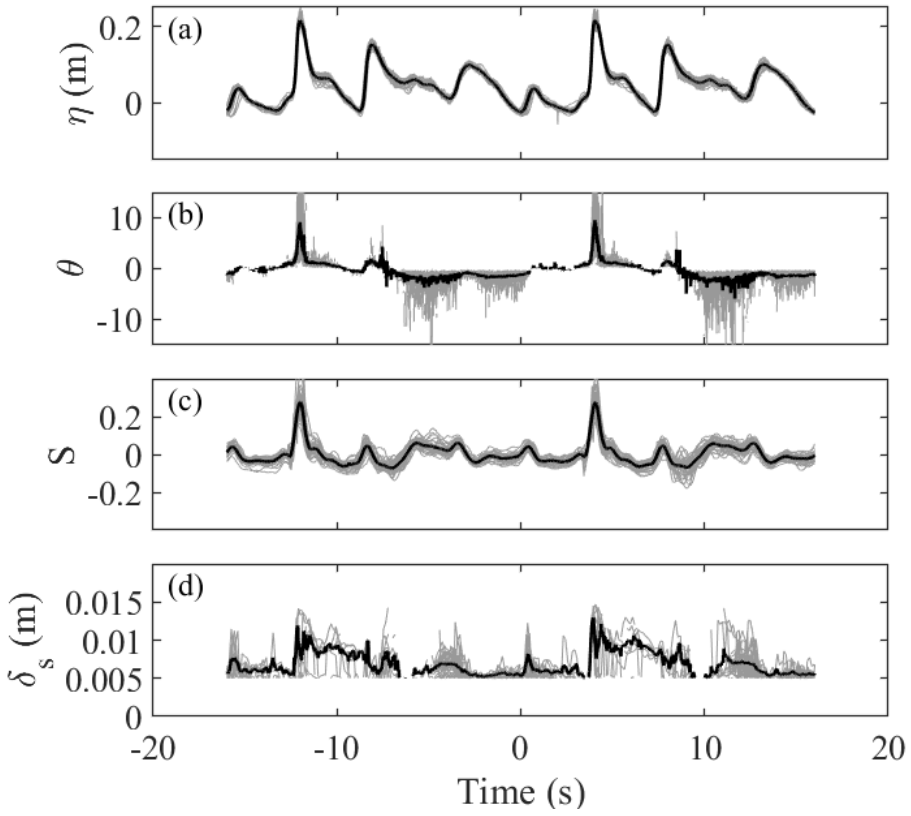

Figure 3.4: Group averages of (a) relative free surface elevation, (b) Shields parameter, (c) Sleath number, and (d) sheet flow layer thickness for the bichromatic condition B_E3_4W_R1 (4 waves per group with a single group repetition) tested on the 1:15 slope. The black line represents the average values, and the gray lines are the individual realizations used in the averaging scheme.

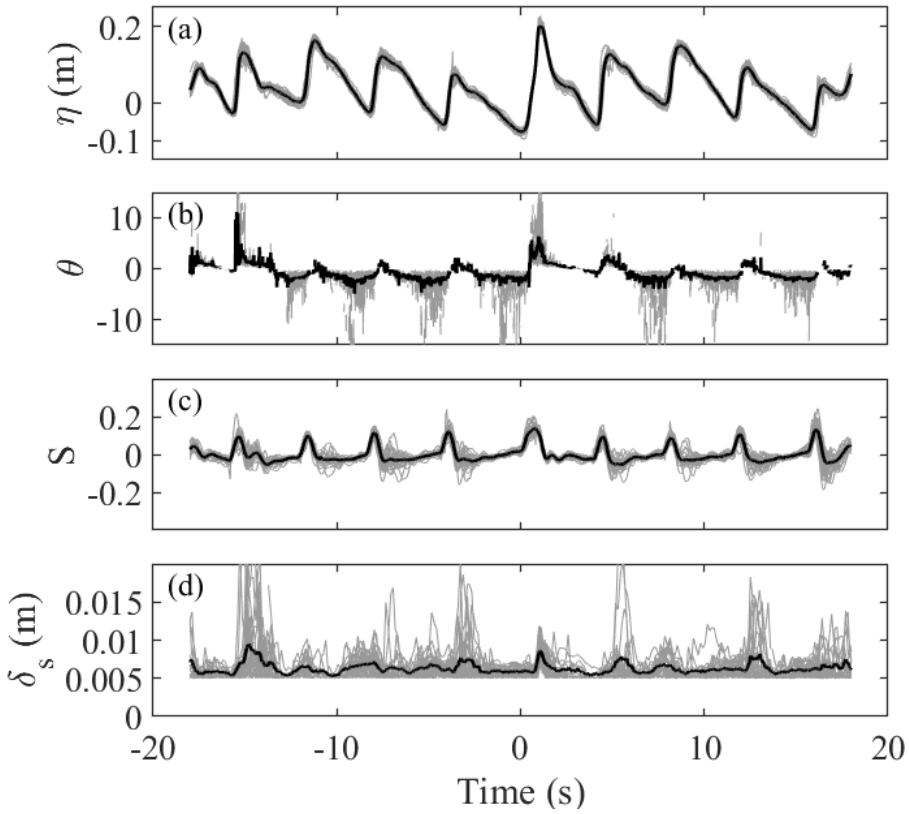

Figure 3.5: Intermittent spikes in bed response are observed in (d). Group averages of (a) relative free surface elevation, (b) Shields parameter, (c) Sleath number, and (d) sheet flow layer thickness for the bichromatic condition B_E3_5W_R2 (4 waves per group with a single group repetition) tested on the 1:15 slope. The black line represents the average values, and the gray lines are the individual realizations used in the averaging scheme

3.3 Bed Response Identification

Sheet flow layer data were inspected to identify occurrences of "large" bed responses. The data were compared against free surface elevation, free stream velocity, Shields parameter, and Sleath number to examine discernible patterns or trends that may be influential in promoting sediment mobilization or bed failure (Figure 3.6). Large bed responses (referred to hereafter as peak bed responses) were identified using a minimum threshold of 0.008 m. A minimum temporal difference

equivalent to the incident wave period, T = 3.5 s, was used to ensure that only one peak bed response per wave could be identified.

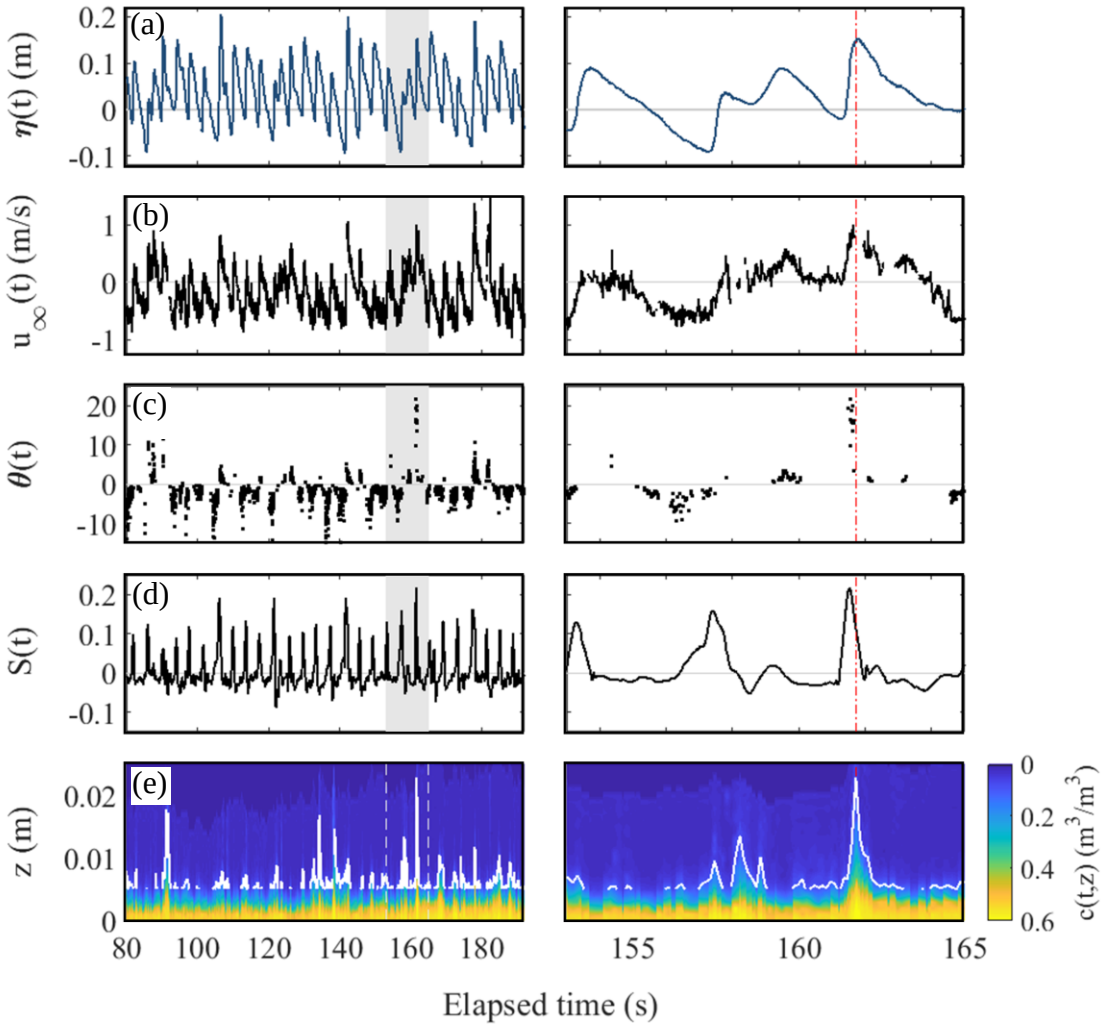

Figure 3.6: Subplot comparison of (a) free surface, (b) free stream velocity, (c) Shields Parameter, (d) Sleath Number, and (e) sheet flow thickness where the white curve is the corrected sheet flow layer thickness. The gray shaded regions in (a) – (d) and the gray vertical dashed lines in (e) represent the data plotted in the panels on the right. The red vertical dashed line references the temporal location of the peak bed response shown in the lower right panel.

Intermittent peak bed response occurrences were often coincident with peaks in Shields parameters and Sleath number within the span of the incident wave period ($\leq \pm$ ½ T_p). Increases in Shields parameter were not always observed, as there were often gaps in the data due to low water levels, turbulent aeration, or weak correlation between the vertical velocity structure and the logarithmic profile of the law of the wall.

3.4 Shields vs Sleath

3.4.1 Time Delayed Response

Inspection of peaks in bed response, identified in Section 3.3, revealed the existence of a phase lag, or time delayed response (commonly referred to as time lags), between the disruptive forces and bed level fluctuations. The iterative process of identifying individual spikes in bed response was expanded to include the isolation and identification of corresponding peaks in Shields parameter and Sleath number occurrences (Figure 3.7). Shields parameter data were smoothed using gaussian averaging on a 0.1 s moving window to reduce signal noise caused by small-scale turbulent fluctuations in the streamwise velocity measurements. Noise reduction in Sleath numbers was previously addressed in the smoothing procedure (discussed in section 2.2.2) used in the difference calculation of the pressure gradients and no additional smoothing was necessary.

Time lags were calculated using the temporal variation between peaks in disruptive forcing and response (Shields-parameter/bed-response and Sleath-number/bed-response) where a negative sign convention was used to denote occurrences of forcing identified prior to the response. Corresponding magnitudes of

bed response, Shields parameter, and Sleath numbers as well as the associated time lags were recorded for each of the bichromatic wave conditions and group sequences tested on both profile slopes. Histograms of the time lags in bed response for both Shields parameters and Sleath numbers were used to analyze the distribution in time lag variation of the two disruptive forces (Figure 3.8). The location of the inner-surf/swash boundary relative to station 1 during the second experimental campaign (1:25 slope) introduced low backwash water levels prior to bore arrival in the five wave bichromatic condition sets (B_E3_5W_R1 and B_E3_5W_R2). The low water levels resulted in insufficient velocity measurements collected to construct definitive distributions of Shields parameter time lags. A comparison of the five wave sets between the two slopes was not available and histograms of these tests are not presented.

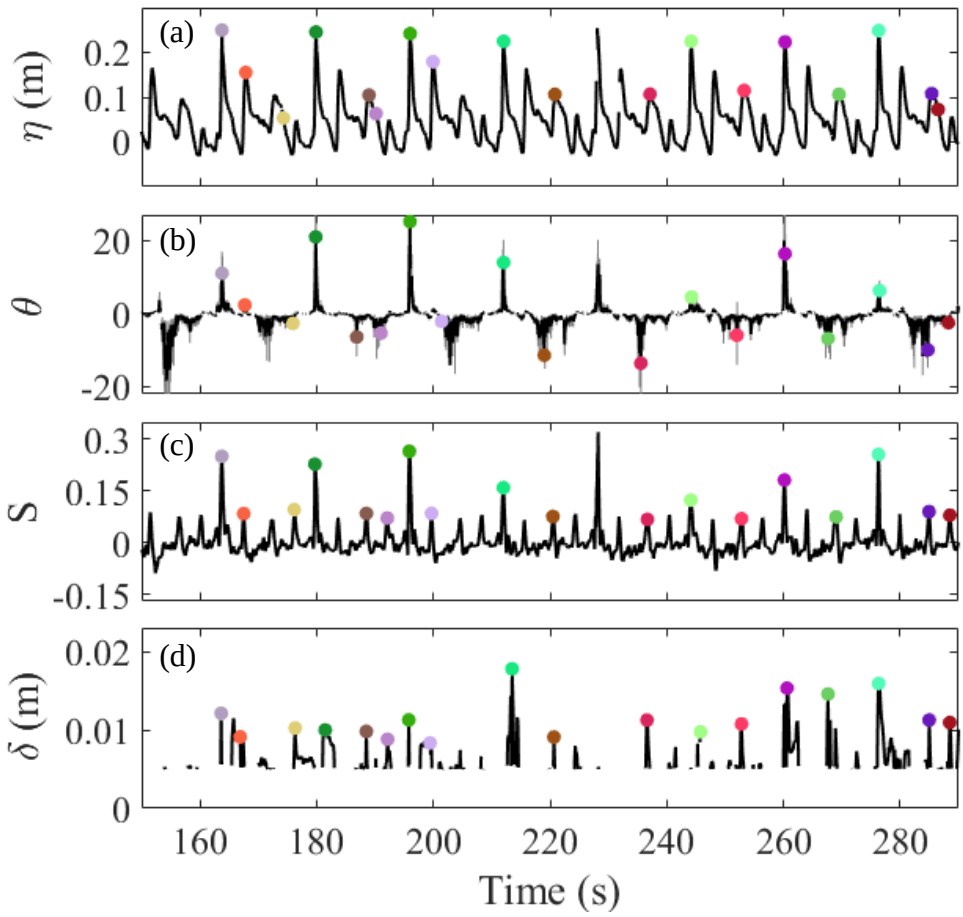

Figure 3.7: Example of peak values of (a) free surface elevation, (b) Shields parameter, and (c) Sleath number corresponding to (d) maximum bed responses exceeding 0.008 m. Corresponding peak values are identified by matching colored circles.

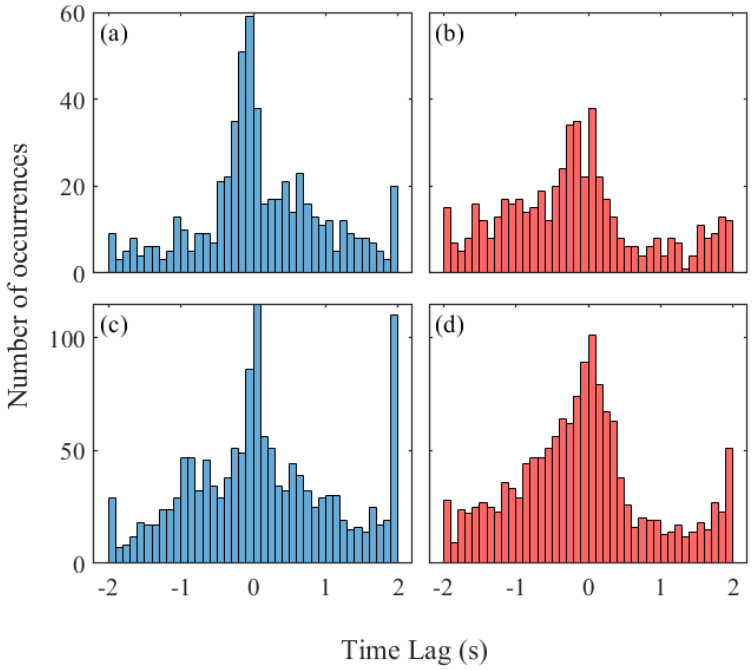

Figure 3.8: Histogram plots depicting the distribution of time lags between (a) Sleath number and bed response and (b) Shields Parameter and bed response for condition B_E3_4W_R1 on the 1:15 slope; Distribution of time lags between (c) Sleath number and bed response and (d) Shields Parameter and bed response for condition B_E3_4W_R2 on the 1:15 slope.

Comparison of the histogram plots between group sequencing exhibit a general agreement in shape similarity of time lag distributions. However, the change in repetition resulted in a positive shift observed in the distributions such that the mean time lag between disruptive forces and bed response may be more accurately described as a time lead between response and forcing. It is important to note that the mean value is influenced by the inclusion of values identified near the extents of the temporal range regardless of the relative importance of the associated Shields parameters and Sleath Numbers.

The time lag distributions were further examined by analyzing the relative importance of the collected peak values as a function of time lag and magnitude of bed response (Figure 3.9). The center of mass of the recorded values, weighted by the corresponding bed response, was calculated to assess the influence of time lag extremities. The distribution of time lags was comparable to the distribution of both Shields and Sleath values. Larger Shields and Sleath values were typically zero-centered with respect to time lag in bed response. Sleath numbers decreased drastically for time lags greater than 0 s, and some large Sleath values were observed with time lags less than -1 s. However, these instances were associated with bed response magnitudes of less than 0.014 m.

Recorded Shields parameters represented a proportionate number of onshore and offshore flow scenarios but larger magnitudes were generally onshore directed which is consistent with findings suggested from previous research (e.g. Butt et al., 2004, 2005; Chardón-Maldonado et al., 2016; Puleo et al., 2014; Torres-Freyermuth et al., 2013). Moreover, large offshore directed Shields values identified as the peak value in the considered time-frame do not necessarily indicate that shear stresses introduced during offshore flow were in fact larger in magnitude than shear stresses introduced during onshore flow as the largest stresses may have been experienced during gaps in velocity measurements.

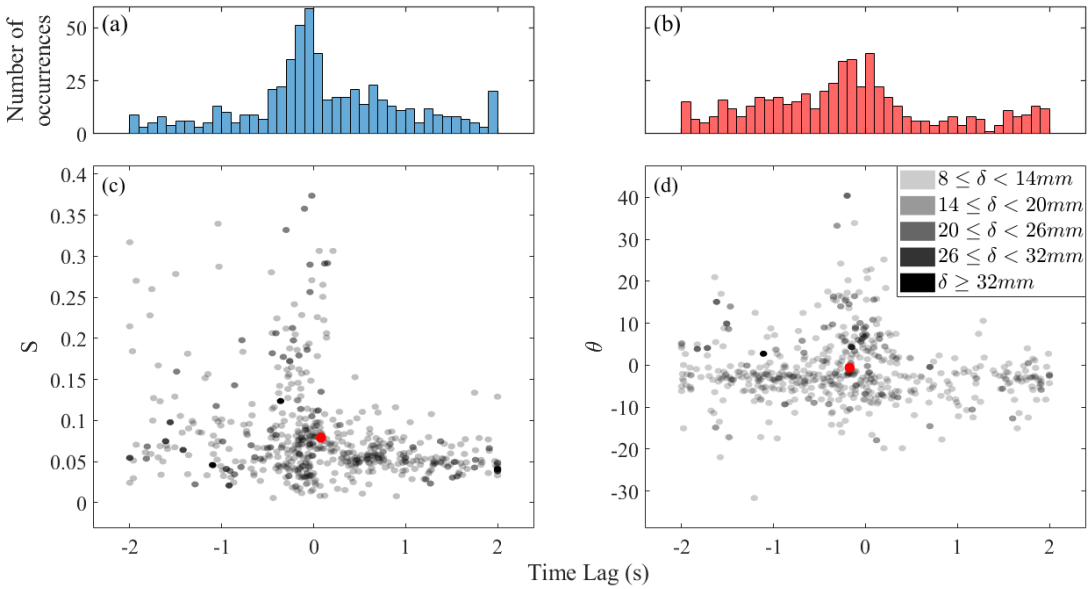

Figure 3.9: Histograms of the time lags between peak bed response and the (a) corresponding peak Sleath number and (b) corresponding peak Shields parameter for condition B_E3_4W_R1 on the 1:15 slope; Compared with (c) peak Sleath number and (d) peak Shields parameter plotted as a function of the time lag and magnitude of the corresponding peak sheet flow thickness. The red dot denotes the center of mass of the plotted values weighted by the magnitude of sheet flow thicknesses.

Sleath number time lags for all test sequences displayed a nearly normal distribution with an average mean time lag of -0.11 s and an average standard deviation of 0.1 s. The average Sleath number and time lag across all tests determined by calculating the bed-response-weighted center of mass was S = 0.13 and Δt = -0.11 s, respectively. Similarly, Shields parameter time lags were also normally distributed in tests on the 1:15 slope, with average mean time lag and standard deviation of 0.14 s and 0.15 s, respectively. However, a more uniform distribution was observed in the B_E3_4W_R2 tests on the 1:25 slope (refer to Figure C.3 in Appendix C). Weighted center mass averages for Shields parameters and time lags were θ = 6.1 and Δt = 0.02

s, respectively. Weighted center of mass time lags for both Shields parameters and Sleath numbers are in good agreement with the statistically determined averages as they only vary by $\leq \pm 0.06$ s. Individual statistics for the four-wave tests are presented in Table 3.1. Comparisons of other bichromatic tests on the 1:25 slope were not definitive, as mentioned previously.

Table 3.1: Shields and Sleath statistics for four-wave Bichromatic conditions

			Time Lag (s)			Value		
	Condition		Mean	Standard Deviation	Center of Mass	Mean	Standard Deviation	Center of Mass
Slope: 1:15								
	B_E3_4W_R1							
		S	0.10	0.88	0.08	0.13	1.01	0.08
		θ	-0.18	0.99	-0.17	5.89	5.27	5.72
	B_E3_4W_R2							
		S	0.13	1.02	0.07	0.12	0.37	0.09
		θ	-0.09	0.95	-0.09	5.26	7.05	4.90
Slope: 1:25								
	B_E3_4W_R1							
		S	-0.37	0.78	-0.31	0.22	0.12	0.17
		θ	0.71	0.83	0.17	20.01	21.47	17.43
	B_E3_4W_R2							
		S	-0.31	0.83	-0.28	0.17	0.08	0.16
		θ	0.13	1.20	0.17	13.75	13.34	12.83

Note: Only absolute magnitudes of Shields Parameter values were considered to remove directional bias.

3.4.2 Influence on Bed Response

Individual comparisons between associated Shields parameters and Sleath numbers could not be made in the analysis of the histograms and scatterplots

formulated on relative dependencies to time lags with bed response. Determination of the governing significance of disruptive forces was investigated by examining the bed response associated with corresponding Shields parameters and Sleath numbers (Figure 3.10). Additionally, the direction of flow at the time of peak bed response was recorded to parameterize the influence of driving forces during uprush and backwash conditions.

Shields and Sleath values associated with bed response magnitudes greater than 0.02 m were generally low and exhibited similar time lags close to zero. A possible explanation may be that the combination of coincident driving forces promotes a rapid critical bed failure with an increase in volume of mobilized sediment. However, definitive conclusions cannot be formulated as these occurrences were infrequent and it is likely that additional hydrodynamic mechanisms not considered in this research may have contributed to an enhanced bed response.

Although a slight trend in increasing Shields and Sleath values as the magnitude in bed response increased was observed for bed response values less than 0.018 m (Figure 3.11), the trend was inconsistent and did not continue for bed response peaks greater than 0.018 m. The key result depicted in this analysis was not the poor correlation between increasing forcing and response, but rather that Sleath magnitudes with positive time lags were subcritical (< 0.1) and typically associated with peaks in bed response experienced during offshore directed flows (Figure 3.11a). Thus, revealing that large responses in bed level change were not generated during uprush or backwash exclusively. In fact, large peaks in bed response identified during backwash were similar in magnitude to those identified during uprush. Furthermore, small Sleath numbers identified ensuing peak responses in bed level fluctuations

indicate a possible transition in governing disruptive forces dependent on the phase of the flow cycle.

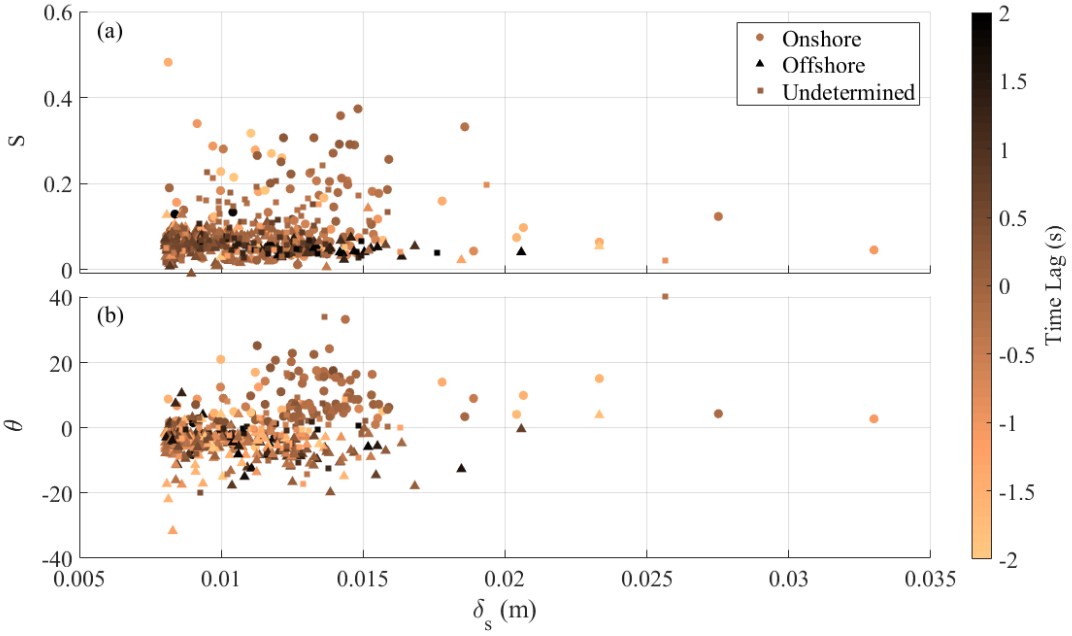

Figure 3.10: (a) Peak Sleath numbers and (b) peak Shield parameters plotted as a function of peak bed response for condition B_E3_4W_R1 tested on the 1:15 sloped profile. The change in color represents the time lag between the forcing and response. The direction of the flow during peak bed response is illustrated by the shape of the symbol where circles indicate onshore, triangles indicate offshore, and squares indicate an undetermined flow direction.

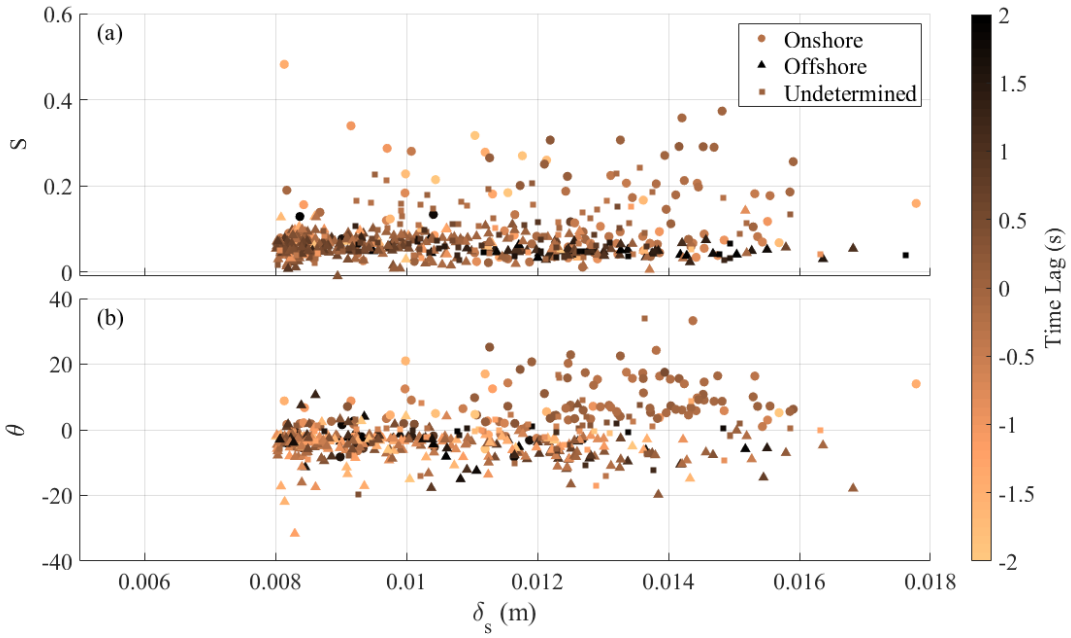

Figure 3.11: Zoomed in depiction of Figure 3.10 for values of peak bed response less than 0.018 m. Plot characteristics are consistent with the description provided for Figure 3.10.

3.5 Irregular Waves

Similar analytic procedures to those discussed in section 3.4 were applied to investigate the role of Shields parameters and Sleath numbers as driving forces under irregular wave conditions. Condition I_E3 was chosen for comparison because it consisted of equal incident wave energy and wave characteristics (H_s and T_p) as the Bichromatic wave conditions.

The results showed that Sleath values maintained a normal distribution comparable to the distributions presented in the bichromatic wave conditions, but Shields values appeared to have a more uniform distribution (Figure 3.12a-b). Typically, Sleath numbers with small time lags preceded large bed response incidents, indicating a possible correlation in bed response magnitude to the proximity in phase

of disruptive forcing (Figure 3.12c). Conversely, Shields values exhibited a poor correlation between time lags and large responses measured in the bed (Figure 3.12d). Though, Shields values did present a different noticeable trend. Shields Parameters identified prior to the peak bed response were generally offshore directed and those identified after peak bed response were primarily onshore directed. Shields values were in the same range of magnitudes for onshore and offshore flows indicating a similarity in shear stresses experienced during uprush and backwash. This is consistent with the results observed in the bichromatic wave conditions.

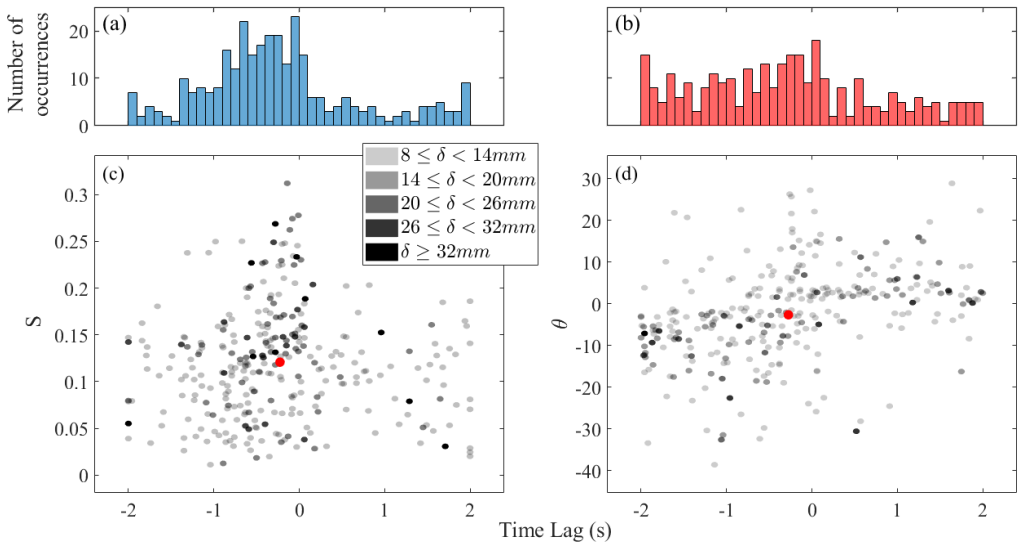

Figure 3.12: Histograms of the time lags between peak bed response and the (a) corresponding peak Sleath number and (b) corresponding peak Shields parameter for condition I_E3 on the 1:15 profile; Compared with (c) peak Sleath number and (d) peak Shields parameter plotted as a function of the time lag and magnitude of the corresponding peak sheet flow thickness. The red dot denotes the center of mass of the plotted values weighted by the magnitude of sheet flow thicknesses.

Bed response examined as a function of either Shields parameter or Sleath number displayed large variability and no discernible relationship was identified Figure 3.13). Flow directions during peak bed response were undetermined in many instances due to discontinuities in velocity measurements and it is important to consider the possibility that large shear stresses may have gone unrecorded.

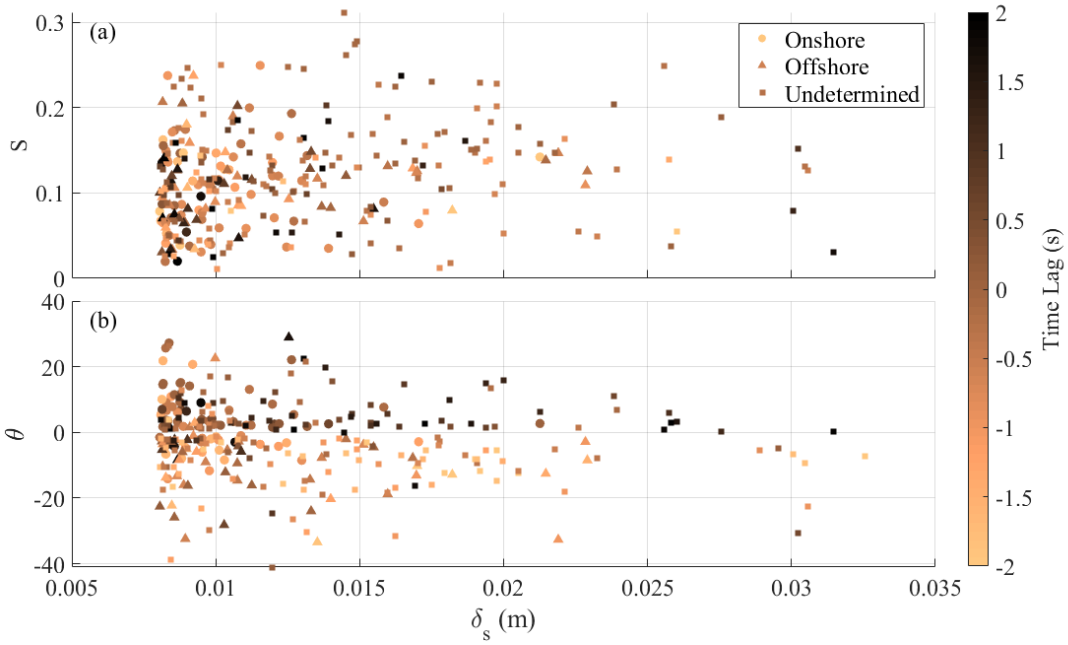

Figure 3.13: (a) Peak Sleath numbers and (b) peak Shield parameters plotted as a function of peak bed response for condition I_E3 tested on the 1:25 sloped profile. The change in color represents the time lag between the forcing and response. The direction of the flow during peak bed response is illustrated by the shape of the symbol where circles indicate onshore, triangles indicate offshore, and squares indicate an undetermined flow direction.

Statistical values for I_E3, presented in Table 3.2, were in good agreement with the results found in the bichromatic tests and fell with the ranges presented in Table 3.1. The results were not consistent with any particular bichromatic condition, as expected due to the stochastic nature of the irregular wave field.

Table 3.2: Shields and Sleath statistics for irregular wave conditions

		Time Lag (s)			Value		
Condition		Mean	Standard Deviation	Center of Mass	Mean	Standard Deviation	Center of Mass
I_E3							
	S	-0.23	0.91	-0.23	0.12	0.07	0.12
	θ	-0.28	1.05	-0.28	8.88	8.38	8.39

Note: Only absolute magnitudes of Shields Parameter values were considered to remove directional bias.

Chapter 4

DISCUSSION

The effects of the combined influence of bed shear stress and horizontal pressure gradients on peak bed response, as well as the correlation between these forcing and response mechanisms, within the swash and inner surf zone was assessed. The analysis was complicated by data collection limitations, variability in phase relationships, and nonlinearities associated with flow skewness and asymmetry. Regardless, several trends were observed and used to assess the relationship, and relative significance, between shear stress and horizontal pressure gradients on bed response.

Large pressure gradients and shear stresses were recorded during moments of dramatic bed level change identifying a strong relationship between the two forces as drivers of sediment mobility. Yet, maximum shear stresses and horizontal pressure gradients (nondimensionalized as the Shields parameter and Sleath number, respectively; previously discussed in section 1.2.2) were not always observed simultaneously, suggesting a fluctuating influential significance between both forces. Although occurrences of large Shields and/or Sleath values coincident with relatively large responses in the bed were observed, these occurrences were not consistent, and a direct relationship could not be formulated. In fact, even occasional trends in growth between the forcing components and bed response appeared to break down at "larger" recorded bed responses (typically $\delta > \sim 0.02$ m). Inner surf and swash zone hydrodynamics are complex and there are many influential mechanisms that

contribute to sediment mobilization. It would be imprudent to ignore the likelihood of additional factors augmenting the bed response. For example, wave induced turbulent eddies that reach bed level can suspend sediments and create momentary spikes in sheet flow layer thickness. Associated shear stresses and horizontal pressure gradients may be small under these conditions and sediment suspension is generated by upward directed flow rotation. Other mechanisms such infiltration-exfiltration, migration of temporary small-scale bed forms when flows do not meet sheet flow criterion, etc. that are not covered in the scope of this research certainly exist as well.

Determination of the governing relationship between Shields parameter and Sleath number was limited to their associated time lags with bed response due to the weak correlation between increasing bed response and increasing magnitude of disruptive forces previously mentioned. However, the phase of individual forcing components in relation to bed response is an important factor in distinguishing their respective influential significance on sediment mobilization (e.g. Calantoni & Puleo, 2006) as well as the net sediment transport for fine sediments (e.g. Rafati et al., 2020; Ribberink & Al-Salem, 1995; van der A et al., 2010). Phase lags are particularly influential on fine sediments (≤ 0.25 mm) under short-period asymmetric oscillatory flows (Dohmen-Janssen et al., 2002; Ruessink et al., 2009), similar to the conditions studied in this research.

Average Shields and Sleath time lags in both the irregular and bichromatic wave conditions were smaller than the mode of the distribution. The average time lag between bed response and Shields parameters was 0.14 s and was -0.11 s for Sleath numbers. It is unlikely that maximum Shields parameters would be observed after the peak in bed response, and an inspection of the plots in Appendix C would corroborate

the unlikeliness of this. Averaged time lags, weighted by the observed response of the bed, presented similar results to the statistical averages with a variation of $\leq \pm 0.06$ s. It is worth noting that values recorded near the bounds of the considered window also contained large bed response measurements which introduces a bias in the center of mass calculation. The calculation of the distributive mean and center of mass was skewed by the inclusion of Sleath and Shields values recorded near the extents of the considered temporal frame, centered about the identified peak bed response. However, the distance between propagating bores was not constant because oscillatory flows at or near the inner surf and swash zone boundary are not necessarily periodic due the dominant influence of infragravity waves (Puleo et al., 2000). This was frequently exhibited by faster moving successive bores converging and overtaking the bore preceding them (also referred to as bore capture). It is likely that pressure gradients and shear stresses associated with other nearby waves were introduced to the sampling frame due to fluctuations in flow phase duration. Shields parameters and Sleath numbers identified beyond the range of influence could be reduced by using a more refined temporal range determined for each condition.

Although shear stresses were shown to be influential during both onshore and offshore flows, onshore directed Shields values were generally larger in magnitude during the bichromatic wave conditions. Large onshore directed shear stresses were closer in phase to the bed response on the 1:15 sloped profile and this pattern was much more well defined during the single repetition sequences. Alternatively, Shields values recorded on the 1:25 sloped profile appeared to demonstrate a loosely defined linear relationship with the phase of bed response such that strong offshore shear stresses were recorded before the response was indicated in the bed and progressively

decreased as the time lag decreased. Shields values then began to increase in onshore magnitude as the corresponding time lags to bed response increased. Anecdotally, this is believed to be caused by the drawn-out swash duration and more gradual flow reversal associated with the dissipative slope. Again, it is emphasized that the observations of large Shields values in phase with the bed response cannot be extensively determined due to gaps in velocity measurements typically located near the leading edge of the propagating wave. The accuracy of the trend observed on the 1:25 slope should be regarded with apprehension due to more prevalent discontinuities introduced by lower water levels at the measuring location during the second experimental campaign.

The apex of the distribution curve representing the time lags between bed response and peak Shields values was generally centered around zero seconds and denoted a strong phase correlation for shear stress and bed response. Larger variance shown in the time lag distributions for the Shields parameter indicates many occurrences of shear stress being potentially less influential than pressure gradients on maximum bed level changes in the measured location. Conventionally, when multiple momentary forces are applied to a rigid object, the forces that are at a greater temporal distance from the reaction of the object are considered to have less effective impact on its response. The result of the variance in Shields/response time lags as well as the transition of directional influence in shear stresses indicate the governing effects of the spatial variability of the boundary between the inner surf and swash zones.

Overall, critical Sleath numbers (> 0.1) were compellingly observed prior to the response of the bed while subcritical values represented a much broader assortment of time lags that spanned the width of the relative time window. Shorter

group periods in the bichromatic tests typically exhibited smaller time lags associated with large bed response peaks recorded after the peak in Sleath number, consistent with the results of Calantoni & Puleo, (2006). Instabilities in the bed associated with flow reversal are common and the rapid introduction of additional disruptive forcing or rapid change in forcing by pressure gradients produces a more immediate response in sediment mobilization.

Naturally, pressure gradients are proportional to the slope of free surface elevation and are therefore limited by the maximum steepness of the surface before wave breaking or collapse occurs. Maximum observed Sleath values were approximately 0.4. However, no discernible correlation to the overall magnitude of bed responses corresponding to Sleath numbers above the critical threshold could be concluded as a large variability in Sleath numbers was present despite similar corresponding bed response magnitudes and consistent time lags. Surely, it is possible that the combined influence of horizontal pressure gradients and shear stresses may contribute to an enhanced bed response such that the effective critical threshold of each forcing mechanism is reduced by the contributed influence of the other. Likewise, it is also possible that sediment already mobilized in the sheet flow during the backwash can converge with the bed failure initiated by critical pressure gradients and promote dramatic momentary bed level changes.

Net sediment transport rates may be similar between bichromatic and natural waves, but localized erosion and accretion were observed to be much greater under bichromatic conditions. Hydrodynamic forcing of the two wave types displayed similar trends, but recorded Shields values represented a more uniform distribution. This is likely due to the fluctuating inner surf and swash zone boundary. A strong

spatial dependence was shown to affect the influence of shear stress and even slight changes in the location of bore collapse and offshore extent of backwash revealed a shift in the relative influence of shear stresses and horizontal pressure gradients. Overall, Shields parameter magnitudes during the irregular waves showed little to no exceedance between uprush and backwash contradicting the results found in bichromatic conditions with longer group periods (the single repetition groups). Bichromatic conditions with small group periods (the alternating group repetitions) showed similar magnitudes of onshore and offshore Shields parameters much like the irregular wave tests. This is believed to be a result of longer uprush and backwash durations caused by the influence of intermittent harmonic resonance between the infragravity and incident waves.

The highly precise repeatability of bichromatic waves promotes drastic changes in areas that continuously experience constant forcing such as the breaking zone in the surf zone and bore collapse in the nearshore. Multiple tests were affected by these dramatic changes as erosion near the shoreline was not anticipated to the extent that was experienced. The predictability of locations is important because, if predicted accurately, it allows for instrumentation to be deployed in areas of rapid change without the need to collect spatially robust datasets. Erosive and accretive areas will migrate eventually though due to evolution of the bed geometry, but these migrations are also predictable under controlled conditions.

Chapter 5

CONCLUSIONS

Large-scale laboratory observations of bed mobilization within the swash and inner surf zones as well as quantification of corresponding local bed shear stresses and horizontal pressure gradients have been presented. Shear stresses were calculated using the log-law with data collected from a high-resolution profiling velocimeter and parameterized using the nondimensional Shields parameter. Horizontal pressure gradients were calculated using a novel pressure sensor array and parameterized using the dimensional Sleath number. The observations were collected under bichromatic and irregular wave conditions within close proximity to the inner surf and swash zone boundary.

The current state of this research provides insight into the forces that govern maximum bed response. However, isolating the onset of sediment mobilization is challenging under continuous oscillatory flow where shallow water depths are present. Long period monochromatic waves or solitary waves could be tested to further investigate the driving forces of incipient motion in the inner surf and swash zones. These types of waves offer enough settling time for the sediment to return to rest prior to experiencing repeated hydrodynamic disruptive forces. The additional time between waves would also allow for proper scaling of the relative timeframe used to locate maximum values of Shields parameters and Sleath numbers.

Although the rapidly changing hydrodynamics restricted the analysis of incipient motion, the diverse set of hydrodynamic conditions offered valuable

evidence to the fluctuating roles of horizontal pressure gradients and shear stresses in relation to the phase of the flow. Large horizontal pressure gradients generated by the leading edge of the asymmetric waves were shown to exceed the critical threshold to promote plug flow conditions and resulted in large spikes in bed level elevation during flow reversal. Offshore directed shear stresses caused by the backwash prior to flow reversal are believed to enhance the signal of the bed level spikes through the contribution of additional disruptive forcing due to the convergence of onshore and offshore flows. Horizontal pressure gradients are considered the governing disruptive force in the inner surf zone when critical Sleath values are met and are generally close in phase with the bed response. However, occurrences of bed level response during backwash flows exceeding the prior or subsequent responses in onshore flows illustrate the dominance of shear stress in the swash zone where pressure gradients have reduced significantly after bore collapse.

REFERENCES

Aagaard, T., & Hughes, M. G. (2006). Sediment suspension and turbulence in the swash zone of dissipative beaches. *Marine Geology*, *228*(1–4), 117–135. https://doi.org/10.1016/j.margeo.2006.01.003

Alsina, J. M., & Cáceres, I. (2011). Sediment suspension events in the inner surf and swash zone. Measurements in large-scale and high-energy wave conditions. *Coastal Engineering*, *58*(8), 657–670. https://doi.org/10.1016/j.coastaleng.2011.03.002

Alsina, J. M., van der Zanden, J., Cáceres, I., & Ribberink, J. S. (2018). The influence of wave groups and wave-swash interactions on sediment transport and bed evolution in the swash zone. *Coastal Engineering*, *140*, 23–42. https://doi.org/10.1016/j.coastaleng.2018.06.005

Anderson, D., Cox, D., Mieras, R., Puleo, J. A., & Hsu, T.-J. (2017). Observations of wave-induced pore pressure gradients and bed level response on a surf zone sandbar: wave-induced pore pressure gradients. *Journal of Geophysical Research: Oceans*, *122*(6), 5169–5193. https://doi.org/10.1002/2016JC012557

Archie, G. E. (1942). The Electrical Resistivity Log as an Aid in Determining Some Reservoir Characteristics. *Transactions of the AIME*, *146*(01), 54–62. https://doi.org/10.2118/942054-G

Astruc, D., Cazin, S., Cid, E., Eiff, O., Lacaze, L., Robin, P., Toublanc, F., & Cáceres, I. (2012). A stereoscopic method for rapid monitoring of the spatio-temporal evolution of the sand-bed elevation in the swash zone. *Coastal Engineering*, *60*, 11–20. https://doi.org/10.1016/j.coastaleng.2011.08.007

Bagnold, R. A. (1956). The Flow of Cohesionless Grains in Fluids. *Philosophical Transactions of the Royal Society of London. Series A, Mathematical and Physical Sciences*, *249*(964), 235–297.

Bagnold, R. A. (1966). *An Approach to the Sediment Transport Problem from General Physics*. U.S. Government Printing Office.

Bailard, J. A. (1981). An energetics total load sediment transport model for a plane sloping beach. *Journal of Geophysical Research*, *86*(C11), 10938. https://doi.org/10.1029/JC086iC11p10938

Baldock, T. E. (2012). Discussion of "Laboratory investigation of pressure gradients induced by plunging breakers", by Pedrozo-Acuña et al. *Coastal Engineering*, *66*, 1–2. https://doi.org/10.1016/j.coastaleng.2012.03.008

Baldock, T. E., Alsina, J. A., Caceres, I., Vicinanza, D., Contestabile, P., Power, H., & Sanchez-Arcilla, A. (2011). Large-scale experiments on beach profile evolution and surf and swash zone sediment transport induced by long waves, wave groups and random waves. *Coastal Engineering*, *58*(2), 214–227. https://doi.org/10.1016/j.coastaleng.2010.10.006

Baldock, T. E., & Hughes, M. G. (2006). Field observations of instantaneous water slopes and horizontal pressure gradients in the swash-zone. *Continental Shelf Research*, *26*(5), 574–588. https://doi.org/10.1016/j.csr.2006.02.003

Baldock, T. E., Huntley, D. A., Bird, P. A. D., O'Hare, T., & Bullock, G. N. (2000). Breakpoint generated surf beat induced by bichromatic wave groups. *Coastal Engineering*, *39*(2–4), 213–242. https://doi.org/10.1016/S0378-3839(99)00061-7

Battjes, J. A. (1974). Surf similarity. *Coastal Engineering Proceedings*, *1*(14), 26. https://doi.org/10.9753/icce.v14.26

Bauer, B. O., Davidson-Arnott, R. G. D., Hesp, P. A., Namikas, S. L., Ollerhead, J., & Walker, I. J. (2009). Aeolian sediment transport on a beach: Surface moisture, wind fetch, and mean transport. *Geomorphology*, *105*(1–2), 106–116. https://doi.org/10.1016/j.geomorph.2008.02.016

Beach, R. A., Sternberg, R. W., & Johnson, R. (1992). A fiber optic sensor for monitoring suspended sediment. *Marine Geology*, *103*(1–3), 513–520. https://doi.org/10.1016/0025-3227(92)90036-H

Blenkinsopp, C. E., Turner, I. L., Masselink, G., & Russell, P. E. (2011). Swash zone sediment fluxes: Field observations. *Coastal Engineering*, *58*(1), 28–44. https://doi.org/10.1016/j.coastaleng.2010.08.002

Bowen, A. J. (1980). Simple models of nearshore sedimentation: Beach profiles and longshore bars. *The Coastline of Canada*.

Butt, T., Russell, P., Puleo, J., & Masselink, G. (2005). The Application of Bagnold-Type Sediment Transport Models in the Swash Zone. *Journal of Coastal Research, 215*, 887–895. https://doi.org/10.2112/04-0210.1

Butt, T., Russell, P., Puleo, J., Miles, J., & Masselink, G. (2004). The influence of bore turbulence on sediment transport in the swash and inner surf zones. *Continental Shelf Research*, *24*(7–8), 757–771. https://doi.org/10.1016/j.csr.2004.02.002

Butt, T., Tinker, J., Masselink, G., O'Hare, T., & Russell, P. (2009). Field Observations of Sediment Fluxes in the Inner-Surf and Swash Zones. *Journal of Coastal Research, 254*, 991–1001. https://doi.org/10.2112/08-1044.1

Cáceres, I., & Alsina, J. M. (2012). A detailed, event-by-event analysis of suspended sediment concentration in the swash zone. *Continental Shelf Research*, *41*, 61–76. https://doi.org/10.1016/j.csr.2012.04.004

Calantoni, J., & Puleo, J. A. (2006). Role of pressure gradients in sheet flow of coarse sediments under sawtooth waves. *Journal of Geophysical Research, 111*(C1), C01010. https://doi.org/10.1029/2005JC002875

Chardón-Maldonado, P., Pintado-Patiño, J. C., & Puleo, J. A. (2016). Advances in swash-zone research: Small-scale hydrodynamic and sediment transport processes. *Coastal Engineering*, *115*, 8–25. https://doi.org/10.1016/j.coastaleng.2015.10.008

Crowell, M., Edelman, S., Coulton, K., & McAfee, S. (2007). How Many People Live in Coastal Areas?1. *Journal of Coastal Research, 23*(5). https://doi.org/10.2112/07A-0017.1

Dean, R. G. (Robert G., 1930-2015., & Dalrymple, R. A. 1945-. (2002). *Coastal processes: With engineering applications* (Vol. 1–1 online resource (x, 475 pages) : illustrations, maps). Cambridge University Press. http://site.ebrary.com/id/10014609

Dohmen-Janssen, C. M., Kroekenstoel, D. F., Hassan, W. N., & Ribberink, J. S. (2002). Phase lags in oscillatory sheet flow: Experiments and bed load modelling. *Coastal Engineering*, *46*(1), 61–87. https://doi.org/10.1016/S0378-3839(02)00056-X

Downing, J. P., & Beach, R. A. (1989). Laboratory apparatus for calibrating optical suspended solids sensors. *Marine Geology*, *86*(2), 243–249. https://doi.org/10.1016/0025-3227(89)90053-4

Drake, T. G., & Calantoni, J. (2001). Discrete particle model for sheet flow sediment transport in the nearshore. *Journal of Geophysical Research: Oceans*, *106*(C9), 19859–19868. https://doi.org/10.1029/2000JC000611

Elfrink, B., & Baldock, T. (2002). Hydrodynamics and sediment transport in the swash zone: A review and perspectives. *Coastal Engineering*, *45*(3–4), 149–167. https://doi.org/10.1016/S0378-3839(02)00032-7

Foster, D. L., Bowen, A. J., Holman, R. A., & Natoo, P. (2006). Field evidence of pressure gradient induced incipient motion. *Journal of Geophysical Research*, *111*(C5), C05004–C05011.

Frank, D., Foster, D., Sou, I. M., & Calantoni, J. (2015). Incipient motion of surf zone sediments: Incipient motion of surf zone sediments. *Journal of Geophysical Research: Oceans*, *120*(8), 5710–5734. https://doi.org/10.1002/2014JC010424

Fredsøe, J., & Deigaard, R. (1992). *Mechanics of Coastal Sediment Transport* (Vol. 3). WORLD SCIENTIFIC. https://doi.org/10.1142/1546

Gallagher, E. L., Elgar, S., & Guza, R. T. (1998). Observations of sand bar evolution on a natural beach. *Journal of Geophysical Research: Oceans*, *103*(C2), 3203–3215. https://doi.org/10.1029/97JC02765

Guard, P. A., & Baldock, T. E. (2007). The influence of seaward boundary conditions on swash zone hydrodynamics. *Coastal Engineering*, *54*(4), 321–331. https://doi.org/10.1016/j.coastaleng.2006.10.004

Hoefel, F. (2003). Wave-Induced Sediment Transport and Sandbar Migration. *Science*, *299*(5614), 1885–1887. https://doi.org/10.1126/science.1081448

Horikawa, K., Watanabe, A., & Katori, S. (1982). Sediment transport under sheet-flow condition. *Coastal Engineering Proceedings*, *1*(18), 82. https://doi.org/10.9753/icce.v18.82

Horn, D. P., & Mason, T. (1994). Swash zone sediment transport modes. *Marine Geology*, *120*(3–4), 309–325. https://doi.org/10.1016/0025-3227(94)90064-7

Houser, C., & Greenwood, B. (2005). Hydrodynamics and sediment transport within the inner surf zone of a lacustrine multiple-barred nearshore. *Marine Geology*, *218*(1–4), 37–63. https://doi.org/10.1016/j.margeo.2005.02.029

Hsu, T.-J., & Hanes, D. M. (2004). Effects of wave shape on sheet flow sediment transport. *Journal of Geophysical Research*, *109*(C5), C05025. https://doi.org/10.1029/2003JC002075

Hughes, M. G., Aagaard, T., Baldock, T. E., & Power, H. E. (2014). Spectral signatures for swash on reflective, intermediate and dissipative beaches. *Marine Geology*, *355*, 88–97. https://doi.org/10.1016/j.margeo.2014.05.015

Hughes, M. G., Masselink, G., & Brander, R. W. (1997). Flow velocity and sediment transport in the swash zone of a steep beach. *Marine Geology*, *138*(1–2), 91–103. https://doi.org/10.1016/S0025-3227(97)00014-5

Jackson, N. L., Masselink, G., & Nordstrom, K. F. (2004). The role of bore collapse and local shear stresses on the spatial distribution of sediment load in the uprush of an intermediate-state beach. *Marine Geology*, *203*(1–2), 109–118. https://doi.org/10.1016/S0025-3227(03)00328-1

Janssen, T. T. (2003). Long waves induced by short-wave groups over a sloping bottom. *Journal of Geophysical Research*, *108*(C8), 3252. https://doi.org/10.1029/2002JC001515

Kraus, N. C., Larson, M., & Kriebel, D. L. (1991). *Evaluation of beach erosion and accretion predictors*. Amer. Society of Civil Engineers.

Lanckriet, T., Puleo, J. A., Masselink, G., Turner, I. L., Conley, D., Blenkinsopp, C., & Russell, P. (2014). Comprehensive Field Study of Swash-Zone Processes. II: Sheet Flow Sediment Concentrations during Quasi-Steady Backwash. *Journal of Waterway, Port, Coastal, and Ocean Engineering*, *140*(1), 29–42. https://doi.org/10.1061/(ASCE)WW.1943-5460.0000209

Lanckriet, T., Puleo, J. A., & Waite, N. (2013). A Conductivity Concentration Profiler for Sheet Flow Sediment Transport. *IEEE Journal of Oceanic Engineering*, *38*(1), 55–70. https://doi.org/10.1109/JOE.2012.2222791

Madsen, O. S. (1974). Stability of a sand bed under breaking waves. *Coastal Engineering Proceedings*, *1*(14), 45. https://doi.org/10.9753/icce.v14.45

Masselink, G., Evans, D., Hughes, M. G., & Russell, P. (2005). Suspended sediment transport in the swash zone of a dissipative beach. *Marine Geology*, *216*(3), 169–189. https://doi.org/10.1016/j.margeo.2005.02.017

Masselink, G., & Hughes, M. (1998). Field investigation of sediment transport in the swash zone. *Continental Shelf Research*, *18*(10), 1179–1199. https://doi.org/10.1016/S0278-4343(98)00027-2

Masselink, G., & Puleo, J. A. (2006). Swash-zone morphodynamics. *Continental Shelf Research*, *26*(5), 661–680. https://doi.org/10.1016/j.csr.2006.01.015

Masselink, G., Ruju, A., Conley, D., Turner, I., Ruessink, G., Matias, A., Thompson, C., Castelle, B., Puleo, J., Citerone, V., & Wolters, G. (2016). Large-scale Barrier Dynamics Experiment II (BARDEX II): Experimental design, instrumentation, test program, and data set. *Coastal Engineering*, *113*, 3–18. https://doi.org/10.1016/j.coastaleng.2015.07.009

Masselink, G., & Russell, P. (2006). Flow velocities, sediment transport and morphological change in the swash zone of two contrasting beaches. *Marine Geology*, *227*(3–4), 227–240. https://doi.org/10.1016/j.margeo.2005.11.005

Meyer-Peter, E., & Müller, R. (1948). Formulas for Bed-Load transport. *IAHSR 2nd Meeting, Stockholm, Appendix 2*. https://repository.tudelft.nl/islandora/object/uuid%3A4fda9b61-be28-4703-ab06-43cdc2a21bd7

Middleton, G. V., & Southard, J. B. (John B. (1984). *Mechanics of sediment movement* (Second edition.). Society of Economic Paleontologists and Mineralogists.

Mieras, R. S., Puleo, J. A., Anderson, D., Cox, D. T., & Hsu, T. (2017). Large-scale experimental observations of sheet flow on a sandbar under skewed-asymmetric waves. *Journal of Geophysical Research: Oceans*, *122*(6), 5022–5045. https://doi.org/10.1002/2016JC012438

Nicholls, R. J., Wong, P. P., Burkett, V., Codignotto, J., Hay, J., McLean, R., Ragoonaden, S., Woodroffe, C. D., Abuodha, P. A. O., & Arblaster, J. (2007). *Coastal systems and low-lying areas*.

Nielsen, P. (1992). *Coastal bottom boundary layers and sediment transport* (Vol. 4). World scientific.

O'Donoghue, T., & Wright, S. (2004). Concentrations in oscillatory sheet flow for well sorted and graded sands. *Coastal Engineering*, *50*(3), 117–138. https://doi.org/10.1016/j.coastaleng.2003.09.004

Peregrine, D. H. (1983). Breaking Waves on Beaches. *Annual Review of Fluid Mechanics*, *15*(1), 149–178. https://doi.org/10.1146/annurev.fl.15.010183.001053

Puleo, J. A., Beach, R. A., Holman, R. A., & Allen, J. S. (2000). Swash zone sediment suspension and transport and the importance of bore-generated turbulence. *Journal of Geophysical Research: Oceans*, *105*(C7), 17021–17044. https://doi.org/10.1029/2000JC900024

Puleo, J. A., Blenkinsopp, C., Conley, D., Masselink, G., Turner, I. L., Russell, P., Buscombe, D., Howe, D., Lanckriet, T., McCall, R., & Poate, T. (2014). Comprehensive Field Study of Swash-Zone Processes. I: Experimental Design with Examples of Hydrodynamic and Sediment Transport Measurements. *Journal of Waterway, Port, Coastal, and Ocean Engineering*, *140*(1), 14–28. https://doi.org/10.1061/(ASCE)WW.1943-5460.0000210

Puleo, J. A., Faries, J., Davidson, M., & Hicks, B. (2010). A Conductivity Sensor for Nearbed Sediment Concentration Profiling. *Journal of Atmospheric and Oceanic Technology*, *27*(2), 397–408.

Puleo, J. A., Lanckriet, T., Conley, D., & Foster, D. (2016). Sediment transport partitioning in the swash zone of a large-scale laboratory beach. *Coastal Engineering*, *113*, 73–87. https://doi.org/10.1016/j.coastaleng.2015.11.001

Puleo, J. A., Lanckriet, T., & Wang, P. (2012). Near bed cross-shore velocity profiles, bed shear stress and friction on the foreshore of a microtidal beach. *Coastal Engineering*, 11.

Puleo, J. A., & Torres-Freyermuth, A. (2016). The second international workshop on swash-zone processes. *Coastal Engineering*, 7.

Rafati, Y., Hsu, T.-J., Cheng, Z., Yu, X., & Calantoni, J. (2020). Armoring and exposure effects on the wave-driven sediment transport. *Continental Shelf Research*, *211*, 104291. https://doi.org/10.1016/j.csr.2020.104291

Ribberink, J. S., & Al-Salem, A. A. (1995). Sheet flow and suspension of sand in oscillatory boundary layers. *Coastal Engineering*, *25*(3), 205–225. https://doi.org/10.1016/0378-3839(95)00003-T

Ruessink, B. G., van den Berg, T. J. J., & van Rijn, L. C. (2009). Modeling sediment transport beneath skewed asymmetric waves above a plane bed. *Journal of Geophysical Research*, *114*(C11), C11021. https://doi.org/10.1029/2009JC005416

Shields, A. (1936). *Application of similarity principles and turbulence research to bed-load movement*.

Sleath, J. F. A. (1999). Conditions for plug formation in oscillatory #ow. *Continental Shelf Research*, 22.

Small, C., & Nicholls, R. J. (2003). A Global Analysis of Human Settlement in Coastal Zones. *Journal of Coastal Research*, *19*(3), 17.

Sumer, B. M., Kozakiewicz, A., Fredsøe, J., & Deigaard, R. (1996). Velocity and concentration profiles in sheet-flow layer of movable bed. *Journal of Hydraulic Engineering*, *122*(10), 549–558.

Svendsen, I. A. (1984). Mass flux and undertow in a surf zone. *Coastal Engineering*, *8*(4), 347–365. https://doi.org/10.1016/0378-3839(84)90030-9

Svendsen, I. A., & Madsen, P. A. (1984). A turbulent bore on a beach. *Journal of Fluid Mechanics*, *148*, 73–96. https://doi.org/10.1017/S0022112084002251

Svendsen, I. A., Madsen, P. A., & Hansen, J. B. (1978). Wave characteristics in the surf zone. *Coastal Engineering Proceedings*, *1*(16), 29. https://doi.org/10.9753/icce.v16.29

Torres-Freyermuth, A., Puleo, J. A., & Pokrajac, D. (2013). Modeling swash-zone hydrodynamics and shear stresses on planar slopes using Reynolds-Averaged Navier-Stokes equations: MODELING SWASH-ZONE HYDRODYNAMICS. *Journal of Geophysical Research: Oceans*, *118*(2), 1019–1033. https://doi.org/10.1002/jgrc.20074

van der A, D. A., O'Donoghue, T., & Ribberink, J. S. (2010). Measurements of sheet flow transport in acceleration-skewed oscillatory flow and comparison with practical formulations. *Coastal Engineering*, *57*(3), 331–342. https://doi.org/10.1016/j.coastaleng.2009.11.006

van der Zanden, J., Alsina, J. M., Cáceres, I., Buijsrogge, R. H., & Ribberink, J. S. (2015). Bed level motions and sheet flow processes in the swash zone: Observations with a new conductivity-based concentration measuring technique (CCM +). *Coastal Engineering*, *105*, 47–65. https://doi.org/10.1016/j.coastaleng.2015.08.009

van der Zanden, J., Alsina, J. M., Caceres, I., Buijsrogge, R. H., Ribberink, J. S., Sancho, F., Fortes, C., & Tomasicchio, R. (2013). *New CCM technique for sheet flow measurements and its first application in swash zone experiments*. LNEC.

Zhao, Q., Kirby, J. T., & Puleo, J. A. (2011). Modelling on-shore sediment transport using energetics models. *Coastal Engineering Proceedings*, *1*(32), 16. https://doi.org/10.9753/icce.v32.sediment.16

Appendix A

PRESSURE SENSOR ARRAY

Design assembly for pressure array mount and specifications for individual pressure sensors.

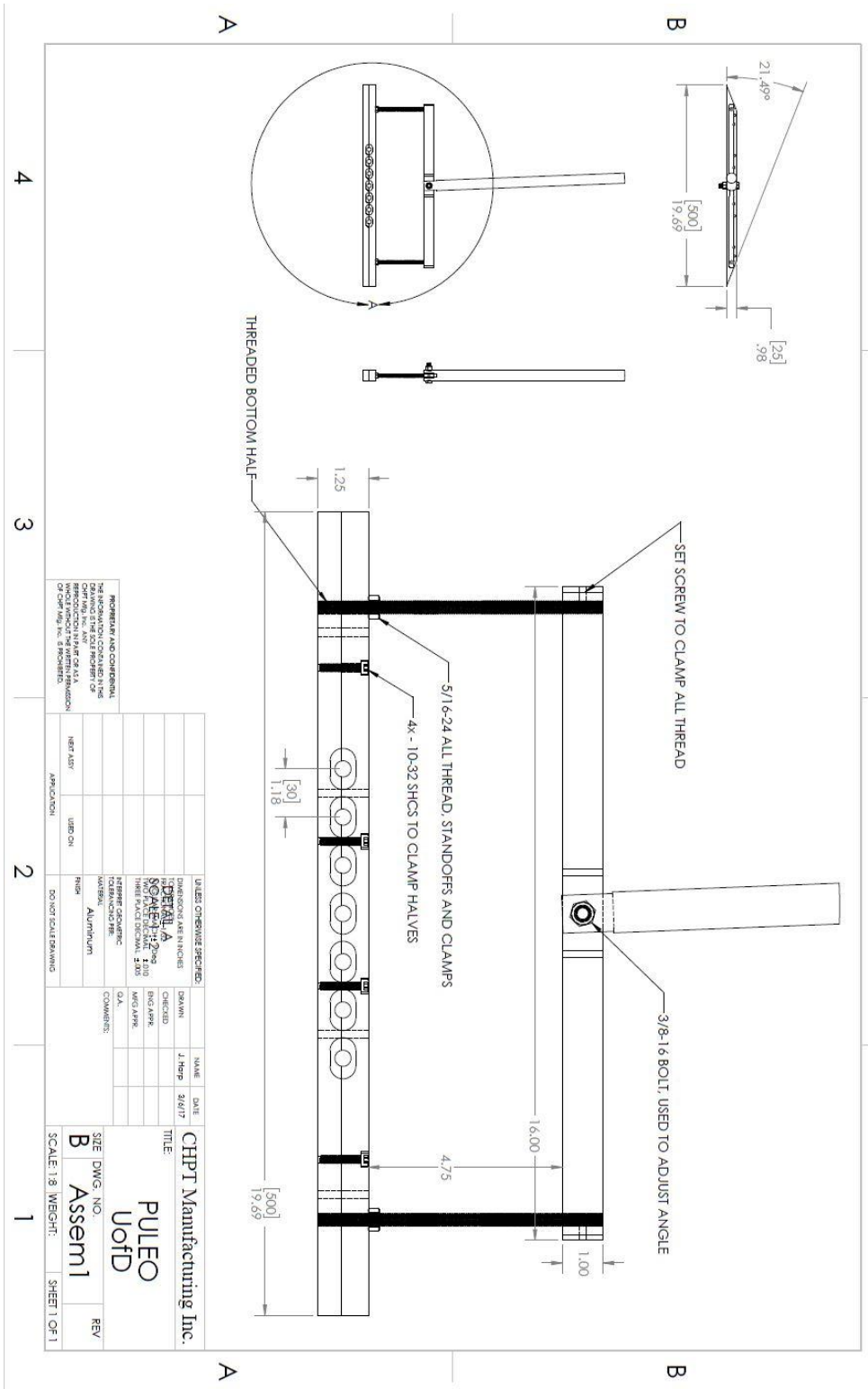

Figure A.1: Design assembly for pressure array mount and specifications for individual pressure sensors.

Appendix B

GROUP AVERAGES FOR ALL CONDITIONS

Appendix B provides a comprehensive list of figures illustrating group averages of the various bichromatic wave grouping sequences that were discussed in Section 3.3. The subplots present group averages of the relative changes in water depth, Shields parameter, Sleath number, and bed response.

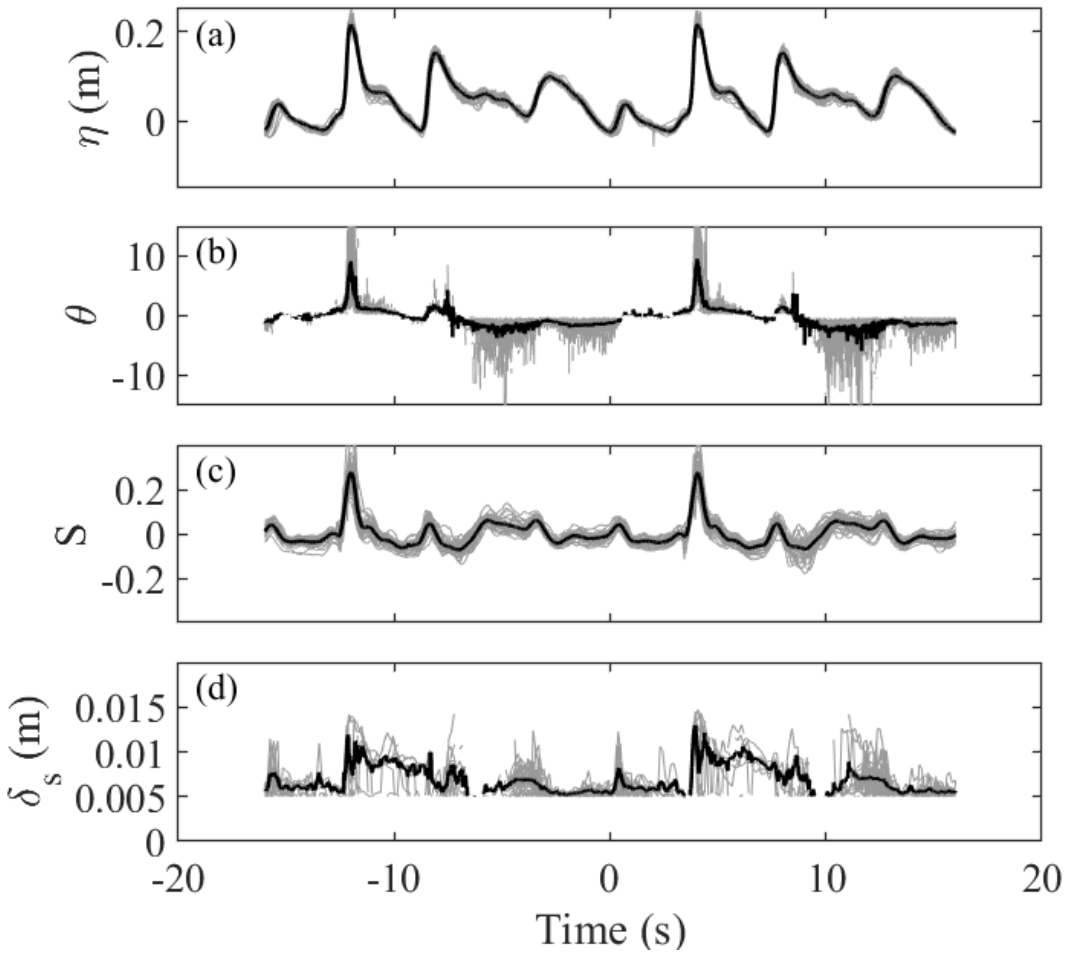

Figure B.1: Group averages of (a) free surface elevation, (b) Shields parameter, (c) Sleath number and (d) sheet flow layer thickness for condition B_E3_4W_R1 tested on the 1:15 slope profile. The black line represents the average values, and the gray lines are the individual realizations used in the averaging scheme.

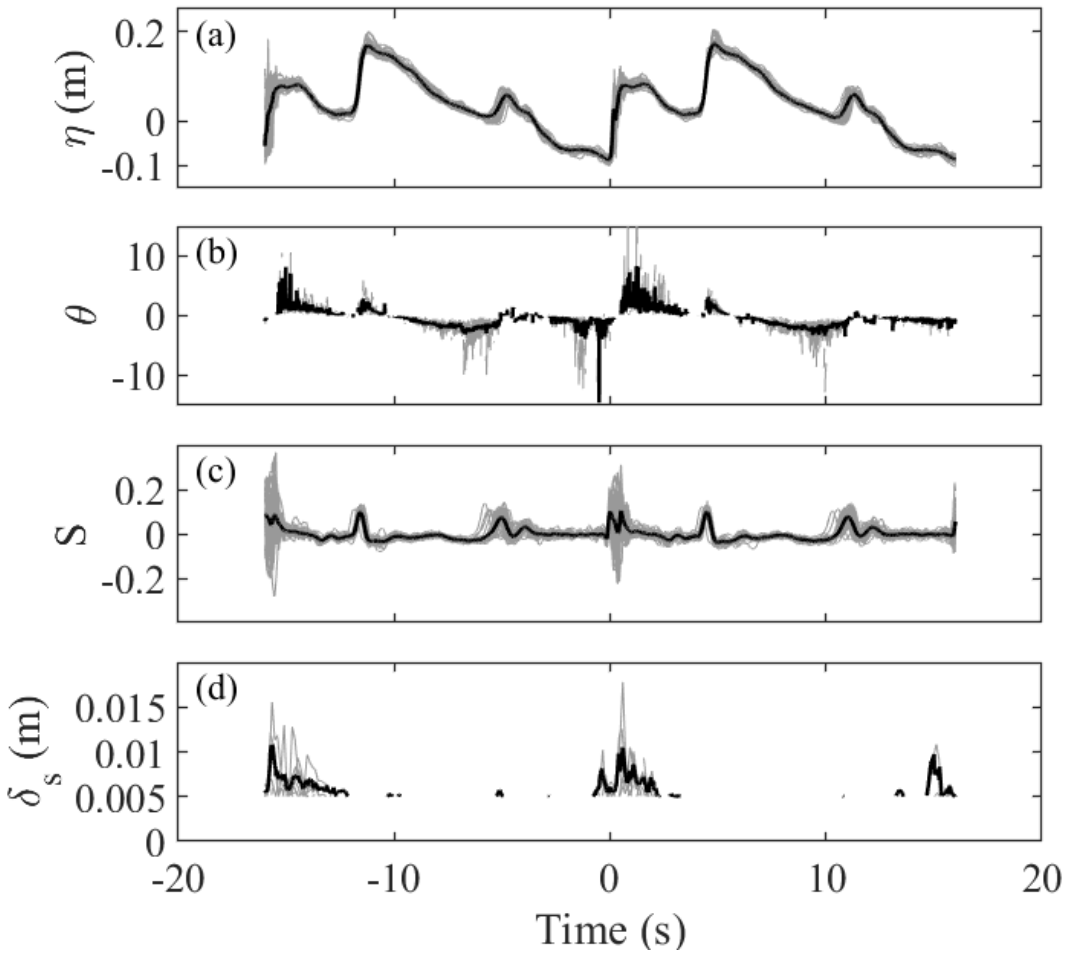

Figure B.2: Group averages of (a) free surface elevation, (b) Shields parameter, (c) Sleath number and (d) sheet flow layer thickness for condition B_E3_4W_R1 tested on the 1:25 slope profile. The black line represents the average values, and the gray lines are the individual realizations used in the averaging scheme.

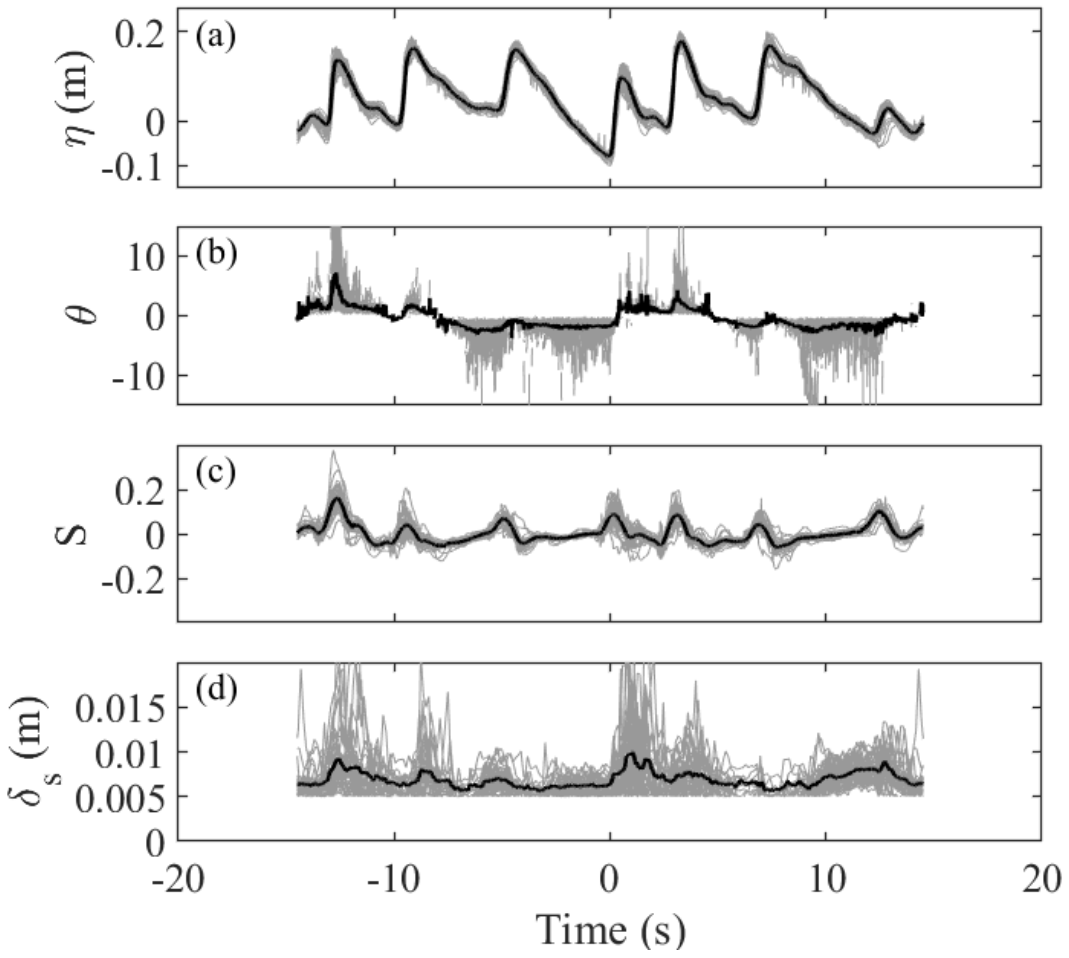

Figure B.3: Group averages of (a) free surface elevation, (b) Shields parameter, (c) Sleath number and (d) sheet flow layer thickness for condition B_E3_4W_R2 tested on the 1:15 slope profile. The black line represents the average values, and the gray lines are the individual realizations used in the averaging scheme.

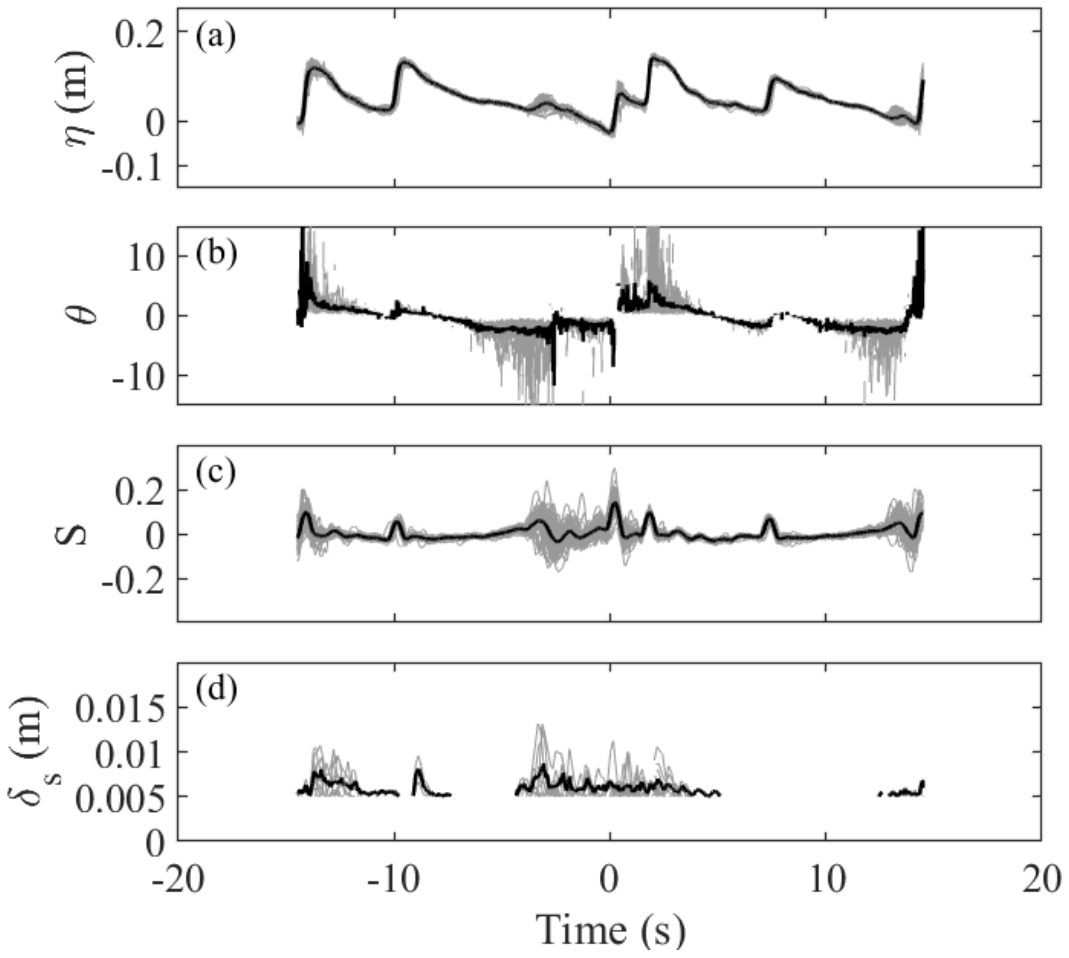

Figure B.4: Group averages of (a) free surface elevation, (b) Shields parameter, (c) Sleath number and (d) sheet flow layer thickness for condition B_E3_4W_R2 tested on the 1:25 slope profile. The black line represents the average values, and the gray lines are the individual realizations used in the averaging scheme.

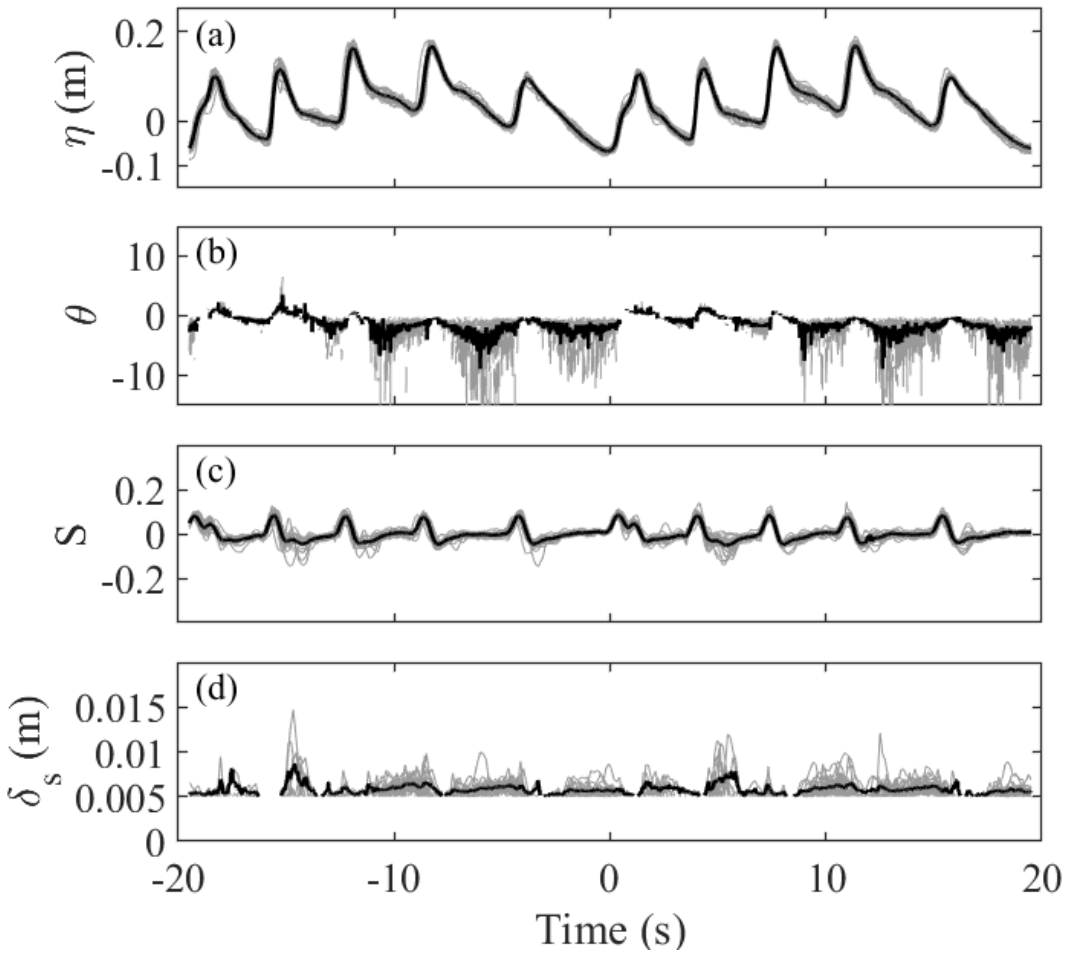

Figure B.5: Group averages of (a) free surface elevation, (b) Shields parameter, (c) Sleath number and (d) sheet flow layer thickness for condition B_E3_5W_R1 tested on the 1:15 slope profile. The black line represents the average values, and the gray lines are the individual realizations used in the averaging scheme.

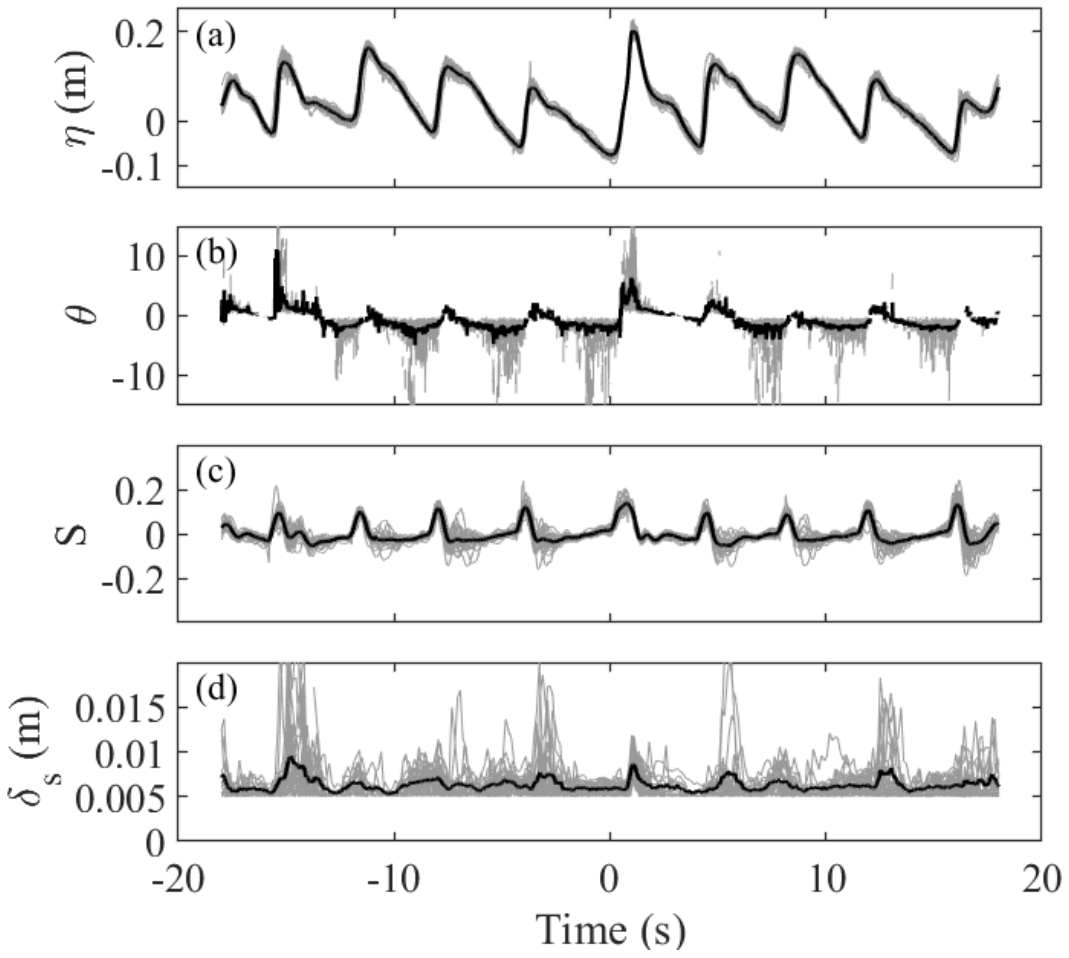

Figure B.6: Group averages of (a) free surface elevation, (b) Shields parameter, (c) Sleath number and (d) sheet flow layer thickness for condition B_E3_5W_R2 tested on the 1:15 slope profile. The black line represents the average values, and the gray lines are the individual realizations used in the averaging scheme.

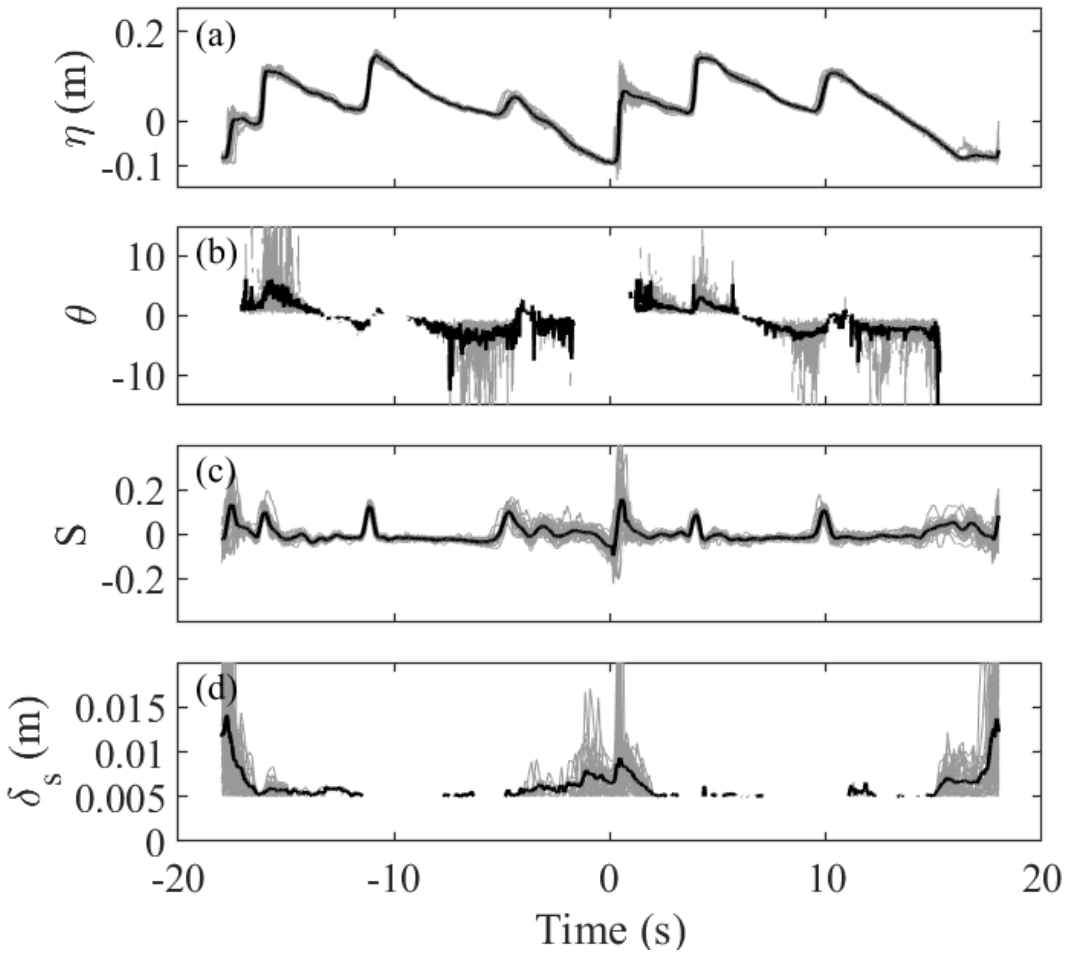

Figure B.7: Group averages of (a) free surface elevation, (b) Shields parameter, (c) Sleath number and (d) sheet flow layer thickness for condition B_E3_5W_R2 tested on the 1:25 slope profile. The black line represents the average values, and the gray lines are the individual realizations used in the averaging scheme.

Appendix C

TIME LAG COMPARISON OF SLEATH NUMBER AND SHIELDS PARAMETER

The additional figures presented in Appendix C represent bed response time lag comparisons of Sleath numbers and Shields parameters for various bichromatic conditions as discussed in Section 3.4.

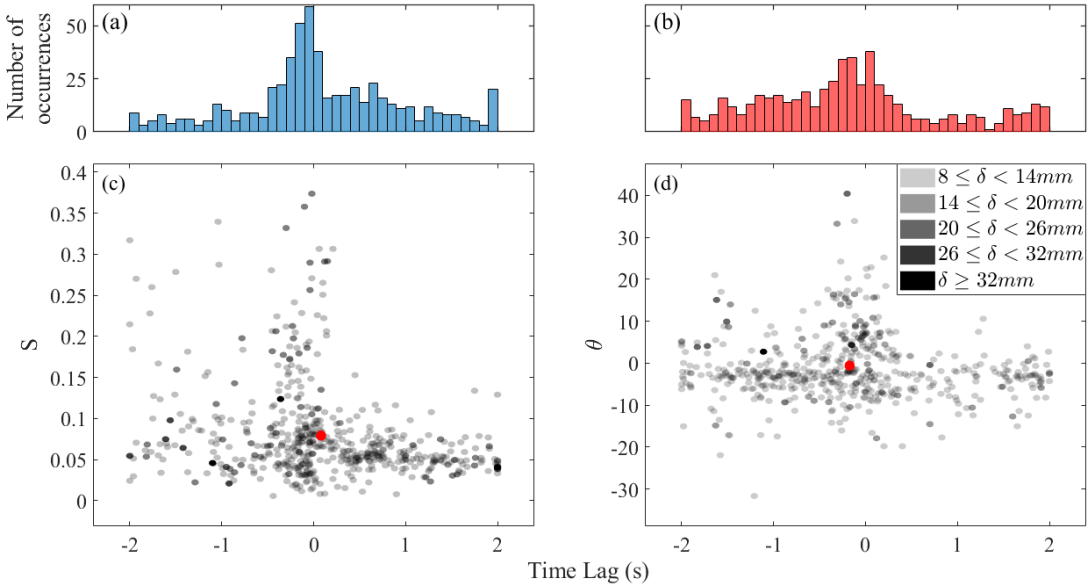

Figure C.1: Histograms of the time lags between peak bed response and the (a) corresponding peak Sleath number and (b) corresponding peak Shields parameter compared with (c) peak Sleath number and (d) peak Shields parameter plotted as a function of the time lag and magnitude of the corresponding peak sheet flow thickness (condition B_E3_4W_R1 tested on the 1:15 slope profile). The red dot denotes the center of mass of the plotted values weighted by the magnitude of sheet flow thicknesses.

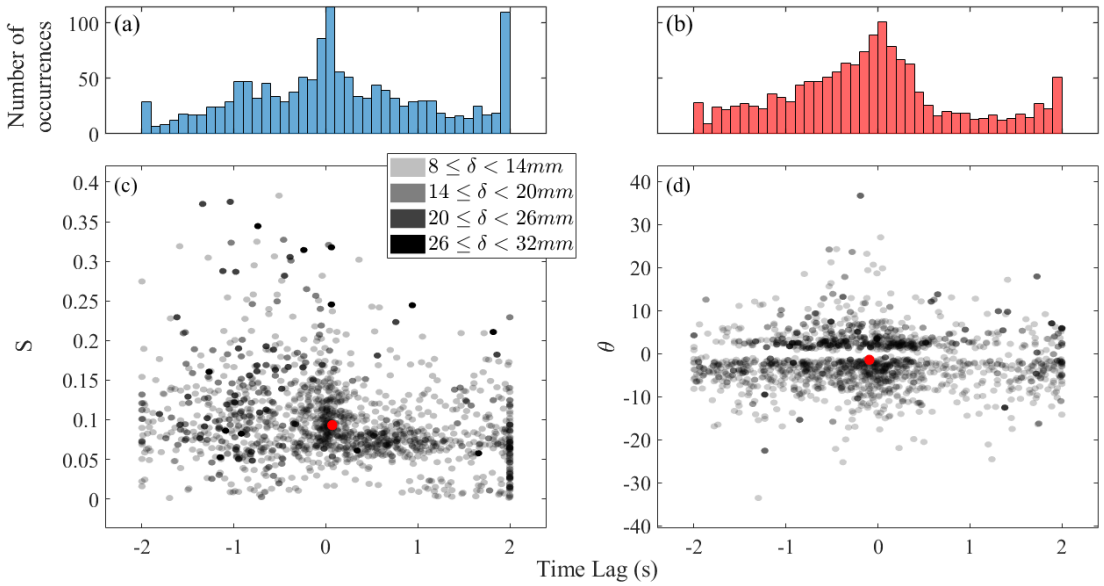

Figure C.2: Histograms of the time lags between peak bed response and the (a) corresponding peak Sleath number and (b) corresponding peak Shields parameter compared with (c) peak Sleath number and (d) peak Shields parameter plotted as a function of the time lag and magnitude of the corresponding peak sheet flow thickness (condition B_E3_4W_R2 tested on the 1:15 slope profile). The red dot denotes the center of mass of the plotted values weighted by the magnitude of sheet flow thicknesses.

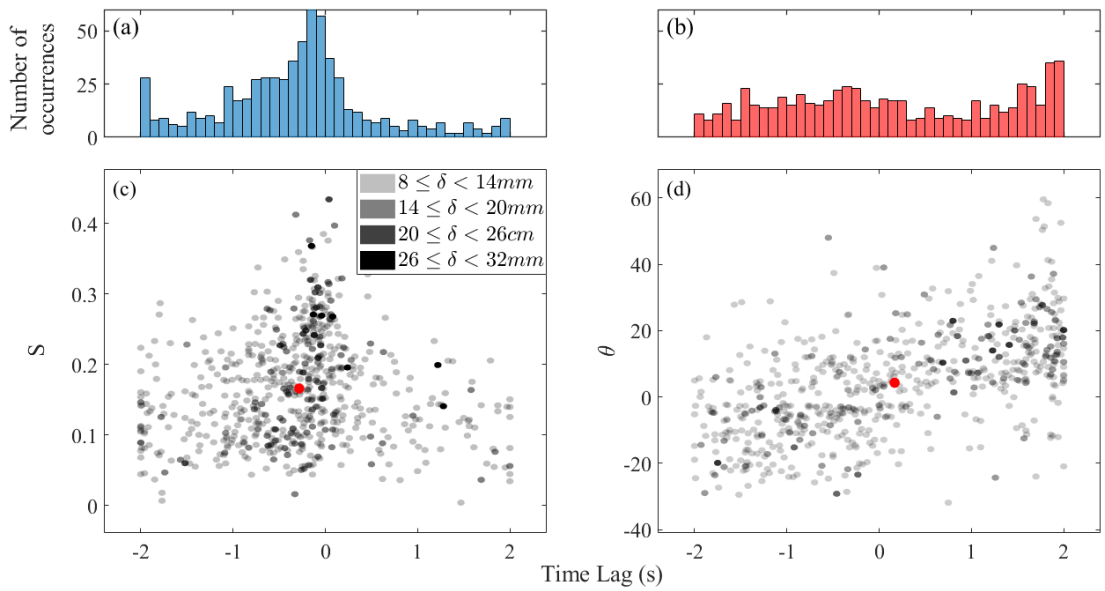

Figure C.3: Histograms of the time lags between peak bed response and the (a) corresponding peak Sleath number and (b) corresponding peak Shields parameter compared with (c) peak Sleath number and (d) peak Shields parameter plotted as a function of the time lag and magnitude of the corresponding peak sheet flow thickness (condition B_E3_4W_R2 tested on the 1:25 slope profile). The red dot denotes the center of mass of the plotted values weighted by the magnitude of sheet flow thicknesses.